

UC Berkeley

UC Berkeley Electronic Theses and Dissertations

Title

Microstructure, Mechanical Behavior, and Clinical Trade-offs in Ultra-High Molecular Weight Polyethylene for Total Joint Replacement

Permalink

<https://escholarship.org/uc/item/8v15s1hn>

Author

Atwood, Sara Anne

Publication Date

2010

Peer reviewed|Thesis/dissertation

Microstructure, Mechanical Behavior, and Clinical Trade-offs in
Ultra-High Molecular Weight Polyethylene for Total Joint Replacement

By

Sara Anne Atwood

A dissertation submitted in partial satisfaction of the

requirements for the degree of

Doctor of Philosophy

in

Engineering - Mechanical Engineering

in the

Graduate Division

of the

University of California, Berkeley

Committee in charge:

Professor Lisa A. Pruitt, Chair

Professor Tony M. Keaveny

Professor David M. Rempel

Spring 2010

Microstructure, Mechanical Behavior, and Clinical Trade-offs in
Ultra-High Molecular Weight Polyethylene for Total Joint Replacement

© 2010

by Sara Anne Atwood

Abstract

Microstructure, Mechanical Behavior, and Clinical Trade-offs in Ultra-High Molecular Weight Polyethylene for Total Joint Replacement

by

Sara Anne Atwood

Doctor of Philosophy in Engineering-Mechanical Engineering

University of California, Berkeley

Professor Lisa A. Pruitt, Chair

Ultra-high molecular weight polyethylene (ultra-high) often limits the longevity of total joint replacements due to excessive wear and associated clinical complications such as osteolysis. To mitigate such wear-related failure, manufacturers produced ultra-high that was highly cross-linked, typically by gamma radiation. Cross-linking was coupled with subsequent re-melting to neutralize free radicals that can lead to oxidative degradation of the material. However, cross-linking and re-melting decreased the resistance to fatigue crack propagation. In an attempt to preserve adequate resistance to fatigue and fracture while maintaining wear resistance and oxidative stability, manufacturers produced ultra-high that was either moderately cross-linked and re-melted, highly cross-linked and annealed below the melting temperature, or sequentially cross-linked and annealed. The success of such treatments remains a subject of debate due to the paucity of full-spectrum mechanical characterization studies that provide controlled comparisons amongst multiple clinically-relevant ultra-high materials.

This dissertation is the first study to simultaneously evaluate fatigue crack propagation, wear, and oxidation in a wide variety of clinically-relevant ultra-high. Results have important clinical implications: primarily, none of the materials was able to excel in all three areas. The moderately cross-linked re-melted material did equally well in all areas, but did not excel in any. With respect to processing treatments, increasing radiation dose increased wear resistance but decreased fatigue crack propagation resistance. Annealing reduced fatigue resistance less than re-melting, but left materials susceptible to oxidation. This appears to occur because annealing below the melting temperature after cross-linking increased the volume fraction and size of lamellae, but failed to neutralize all free radicals. Alternately, re-melting after cross-linking appeared to eliminate free radicals, but, restricted by the network of cross-links, the re-formed lamellae were fewer and smaller in size which resulted in poor fatigue crack propagation resistance.

The trade-off demonstrated is critical to the material's long-term success in total joint replacements: 1) excessive wear is a historical problem that results in large numbers of failures; 2) poor resistance to fatigue crack propagation and fracture has been implicated in recent reports of cross-linked re-melted hip liners fracturing in vivo; and 3) highly oxidized ultra-high cannot adequately withstand in vivo demands. Understanding the shortcomings of the current marketed materials, as well as the relationship of mechanical performance to treatment and microstructure, allows for targeted improvements needed to produce materials and designs that can withstand rigorous in vivo mechanical demands and improve the longevity of total joint arthroplasty.

To the students who came into office hours, said hello in the hallways, stayed after class to ask excited questions, tried their best whether they loved the subject or not, and shared with me when their dreams were coming true. You always reminded me why I wanted this degree, and what it will allow me to do.

Acknowledgements

As I'm finishing my dissertation and looking forward to the next stage in my life, I'm realizing what I will miss about living in Berkeley for the last five years. The temperate weather and beautiful outdoors fostered my love of running, while the proximity of San Francisco allowed me to experience a major city with its restaurants, symphony, and the Nutcracker ballet every year. But mostly I will miss the food – Cheeseboard pizza, tasty Thai, fresh Mexican, and my weekly grocery outing to Monterey Market, Magnani's, and Trader Joes.

In addition to the place itself, there are professors at Berkeley who have been instrumental to my success here: first and foremost Lisa Pruitt for her welcome advice on navigating the department, securing my ideal faculty position, and always striving for balance in my life. Lisa is a genuine role model for promoting teaching, outreach, leadership, diversity, community, and her life outside academia. Tony Keaveny, for teaching me practical knowledge that I will continue to use throughout my career, including clear and concise writing, short introductions, presentations lacking bullet points, specific aims, testable hypotheses, and critical thinking skills in general. Dr. Rempel, for serving as a member of my qualifying exam and dissertation committee. Dr. Ries, for providing a clinical perspective in all of my work. And Linda von Hoene, for teaching me about teaching, and for valuing it.

My labmates in the Medical Polymers Group have made coming into work every day rewarding and fun. In particular, Shikha and Sheryl for taking me under their wings as senior students, Alastair for making me excited about my research, Matt for engaging me in interesting conversations about the world outside of lab, and Eli for sharing our cubicles, our research, and our grad student lives for the last two years. I also couldn't have completed this thesis without the assistance of many wonderful undergraduate researchers over the years: Erik, Mike, John, Stephanie, Perry, Mike, Chris, Ingrid, Tim, and Robyn. And Ivan, who supported my academic goals and allowed me to help him achieve his own. It has truly been one of my favorite parts of graduate school to see you all become confident students and researchers, and to see where your lives take you after Berkeley.

The Mechanical Engineering department and the University of California have provided fellowships and graduate student instructorships over the years, for which I am grateful. In addition to funding, the Mechanical Engineering department staff has helped me more times than I can count, in my personal education and in my efforts to leave the department community in better shape than I found it. Particularly Donna, Pat, Shareena, and Yawo who have answered questions and opened locked doors numerous times, both literally and figuratively.

A little farther afield, my former Dartmouth family has continued to be a source of support and encouragement from thousands of miles away. Collaboration with the Dartmouth Biomedical Center has enhanced this research and my education substantially. Especially with Doug, who continues to be an invaluable mentor and friend, and with the Curriers, who continue to be role models for me both professionally and personally. Also from my Dartmouth family, Eleanor and Cici have provided a listening ear on the other side of many phone calls, and the occasional visit. I could not have done it without you.

My Texas family has also kept me going over the years. It has meant more than I can say to know how proud my family is of my accomplishment. It makes me smile to know that Papa and Mimi brag to their friends (and anyone else who will listen). I have frequently looked forward to resting and replenishing myself at my parents' and aunts' and uncles' homes, even when I couldn't be in Cleburne often. Most of all my parents – my mom who shows me how to get out of bed energetically and accomplish something every day, and my dad who shows me how to go above and beyond in my efforts, like sweeping crickets at the bank on the weekends.

My years in Berkeley have been made indescribably more fun and filled with love by the company of Oscar and Greg. Oscar the Cat has been with me from the beginning, with a purr and a furry head-butt on my good and bad days alike. Greg has come into our lives more recently, and has quickly become my best friend and constant companion – someone with whom I can share silly tv shows and major life decisions. I look forward to continuing my life with both of you beside me.

And finally, Sarah and Aaron. You have been with me from the very first class, through every major moment in my life in the last five years. I can't thank you enough for washing my dishes when I was stressed about quals or sick with the flu, or coming over in the middle of the night when I needed to talk, or driving me and Oscar to the airport, or stopping by the lab to provide hours of welcome distraction, or running hundreds, maybe thousands, of miles together. Although I came to Berkeley knowing no one, once I met you two I never felt alone.

Table of Contents

Chapter 1: Introduction	1
1.1 Total Joint Replacement	1
1.2 Ultra-High Molecular Weight Polyethylene	3
1.3 Historical Evolution of Orthopaedic Ultra-High Motivated by Clinical Failure	5
1.4 Dissertation Aims and Study Design	9
Chapter 2: Materials and Methods	11
2.1 Materials	11
2.2 Methods	12
2.2.1 Tensile Testing	12
2.2.2 Fatigue Crack Propagation Testing	13
2.2.3 Wear Testing	15
2.2.4 Oxidation Following Artificial Aging	18
2.2.5 Microstructure	19
2.2.6 Statistical Analysis of Pair-wise Correlations	24
Chapter 3: Results	25
3.1 Tensile Behavior	25
3.2 Fatigue Crack Propagation	27
3.3 Wear Rate	31
3.4 Oxidation	35
3.5 Microstructure	36
3.6 Statistical Correlations	44
Chapter 4: Discussion and Conclusions	46
4.1 Trade-offs in Material Behavior	46
4.2 Material Behavior and Processing Treatments	47
4.3 Effect of Microstructure	47
4.4. Limitations	48
4.5 Strength of Study	51
Chapter 5: Implications and Future Work	52
5.1 Clinical Implications	52
5.2 Future Work: Computational Modeling of Microstructure	52
5.3 Closing Thoughts	56
References	57
Appendix A: Clinical Case of Fracture in an Orthopaedic Implant	65
Appendix B: Evolution of Lamellar Alignment in Plastically-Strained Ultra-High	71

List of Figures

Chapter 1: Introduction

Figure 1.1 Natural articular joint	1
Figure 1.2 Components comprising total knee and hip replacements	2
Figure 1.3 Chemical structure of polyethylene	4
Figure 1.4 Semicrystalline microstructure of ultra-high	4
Figure 1.5 Severely worn and delaminated retrievals	6
Figure 1.6 Gamma radiation results in a lower wear rate	7
Figure 1.7 Cross-linked decreases fatigue crack propagation resistance	8
Figure 1.8 Timeline schematic of the evolution of ultra-high	10

Chapter 2: Materials and Methods

Figure 2.1 Ultra-high materials and processing treatments.....	12
Figure 2.2 Tensile testing setup	13
Figure 2.3 Fatigue crack propagation testing schematic.....	14
Figure 2.4 Custom pin-on-disk tribotester	16
Figure 2.5 Geometry of hemispherical ended wear pin	17
Figure 2.6 Changes in wear pin geometry due to creep recovery	18
Figure 2.7 Typical spectroscopy scan of oxidized ultra-high	19
Figure 2.8 Typical differential scanning calorimetry graph	20
Figure 2.9 Microstructure images subjected to image analysis	21
Figure 2.10 Lamellae are analogous to scattering planes of atoms	23
Figure 2.11 X-ray scattering determination of lamellar thickness	24

Chapter 3: Results

Figure 3.1 Typical stress-strain curve for ultra-high	25
Figure 3.2 Tensile properties for all materials	26
Figure 3.3 Fatigue crack propagation data for all materials.....	27
Figure 3.4 Fatigue crack propagation data for re-melted materials	28
Figure 3.5 Wear data for all materials	32
Figure 3.6 Wear volume measurements considering creep recovery	35
Figure 3.7 Artificial aging data for all materials	36
Figure 3.8 Microstructural characterization of representative materials	37
Figure 3.9 Microstructure properties for all materials	38
Figure 3.10 Comparison of average lamellar thickness using various techniques	40
Figure 3.11 Comparison of average lamellar length using various techniques	41
Figure 3.12 Comparison of average lamellar size using various techniques	42
Figure 3.13 Comparison of average lamellar thickness using x-ray scattering	43

Chapter 4: Discussion and Conclusions

Figure 4.1 Schematic showing trade-offs in ultra-high behavior	46
--	----

Chapter 5: Implications and Future Work

Figure 5.1 Representative finite element model of ultra-high microstructure	54
Figure 5.2 Schematic of future computational modeling	55

Appendix A: Clinical Case of Fracture in an Orthopaedic Implant

Figure A.1 Schematic illustration of the fracture process 65
Figure A.2 Radiograph and photograph of fractured implant 66
Figure A.3 Initiation site and fracture surface of implant 67
Figure A.4 Areas of burnishing and fretting on implant 68
Figure A.5 Schematic illustration of bending stresses on implant neck 69

Appendix B: Evolution of Lamellar Alignment in Plastically-Strained Ultra-High

Figure B.1 Schematic of testing and characterization procedure 72
Figure B.2 Scanning electron micrographs of the plastically-deformed lamellae 73

List of Tables

Chapter 1: Introduction

Table 1.1 Physical properties of conventional untreated ultra-high	5
--	---

Chapter 2: Materials and Methods

Table 2.1 Ultra-high material groups tested	11
Table 2.2 Wear test parameters	15

Chapter 3: Results

Table 3.1 Estimated fatigue crack propagation parameters for all materials	29
Table 3.2 Regression on fatigue crack propagation data for all materials	29
Table 3.3 Estimated fatigue crack propagation parameters for re-melted materials	30
Table 3.4 Regression on fatigue crack propagation data for re-melted materials	30
Table 3.5 Regression on fatigue, resin, and radiation dose for re-melted materials	31
Table 3.6 Statistical comparisons of wear rates	33
Table 3.7 Steady state wear rates for all materials	33
Table 3.8 Multiple comparison procedure on war rates	34
Table 3.9 Crystallinity increase after aging in oxidized materials	36
Table 3.10 Lamellar parameter estimates using various techniques	39
Table 3.11 Lamellar thickness measurements of x-rayed materials	43
Table 3.12 Correlations between microstructure and mechanical behavior	44
Table 3.13 Detailed results from Spearman rank correlation analysis	45

Appendix B: Evolution of Lamellar Alignment in Plastically-Strained Ultra-High

Table B.1 Thermal analysis results on plastically-strained ultra-high	72
---	----

Chapter 1

Introduction

1.1 Total Joint Replacement

Natural Joints

There are over three hundred joints in the human body, whose purpose is to provide a combination of mobility and stability to allow for the controlled motion of the skeletal system. Load-bearing articular joints are remarkable natural bearing systems, supporting loads up to ten times body weight at more than 2 million loading cycles per year, for almost 100 years (John Fisher, 2001; J. Fisher & Dowson, 1991; Mow & Hayes, 1991). In a healthy articular joint, the bones are covered with articular cartilage and the contact is lubricated by synovial fluid (Figure 1.1), resulting in a bearing system with extremely low wear and friction (Williams, 1994).

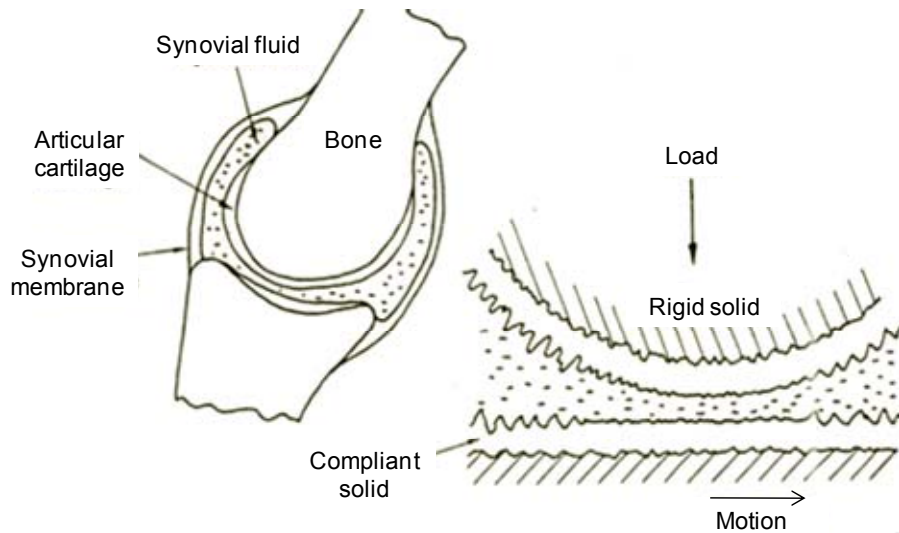


Figure 1.1. Natural articular joint showing articular cartilage covering the bone (*left*) and schematically represented as an engineering bearing system (*right*) From (Williams, 1994).

Conditions exist in which human joints deteriorate over time or due to trauma, resulting in the deterioration of the articular cartilage (osteoarthritis). Healthy articular cartilage, made up of 80% water and 20% of a type-2 collagen fiber network and hydrophilic proteoglycans, can support and lubricate the joint under complex dynamic loading situations. However, once damaged, cartilage is slow to recover due to its avascularity (Dumbleton, 1981; John Fisher, 2001). This leads to bone-on-bone contact, limited motion, pain, and ultimately the replacement of the natural joint by an engineered total joint replacement (Dumbleton, 1981).

Total Joint Replacement

Total joint replacement restores pain-free mobility using engineering materials, but does not necessarily mimic the natural bone and cartilage. Most total joint replacements are composed of two metal components that attach to the bone (usually a titanium or cobalt chrome alloy), and a polymer bearing (Figure 1.2). The titanium alloy (usually Ti6Al4V) encourages bone ingrowth, while the cobalt chrome alloy (usually CoCrMo) is hard enough to maintain an extremely smooth surface finish for articulation against the polymer. The polymer is almost exclusively ultra high molecular weight polyethylene (ultra-high, or UHMWPE).

Alternative bearing couples are sometimes used in hip joint replacement, including metal-on-metal (35%) and ceramic-on-ceramic (14%). However, metal-on-ultra-high remains the bearing couple of choice in 51% of hip replacements and virtually all knee replacements in the United States (Bozic, Kurtz et al., 2009a).

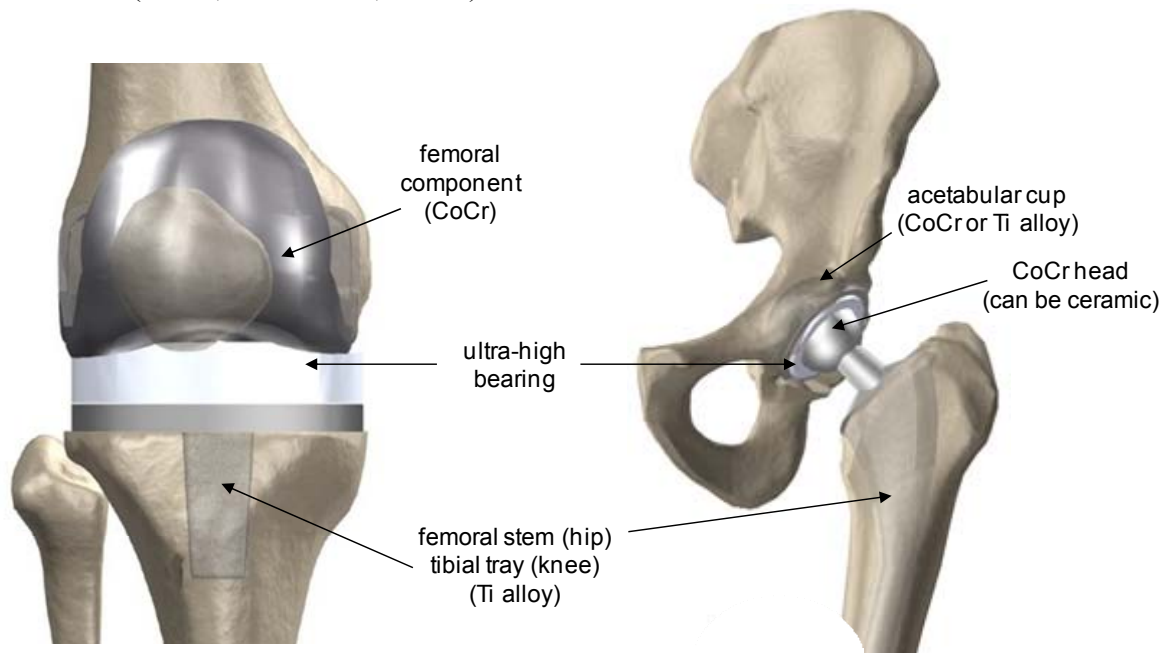


Figure 1.2. Components comprising total knee and hip replacements, including metal components attached to the bone and an ultra-high bearing. Modified from www.eorthopod.com.

The hip and the knee are the most commonly replaced joints, followed by the spine, shoulder, elbow, and ankle. The hip is a relatively conforming ball-and-socket joint with a wide range of motion including translation and rotation in several planes. This anatomy results in an implant undergoing relatively low contact stresses (2-10 MPa, due to the high conformity) and cross-shearing motion. The knee, in contrast, is much less conforming with motion that is primarily rolling-sliding due to flexion-extension. The anatomy of the knee results in an implant undergoing relatively high contact stresses (20-30 MPa or higher) and uniaxial motion. Most of the other replaced joints fall somewhere between in terms of conformity and motion (Bartel, Bicknell, & Wright, 1986; Bartel, Rawlinson, Burstein, Ranawat, & Flynn, 1995; S. M. Kurtz, 2009b, 2009c).

Together, hip and knee replacements numbered over 600,000 in the United States during 2003 (202,500 hip, 402,100 knee) (S. Kurtz, Ong, Lau, Mowat, & Halpern, 2007). Despite the success of most of these surgeries, about 10% of joint replacements fail during the patient's lifetime due to problems including pain, loosening, limited range of motion, instability, tissue degradation, and implant failure (Bozic, Kurtz et al., 2009b; Bozic, Kurtz, Lau, Ong, Vail et al., 2009; S. Kurtz et al., 2005). The revision procedure consists of the removal and replacement of one or more of the implant components, most commonly the ultra-high bearing. Revision surgeries are more costly than primary replacement surgeries with a lower rate of success (D. W. Van Citters, 2003).

The reason for revision in approximately 20% of hips and 16% of knees is implant loosening, often associated with periosteal osteolysis (Bozic, Kurtz et al., 2009b; Bozic, Kurtz, Lau, Ong, Vail et al., 2009). Osteolysis describes the loss of bone tissue surrounding an implant as a reaction to the presence of small foreign particles. In the case of hip and knee replacements, these foreign particles are primarily from wear of the ultra-high bearing (Harris, 2001; Ingram, Stone, Fisher, & Ingham, 2004). Other common reasons for retrieval are infection (15% in the hip, 25% in the knee) and instability/dislocation (22% in the hip) (Bozic, Kurtz et al., 2009b; Bozic, Kurtz, Lau, Ong, Vail et al., 2009). Infections and instability are relatively short-term failures and are related to patient and surgical factors rather than mechanical failure.

Failures of total joint replacements are a growing problem facing the U.S. population and healthcare system. In 2003, there were 604,600 primary total hip and knee replacements performed in the United States, which had increased from 248,000 in 1990. In the same time period, the percentage of revision procedures to replace one or more failed components stayed approximately constant at 12% of all total joint surgeries performed (S. Kurtz et al., 2005; S. Kurtz et al., 2007). Considering these rates, along with an aging baby boomer population, the increasing incidence of obesity, and a more active elderly population, it has been estimated that by 2030, the demand for total hip and knee replacements could reach 4 million procedures annually in the United States alone. Unless the revision rate is reduced by advances in the field, revision procedures are expected to number about 350,000 per year (S. Kurtz et al., 2007).

Based on these numbers, it has been estimated that a 1% reduction in the percentage of revision procedures would result in approximately 96 to 211 million dollars in savings for the U.S. healthcare system (S. Kurtz et al., 2007; S. M. Kurtz et al., 2007; Ong et al., 2006), not to mention the reduction in the number of patients undergoing a second surgery and recovery.

1.2 Ultra-High Molecular Weight Polyethylene

Ultra-high molecular weight polyethylene (ultra-high) is utilized in about 90% of total joint replacements (Bozic, Kurtz et al., 2009a). It is also the component that most commonly fails and is replaced during revision surgery: approximately 53% of knee revisions and 80% of hip revisions (Bozic, Kurtz et al., 2009b; Bozic, Kurtz, Lau, Ong, Vail et al., 2009). Therefore, it is important to understand the underlying microstructure and performance of ultra-high as a bearing material for orthopaedic applications.

Ultra-High Microstructure

Polyethylene is a long chain molecule made by the synthesis of the simple organic compound ethylene through an addition reaction (Figure 1.3). The carbon atoms are covalently bonded, while the long chains are held next to one another by secondary van der Waals bonds (Lin & Argon, 1994). A polyethylene chain contains on average 250,000 to 500,000 carbon atoms and can be 18 microns long (Lynch, 1982). Ultra-high specifically refers to a polyethylene with a large number of long linear chains (the Ziegler-Natta catalyst maintains linearity throughout the polymerization) and an extremely high molecular weight (about 2-6 million grams/mole as opposed to 200,000 grams/mole for high density polyethylene). The elevated molecular weight contributes to relatively high wear resistance and toughness compared to other polyethylenes (commonly used to make items such as plastic bags and milk jugs) (S. M. Kurtz, 2009d).

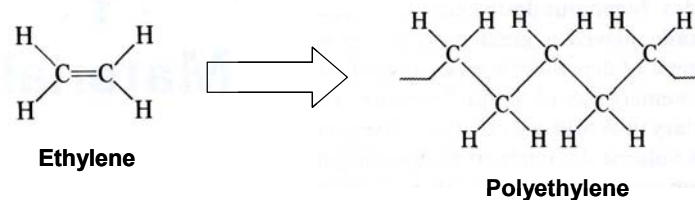


Figure 1.3. Chemical structure of polyethylene (Lynch, 1982)

Ultra-high microstructure is semi-crystalline, composed of approximately 50% crystallites (lamellae) with the remaining 50% taken up by amorphous polymer chains that surround and weave amongst the lamellae (Figure 1.4). The crystalline lamellae consist of tightly-packed polyethylene chains folded back on themselves to create a plate-like structure with a thickness of 10 to 50 nanometers and a length and width of about 10 to 50 microns (S. M. Kurtz, 2009d). The amorphous phase surrounding the lamellae consists of a random entanglement of polyethylene chains. Some of these amorphous chains are incorporated into one or more lamellae which serve to interconnect the crystalline phase. These incorporated chains are called tie molecules, have a density of about 1 to 30 volume percent, and are thought to be responsible for the high ductility of ultra-high (Lin & Argon, 1994).

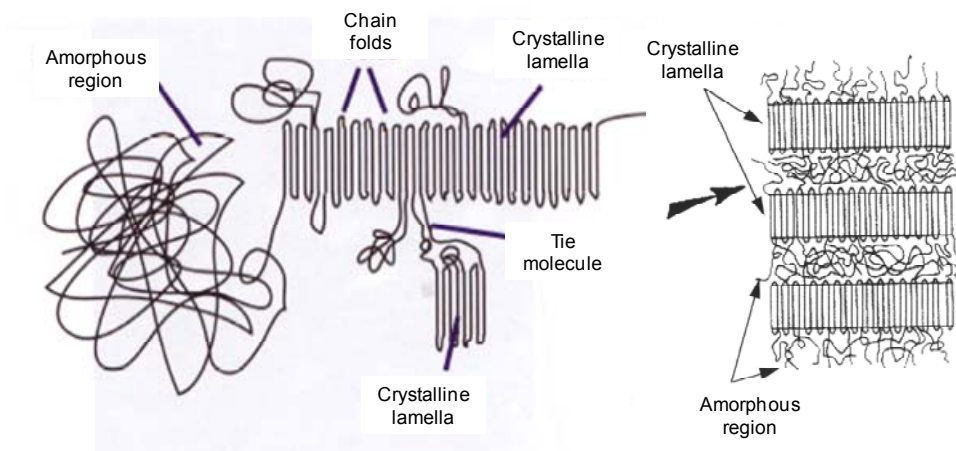


Figure 1.4. Semicrystalline microstructure of ultra-high (compiled from (S. M. Kurtz, 2009d) and (Goldman, Gronsky, & Pruitt, 1998)).

Ultra-High Properties

In its pure form, ultra-high for orthopaedic applications has exceptional mechanical properties due to its semi-crystalline microstructure, high molecular weight, and moderate crystallinity (L. A. Pruitt, 2005). The properties of untreated ultra-high are shown in Table 1.1.

Property	Untreated ultra-high (GUR 1050)
Molecular Weight	~6 million g/mol
Crystallinity	45-50%
Density	0.93-0.935
Ultimate tensile strength (21°)	42-44 MPa
Ultimate tensile strength (37°)	36 MPa
Yield strength (21°)	20-23 MPa
Yield strength (37°)	21 MPa
Elastic modulus (21°)	1.0-1.39 GPa
Elastic modulus (37°)	0.67 GPa
Elongation at fracture (21°)	330%
Elongation at fracture (37°)	375%
Shore D hardness (21°)	60-65

Table 1.1. Physical properties of conventional untreated ultra-high.
Adapted from (L. A. Pruitt, 2005).

1.3 Historical Evolution of Orthopaedic Ultra-High Motivated by Clinical Failure

Ultra-high has evolved during its half century as an orthopaedic bearing material. Changes in complicated processing methods have been primarily in response to clinical failures, producing several generations of ultra-high: 1) gamma-in-air sterilized (zero-generation) which oxidized and wore severely, 2) moderately and highly cross-linked re-melted materials (first-generation) which have improved wear resistance and oxidative stability, but poor fatigue resistance, and 3) current second-generation annealed materials. Furthermore, it must be noted that the evolution of ultra-high has been motivated by addressing clinical failures rather than by understanding the relationship amongst processing treatments, microstructure, and mechanical performance.

Ultra-high for orthopaedic use starts in the form of powder, or resin. Currently there are two primary resins (GUR 1020 and GUR 1050) which differ in their molecular weight (2-4 and 4-6 million grams/mole, respectively). Calcium stearate was historically included in the powder (GUR 415, 412) to scavenge residual catalyst components during processing, but was discontinued during the 1990s because the calcium stearate was associated with fusion defects that nucleated cracks. These cracks were detrimental to the fatigue behavior of the ultra-high, particularly in the rolling-sliding contact of knee replacements (S. M. Kurtz, Muratoglu, Evans, & Edidin, 1999). In addition, processing improved so that calcium stearate was no longer needed for polymerization (S. M. Kurtz, 2009a).

After polymerization from the resin, ultra-high must be formed into components for orthopaedic purposes. Due to its high molecular weight, ultra-high does not flow like many polymers and cannot be formed using common processes such as injection molding. The resin is

usually either compression molded into a sheet and then machined, ram extruded into a bar or rod and then machined, or direct compression molded into the shape of the component (S. M. Kurtz, 2009a). After shaping, ultra-high for use in the body must be sterilized. Different manufacturers have various methods including exposure to gas plasma, ethylene oxide (EtO), or most commonly, gamma irradiation (L. A. Pruitt, 2005).

The first major historical failure of clinical ultra-high involved sterilization and oxidative degradation of the material. In the 1980s and 1990s, many implants failed due to excessive wear and delamination of the ultra-high component, leading to osteolysis and in some cases wear-through (Figure 1.5). In the mid-1990s, it was determined that sterilization using gamma radiation (up to 4 Mrad) in the presence of oxygen (“gamma in air”) accelerates the chemical and mechanical degradation of ultra-high in a process known as oxidation. The gamma radiation creates free radicals in the material which, in the presence of oxygen, leads to chain scission, decreased molecular weight, and increased percent crystallinity. These changes in the microstructure result in embrittlement and a loss of mechanical properties, which manifested as severe wear, delamination, and ultimately failure of implants (Collier, Sperling et al., 1996; Costa et al., 1998a, 1998b; L. A. Pruitt, 2005; Sutula et al., 1995).

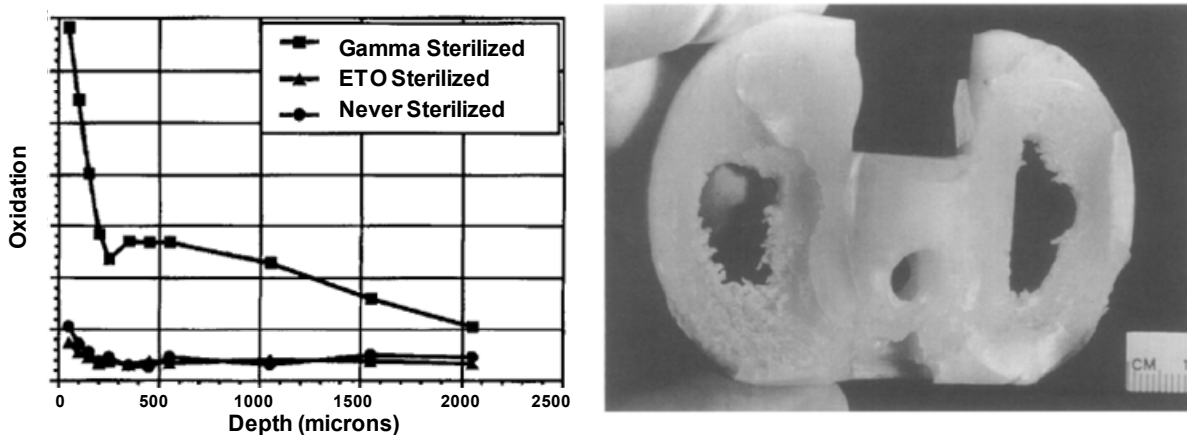


Figure 1.5. Severely worn and delaminated retrievals were found to be due to oxidative degradation caused by gamma sterilization in the presence of oxygen. Modified from (Collier, Sperling et al., 1996).

Before it was determined that oxidation was causing the severe wear and delamination seen in the 1980s, attempts to improve the properties of ultra-high were made by manufacturers. One such attempt was marketed by DePuy in 1994 under the trade-name Hylamer. Hylamer was processed using high pressure, high temperature, and controlled cooling, which produced a high crystallinity microstructure (70% crystalline) with larger lamellae. This highly-crystalline microstructure resulted in a material with higher modulus and yield strength, better fatigue and creep resistance, and a lower wear rate than traditional ultra-high (Li & Burstein, 1994; Rockwood & Wirth, 2002). Hylamer was implanted in hip liners, tibial trays, and glenoid shoulder components.

The laboratory testing on Hylamer was performed on unsterilized material, but implanted Hylamer was being sterilized with gamma radiation in air as was the industry standard. Hylamer implants failed after extremely short times in vivo with reports of severe wear, cracking, pitting,

and delamination. It was discovered that Hylamer had a more substantial decrease in mechanical properties upon oxidation (Collier et al., 1998). This decrease in mechanical properties combined with the higher modulus was thought to lead to Hylamer's poor in vivo performance. Use of Hylamer was virtually discontinued, with the warning that implants in shelf storage were rapidly oxidizing. After 1995, Hylamer was sterilized with gas plasma, but in 1998 Hylamer was replaced with conventional ultra-high sterilized with gas plasma (Rockwood & Wirth, 2002). The Hylamer episode showed the orthopaedic community that laboratory testing does not always predict clinical success, and ultimately made the community wary of scientific improvements to the conventional material.

Despite causing oxidation, in the late 1990s and early 2000s it was discovered that the gamma sterilization process also had a positive side effect: increased wear resistance due to a cross-linked network of the long chain molecules (Figure 1.6) (Muratoglu, Bragdon, O'Connor, Jasty, & Harris, 2001). Chain cross-linking (recombining across side groups) is favored over chain scission in the absence of oxygen. This cross-linking is thought to reduce the extent of molecular orientation, which enhances the resistance to wear by increasing strength in the transverse direction during cross-shear (Edidin et al., 1999; Wang et al., 1997). In order to take advantage of cross-linking, manufacturers began to treat ultra-high with moderate to high doses of gamma or electron-beam radiation (ranging from 5 to 10 Mrad) in an oxygen-free environment. This cross-linking was followed by a thermal treatment of heating the polyethylene above its melting temperature to subsequently neutralize residual free radicals from the gamma radiation (McKellop, Shen, Lu, Campbell, & Salovey, 1999; Muratoglu et al., 2001). Then ultra-high was cooled and machined, followed by a final sterilization procedure that often did not involve gamma radiation (gas plasma or ethylene oxide) (Ries & Pruitt, 2005). This "first-generation" of cross-linked re-melted ultra-high remains a popular choice for hip liners.

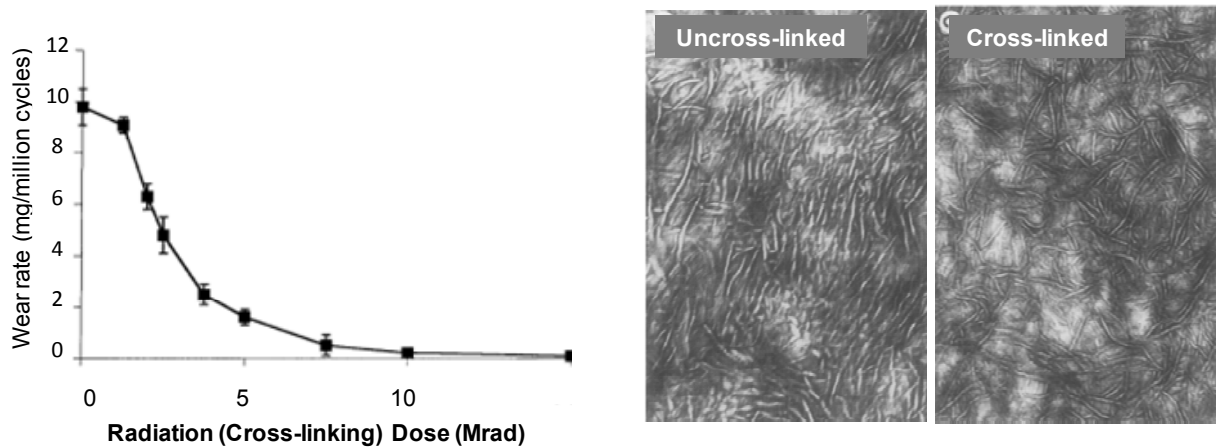


Figure 1.6. Gamma radiation cross-links the long chain molecules, which results in a low wear rate attributed to the inhibition of lamellar alignment. Modified from (left) (Muratoglu et al., 2001) and (right) (Edidin et al., 1999).

Since the late 1990s, gamma radiation to cross-link is performed in a vacuum or in an inert gas, followed by barrier packaging to prevent oxidation 'on the shelf' after sterilization. Barrier packaging varies by manufacturer, but consists of evacuating the air surrounding the implant and backfilling with an inert gas such as nitrogen or argon (S. M. Kurtz, 2009a). However, recent studies have shown that oxidation can occur in vivo despite radiation and

storage in a vacuum or an inert gas. This evidence of *in vivo* oxidation suggests that many patients are still at risk, particularly if a substantial number of residual free radicals remain in the material (Costa, Bracco, Brach del Prever, Kurtz, & Gallinaro, 2006; Currier, Currier, Mayor, Lyford, Van Citters et al., 2007; Medel et al., 2009).

By the early 2000s, it appeared that oxidative degradation had been resolved by sterilizing with ethylene oxide or gas plasma. Furthermore, cross-linking by gamma radiation in the absence of oxygen substantially reduced the wear of ultra-high (Muratoglu et al., 2001) while subsequent re-melting neutralized residual free radicals that could lead to oxidation *in vivo*. However, in the early to mid 2000s it was found that cross-linking followed by re-melting decreases the ultimate properties and fatigue crack propagation resistance of ultra-high (Baker, Bellare, & Pruitt, 2003). These results have delayed the use of highly cross-linked ultra-high in the knee where high contact stresses and the uniaxial rolling-sliding motion lead to predominantly fatigue wear processes such as delamination. Cross-linked re-melted ultra-high remains in use in the hip, where low contact stresses and cross-shearing lead to predominantly abrasive wear. However, recent reports of catastrophic fractures of the rims of highly cross-linked re-melted hip liners have clinically verified the laboratory findings of decreased fatigue crack propagation resistance (Figure 1.7) (J. Furmanski et al., 2009; Tower et al., 2007).

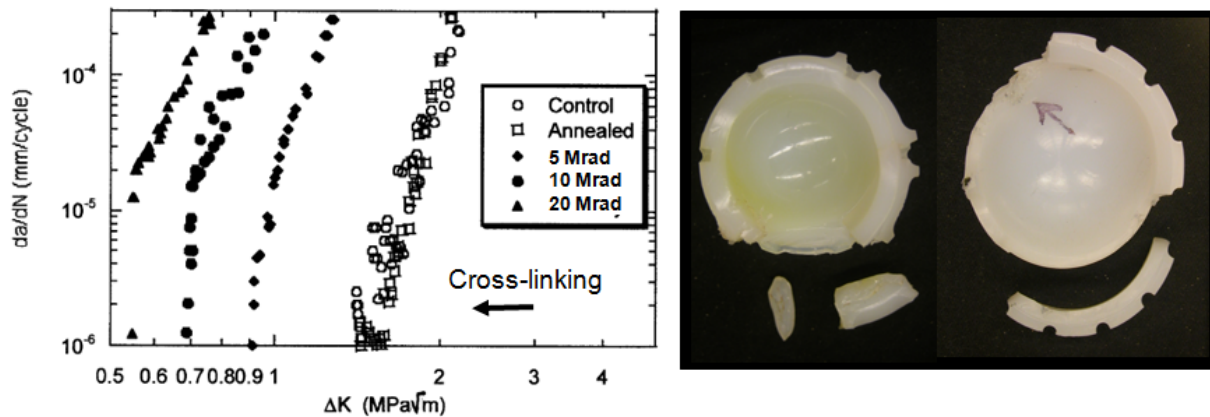


Figure 1.7. As predicted in laboratory tests, cross-linking decreases fatigue crack propagation resistance, resulting in catastrophic fracture *in vivo*. Modified from (left) (Baker et al., 2003) and (right) (J. Furmanski et al., 2009).

In the last few years, manufacturers have developed a second-generation of cross-linking and processing treatments in an attempt to increase resistance to fatigue crack propagation while maintaining wear resistance and oxidative stability. These second-generation treatments include: *annealing* highly cross-linked ultra-high below the melting temperature, applying *sequential* doses of cross-linking and annealing, and annealing a highly cross-linked ultra-high doped with a known *antioxidant* (vitamin E). The success of such treatments with respect to fatigue crack propagation, wear, and oxidation remains a subject of debate (Collier et al., 2003; Crowninshield & Muratoglu, 2008; Currier, Currier, Mayor, Lyford, Collier et al., 2007; Dumbleton, D'Antonio, Manley, Capello, & Wang, 2006; Gencur, Rimnac, & Kurtz, 2006; McKellop et al., 1999; Morrison & Jani, 2009; Wang et al., 2008) due to the paucity of full-spectrum mechanical characterization studies that provide controlled comparisons amongst multiple clinically-relevant ultra-high materials. Before these new formulations are widely implanted in hips and knees, it

must be determined how these new materials perform with respect to fatigue crack propagation, wear, and oxidation in comparison with conventional uncross-linked and cross-linked re-melted materials. Furthermore, before additional improvements in ultra-high are attempted, the relationship amongst processing treatments, microstructure, and mechanical performance must be understood rather than simply responding to the latest clinical failures.

1.4 Dissertation Aims and Study Design

The purpose of this dissertation was to evaluate the performance and elucidate the trade-offs in fatigue crack propagation resistance, wear resistance, and oxidative stability in clinically-relevant cross-linked ultra-high. Additionally, the dissertation seeks to provide insight into relationships amongst processing treatments, microstructure, and mechanical performance. For this purpose, nine distinct ultra-high groups are evaluated, of which two represent *untreated* controls, three represent *highly cross-linked re-melted* materials, two represent *moderately cross-linked re-melted* materials, and two represent *highly cross-linked annealed* materials. On these nine material groups the following tests were performed in parallel: 1) tensile tests to determine yield strength, elastic modulus, and ultimate true tensile strength and strain, 2) fatigue tests using a fracture mechanics approach to assess resistance to fatigue crack propagation, 3) multidirectional pin on disk tests to evaluate wear rate, 4) artificial aging followed by absorbance infrared spectroscopy to measure susceptibility to oxidation, and 5) scanning electron microscopy, digital image analysis, and differential scanning calorimetry to characterize the lamellar microstructure and crystallinity. A statistical analysis was also performed on the results of the mechanical tests and the microstructural characterization to determine relationships between the mechanical performance and microstructure.

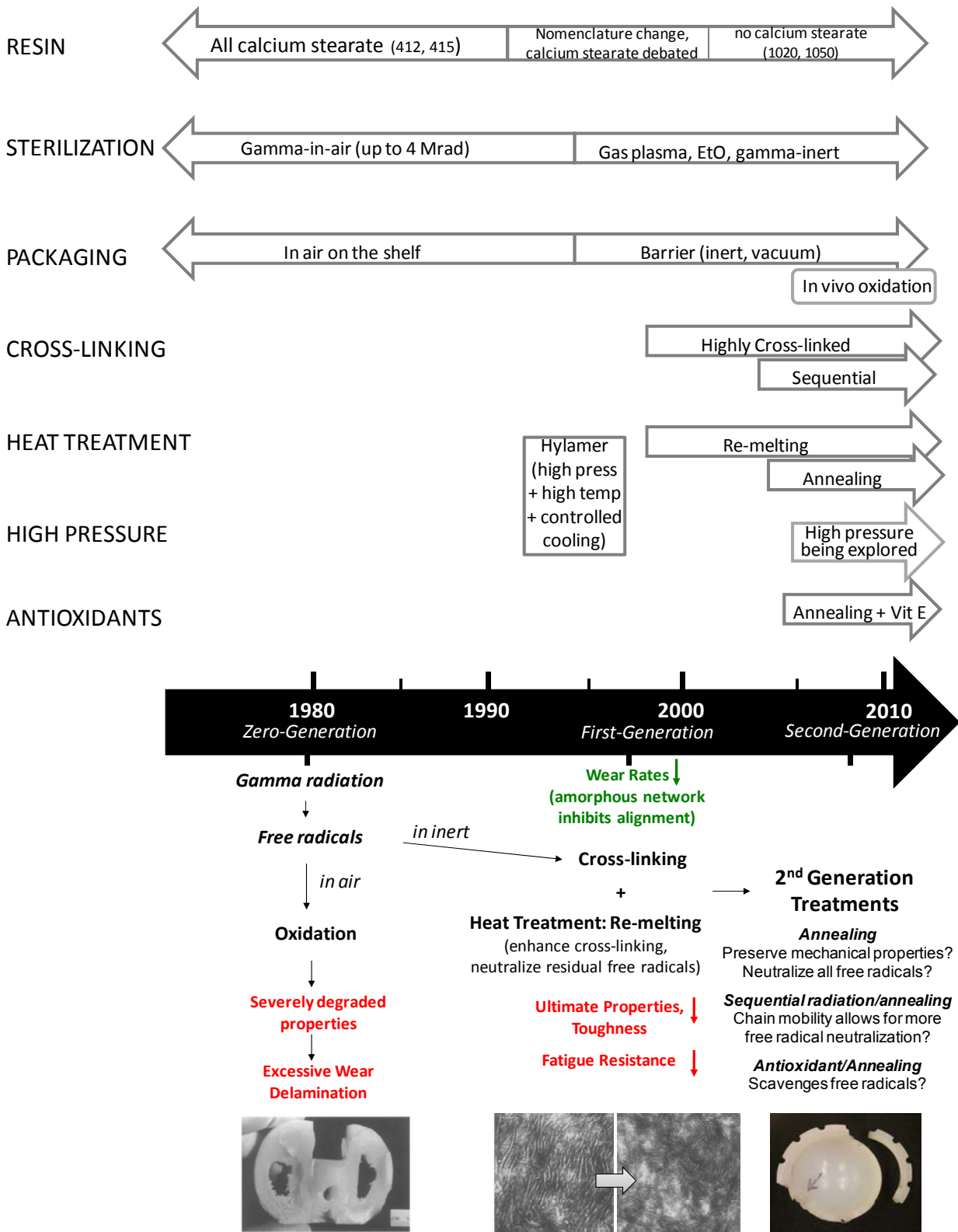


Figure 1.8. Timeline schematic of the evolution of ultra-high for orthopaedic use, motivated by clinical failures. Images are compiled from (Collier, Sperling et al., 1996; Edidin et al., 1999; J. Furmanski et al., 2009).

Chapter 2

Materials and Methods

2.1 Materials

Materials for this study included nine distinct groups of medical-grade ultra-high molecular weight polyethylene (ultra-high) that had undergone clinically-relevant processing treatments (Table 2.1). Of the nine material groups, two are untreated polyethylene controls made from different orthopaedic grade resins (GUR 1020 and GUR 1050). These control materials differ in molecular weight and in consolidation method: the GUR 1020 material has a molecular weight of 2 to 4 million grams/mol and is formed by compression molding, while the GUR 1050 material has a molecular weight of 4 to 6 million grams/mol and is formed by ram extrusion. The remaining ultra-high groups were gamma-irradiated in one or multiple doses (with a dose totaling 5 to 10 Mrad), and then heat-treated either above or below ultra-high's melting temperature of 135°C (S. M. Kurtz, 2009d) (130°C for 8 hours or 147°C for 2 hours). All cross-linked groups were also either compression-molded GUR 1020 or ram-extruded GUR 1050. The material groups are referred to throughout this work as RESIN – RADIATION DOSE (Mrad) – HEAT TREATMENT (°C), for example 1020-9-130 represents a GUR 1020 resin irradiated to a dose of 9 Mrad and subsequently annealed at 130°C.

Material Group	Resin	Radiation Dose Mrad	Heat Treatment °C
1020-0-0	1020	None	None
1050-0-0	1050	None	None
1020-3x3-130	1020	3x3	3 x 130 for 8 hours
1020-9-130	1020	9	130 for 8 hours
1020-5-147	1020	5	147 for 2 hours
1020-7.5-147	1020	7.5	147 for 2 hours
1020-9-147	1020	9	147 for 2 hours
1020-10-147	1020	10	147 for 2 hours
1050-10-147	1050	10	147 for 2 hours

Table 2.1. Ultra-high molecular weight polyethylene groups tested. Material groups are labeled with the key: resin-radiation dose (Mrad)-heat treatment (°C).

The groups include combinations of base resin, radiation dose, and heat treatment that are similar to clinical materials from major device manufacturers (Figure 2.1). Specifically, the 1050-10-147 material represents XLPE™ from Smith and Nephew, the 1020-5-147 material is similar to XLK from DePuy (marketed in knee as well as hip replacements), and the 1020-3x3-130 material is analogous to X3™ from Stryker. Additional materials in this study are comparable to other marketed materials from Zimmer with slight variations; except for the initial warming step and the fact that the radiation source is electron beam instead of gamma, the 1020-9-147 and 1020-10-147 are similar to Durasul® and Longevity®. All of the materials in the study were processed with clinically-relevant resins, radiation doses, and subsequent thermal

treatments (Figure 2.1). None of the materials were sterilized after machining, and data on cooling rates during thermal processing were not provided but were reported to be consistent across groups.

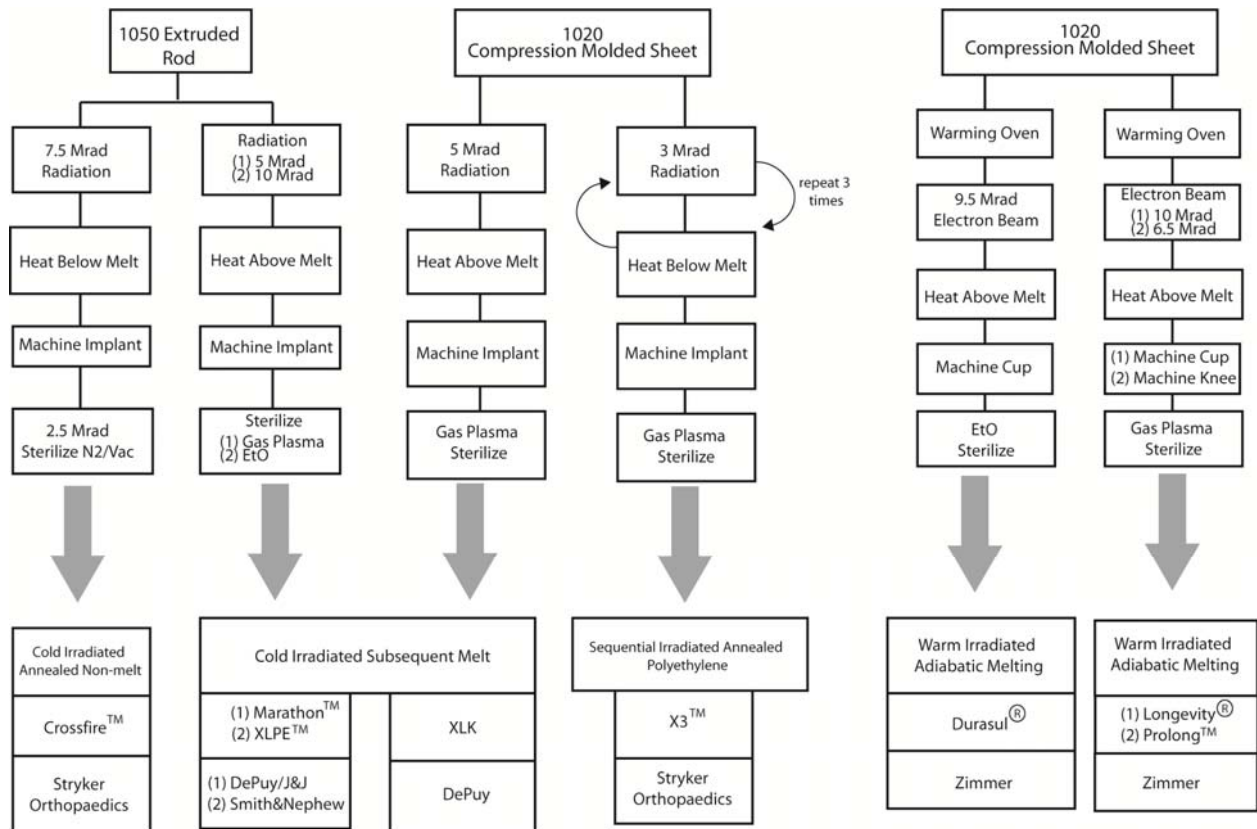


Figure 2.1. Ultra-high materials and processing treatments produced by device manufacturers (modified from (Ries & Pruitt, 2005)).

2.2 Methods

2.2.1 Tensile testing

To evaluate the materials' mechanical properties, tensile tests were performed on three dog-bone specimens for each material group. The dog-bone specimens were machined to the ASTM type V geometry with a thickness of 1.50 mm (Figure 2.2). Before testing, dimensions of each specimen were measured using digital calipers (± 0.01 mm). Tensile tests were run on an Instron 8871 servohydraulic load frame (Norwood, MA) using displacement-control at a rate of 5 mm/min (Baker et al., 2003). The tests were performed at room temperature with air jet cooling directed at the gage section of the specimen. The load and displacement data were converted into engineering stress and strain using measured initial dimensions. The engineering stress and strain data were used to determine the yield strength (where the stress decreased slightly with increasing strain) and the elastic modulus (the secant modulus at 2% strain). A high-resolution digital microscope consisting of a variable magnification optical system (Infinivar CFM-2/S,

Boulder, Colorado, pixel size 5 μm) and a digital CCD video camera (Sony XCD-SX910, Tokyo, Japan) captured a sequence of images during the test with a resolution of 5 μm , taken at a rate of approximately one image per second. Using the specimen dimensions in the image captured just before failure, the ultimate true tensile strength and ultimate true strain at failure were determined.

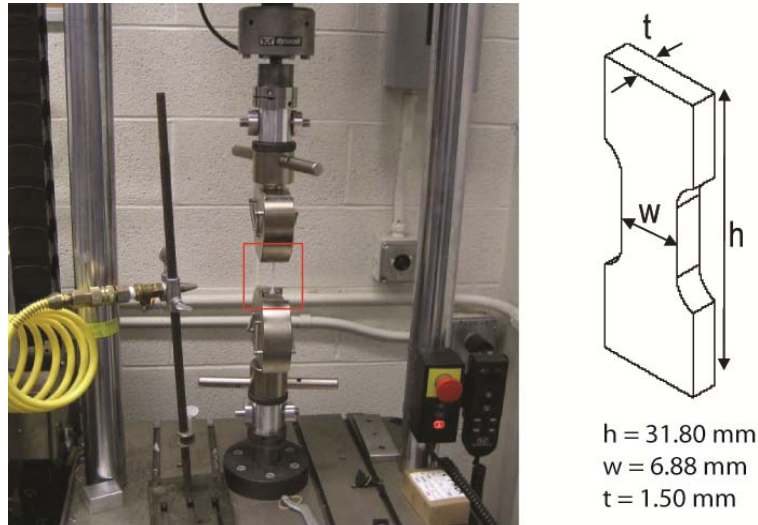


Figure 2.2. Tensile testing setup on servohydraulic load frame with specimen dimensions.

2.2.2 Fatigue Crack Propagation Testing

To evaluate the materials' resistance to fatigue crack propagation, fatigue tests were performed using a fracture mechanics (defect tolerant) approach on four to six compact tension specimens for each material group. The compact tension specimens (Baker et al., 2003) were machined with a 1 mm deep, 40° side groove on both sides of the specimen in the crack plane to allow for more accurate crack measurement and a more even distribution of stress through the thickness of the specimen (Shih, Lorenzi, & Andrews, 1977). The tip of the notch was sharpened with a razor blade before testing. The crack propagation direction corresponded to the ram extrusion direction in the GUR 1050 materials. Fatigue tests were run on an Instron 8871 servohydraulic load frame (Norwood, MA) using a load-controlled sinusoidal wave function at a frequency of 5 Hz. The fatigue tests were performed under ambient conditions with a room-temperature air-jet directed at the crack tip to mitigate hysteretic specimen heating. The sinusoidal load was applied at a constant load ratio of 0.1 (defined as the ratio of the minimum load to the maximum load of the fatigue cycle). After 10,000 load cycles, the load was increased, maintaining a load ratio of 0.1 (for example, 30 to 300N, then 40 to 400 N, etc) (Figure 2.3). This process was repeated throughout the stable crack growth regime until the specimen fractured. Crack advance was quantified after each 10,000 cycles by measuring the distance between the crack tip and fiducial lines marked on the specimen surface using the high-resolution digital microscope and camera system described above. This fatigue crack propagation testing procedure has been validated and performed extensively in the Berkeley Medical Polymers laboratory (Baker et al., 2003; Baker, Hastings, & Pruitt, 2000; Jevan Furmanski & Pruitt, 2007; L. Pruitt & Bailey, 1998).

With the crack advance data, the prescribed loading, known specimen geometry, and measured number of cycles, the crack growth per cycle (da/dN in mm/cycle) can be related to the range of stress intensity driving the crack propagation (ΔK in $\text{MPa}\sqrt{\text{m}}$). The range of stress intensity is defined as

$$\Delta K = F\Delta\sigma \sqrt{\pi a} \quad (2.1)$$

in which F is a specimen-specific geometrical factor described previously (Baker et al., 2000), $\Delta\sigma$ is the range of far-field applied stress (MPa), and a is the crack length (m). In the stable crack growth regime, the Paris equation relates the stress intensity to the crack growth per cycle according to:

$$da/dN = C(\Delta K)^m \quad (2.2)$$

in which C and m are parameters that depend on the material, environment, frequency, temperature and stress ratio. On a log-log plot of crack velocity versus the stress intensity range, m and C represent the slope and intercept, respectively.

Linear regression was used to relate the logarithm of crack growth per cycle (continuous outcome variable) to the logarithm of stress intensity (continuous predictor variable), and to statistically compare values of C and m (STATA v. 9, College Station, TX). A full linear regression model was initially fit including indicators and cross-products to allow for statistical differences in intercept and slope amongst the groups. Full versus restricted F-tests were performed to determine whether various intercepts and slopes should be kept in the model. A cutoff of $p < 0.05$ was used to conclude that particular intercepts or slopes were statistically different from others.

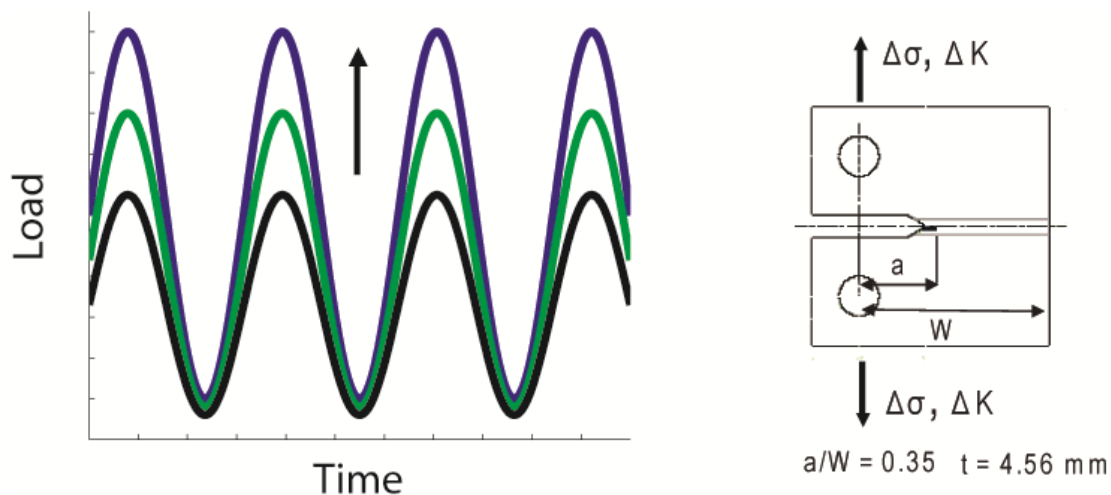


Figure 2.3 Schematic showing fatigue crack propagation tests performed with a constant R-ratio (0.1) and increasing sinusoidal loading (modified from (Jevan Furmanski & Pruitt, 2007)), and the compact tension specimen and dimensions.

2.2.3 Wear Testing

To evaluate the wear resistance of the materials, multidirectional sliding wear tests were performed using a custom pin-on-disk tribotester (Figure 2.4) (Patten, 2008). The bearing couple comprised a spherically-tipped ultra-high pin (3.28 mm radius) against a flat CoCr disk (127 mm diameter). The tribotester consisted of a retrofitted vertical-knee milling machine with the drilling head replaced with a vertical mounting table. The pins and loading system were attached to the vertical table, while the disks and load cells were attached to the horizontal table below. The pins were held in collets on vertical rails and the load was adjusted using individually-controlled pneumatic actuators. The ultra-high pins were held stationary throughout the test while the horizontal table on which the CoCr disks were mounted moved in a defined x-y motion using computer numerical control (National Instruments LabVIEW v8.5 and Motion Assistant v2.2, Austin, TX). The CoCr disks translated along a circular path (8 mm diameter) without rotation, achieving multidirectional sliding with cross-shear on the ultra-high bearing surface.

The CoCr disks were polished to an arithmetic average roughness of less than 0.03 microns as measured at multiple locations using a stylus profilometer (Dektak IID, Sloan Technology Co., Santa Barbara, CA). Before testing, the ultra-high pins and CoCr disk were ultrasonically cleaned in acetone, isopropyl alcohol, and deionized water. Two pins were tested for each material group.

The wear test conditions were chosen to be clinically relevant (Table 2.2) (Klapperich, Komvopoulos, & Pruitt, 1999; Zhou & Komvopoulos, 2005). The normal load of 12 ± 2.5 N results in a mean contact pressure of 25 ± 5 MPa, which is similar to conditions found in total joint replacements (Bartel et al., 1986). The linear speed of 35 mm/s simulates speeds found in joint replacements during normal activity such as walking and running (J. Fisher, Dowson, Hamdzah, & Lee, 1994). The lubricant was bovine serum diluted 1:1 with deionized water and preserved with 0.1 wt% sodium azide. All tests were performed in an ambient laboratory environment. Air and serum temperatures were monitored throughout the test; serum temperature was consistently 1-2 degrees warmer from frictional heating. Tests were run for 500,000 cycles to establish a steady-state wear rate after the run-in period.

Wear Test Parameters	
Wear path	Circularly translating, 8 mm diameter
Normal load	10-15 N
Mean contact pressure	20-30 MPa
Linear speed	35 mm/s
Sliding distance	12.5 km
Number of cycles	500,000
Lubricant	Bovine serum ^a
Environment	~ 25°C, Ambient

^a diluted 1:1 with deionized water, preserved with 0.1 wt% sodium azide

Table 2.2. Wear test parameters for multidirectional pin-on-disk testing.

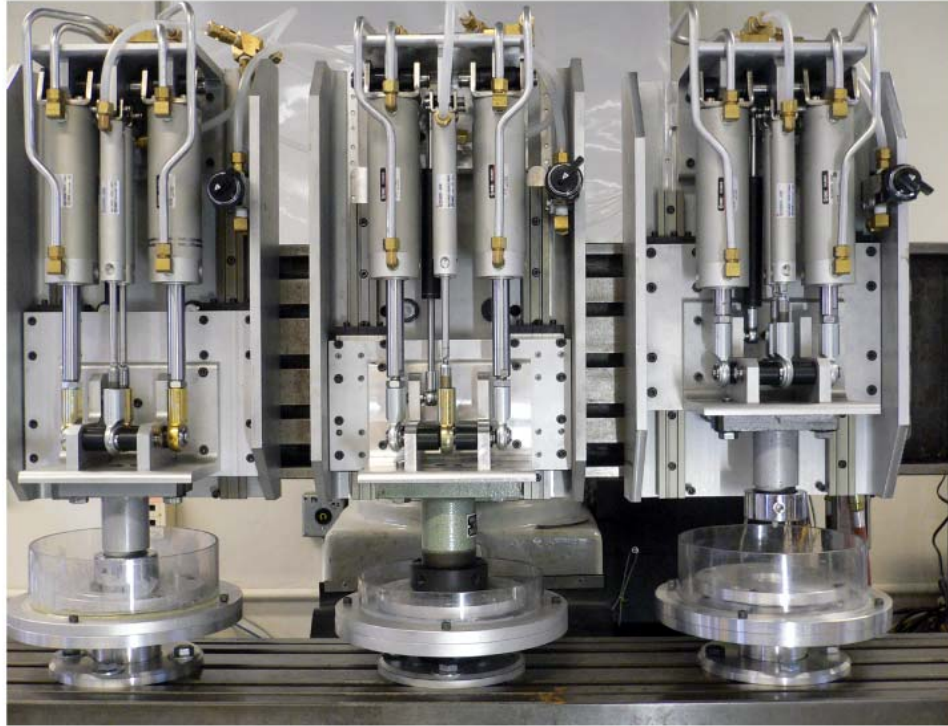


Figure 2.4. Custom pin-on-disk tribotester: the vertical table on top holds the ultra-high pins and is kept stationary while the horizontal table below holds the CoCr disk and moves with X-Y motion control from a retrofitted CNC milling machine. Loading is controlled using independent pneumatic actuators and is monitored by load cells mounted below the disk holders.

The diameter of the wear scar on the pin was measured every 50,000 cycles using the high-resolution digital microscope described above. An image analysis program (National Instruments LabVIEW v. 8.5) was used to fit a circle to the wear scar and report the diameter. The wear was calculated volumetrically as the volume (in mm^3) of material lost, V , from the spherically-ended ultra-high pin according to the equation

$$V = \frac{\pi h}{6} (3a^2 + h^2) \quad (2.3)$$

where a is the measured radius of the worn circular area, and h is the thickness of the worn layer given as

$$h = R - \sqrt{R^2 - a^2} \quad (2.4)$$

where R is the radius of the hemispherical end of the pins (Figure 2.5).

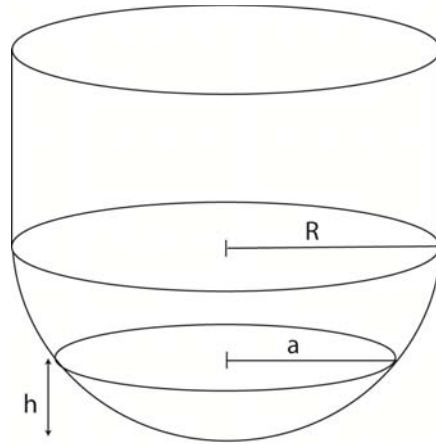


Figure 2.5. Geometry of hemispherical ended pin for wear volume calculation

The wear rate was then calculated as the wear volume divided by the number of cycles. Wear resistance was based on the steady-state wear rate achieved by the materials beyond 300,000 cycles. The steady-state wear data taken after 300,000 cycles (roughly 72 hours) is substantially beyond ultra-high's transient creep period of about 24 hours (Klapperich et al., 1999).

Investigations were performed to determine the accuracy and the effect of creep on the wear measurement. To determine wear volume measurement accuracy, the wear scars on the pins were measured using the image analysis system multiple times, producing an estimate of the largest and smallest circles that could be fit to the image. These ranges were then used to calculate the variation in the wear volume and wear rate measurement. This was done for all material groups to ensure that the variation in measurement was consistent.

To determine the effect of creep on the wear measurement, images of selected wear pins were taken approximately two months after testing to determine changes in geometry resulting from creep recovery. The analysis presented above assumes that the worn surface of the pin is flat when viewed in cross-section. However, creep would affect the worn surface by pressing the hemispherical end of the pin into a flat shape (attributed to wear), when in fact over time the pin bulges out again (resulting in an overestimation of the wear volume) (Figure 2.6).

A subset of wear pins were imaged in cross-section using the image analysis technique and equations presented above to determine the radius and height of the recovered bulge. This recovered volume was then subtracted from the original wear volume assuming no creep contribution. The materials were chosen for this investigation based on material availability and the order in which wear tests were run.

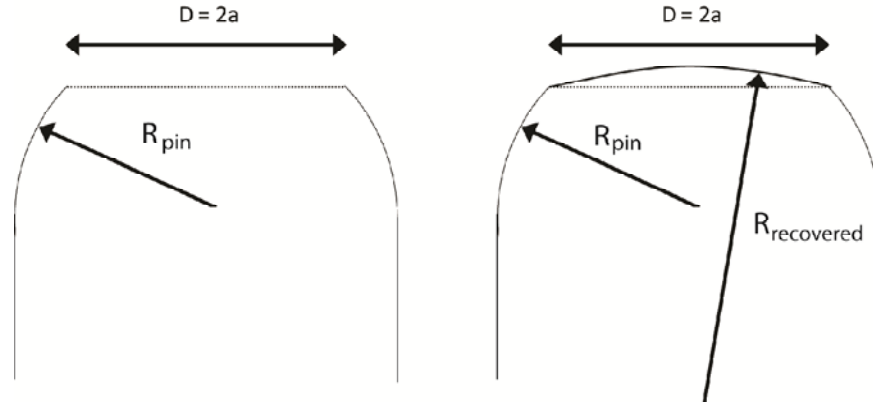


Figure 2.6 Cross-section view of the wear pin showing (left) original wear volume measurement assuming surface to be flat and (right) changes in wear volume measurement due to creep recovery

Analysis of variance (ANOVA) was used to determine statistically significant differences amongst the steady-state wear rates of the material groups beyond 300,000 cycles (STATA v. 9). Multiple post-hoc comparisons were taken into consideration using the Student-Newman-Keuls (SNK) procedure. The Student-Newman-Keuls procedure increases the power of detecting a difference by arranging the means in increasing order and performing one-tailed t-tests, while still controlling the overall false-positive error ($\alpha = 0.05$) for the family of comparisons spanning a given number of means (Glantz, 2005). The q-statistic for the test is defined as

$$q = \frac{\bar{X}_A - \bar{X}_B}{\sqrt{\frac{s_p^2}{2} \left(\frac{1}{n_A} + \frac{1}{n_B} \right)}} \quad (2.5)$$

where \bar{X}_A and \bar{X}_B are the two means being compared, s_p^2 is the pooled variance, and n_A and n_B are the sample sizes of the two groups being compared (Glantz, 2005). The cutoff values to which the q-statistic is compared were interpolated from tabulated values (Glantz, 2005). The minimum power to detect a $0.6 \times 10^{-7} \text{ mm}^3/\text{cycle}$ difference (about twice the typical standard deviation) in wear rate is about 0.85, given 9 material groups, 6-8 data points per group, and an overall $\alpha = 0.05$ (Glantz, 2005; Lenth, 2006-2009).

2.2.4 Oxidation following Artificial Aging

To assess the oxidative stability of the materials, artificial aging and absorbance spectroscopy were performed with colleagues at the Dartmouth Biomedical Engineering Center. To artificially age the materials, one sample for each group (10mm x 10mm x 10mm) was placed in a pressure vessel with 3 atm O₂ at 63° C for 28 days (an environment less aggressive than ASTM-2003 Method A). Subsequently, oxidation in the material was measured by Fourier transform infrared spectroscopy on 200 micron-thick cross-sections of each sample (Jung microtome, Heidelberg, Germany). Incorporation of oxygen into the material was measured using a Perkin Elmer AutoImage Infrared Microscope (Waltham, MA) with 32 scans per 100 μm depth interval, wavelength 2 cm^{-1} , and aperture 100 μm^2 . The oxidation index was defined as the

measured 1715 cm^{-1} (ketone) peak height normalized to the 1368 cm^{-1} peak height (Currier, Currier, Mayor, Lyford, Van Citters et al., 2007). This artificial aging and absorbance spectroscopy protocol has been validated and extensively studied at the Dartmouth Biomedical Engineering Center (Collier, Sperling et al., 1996; Currier, Currier, Collier, Mayor, & Scott, 1997; Currier, Currier, Mayor, Lyford, Van Citters et al., 2007; S. M. Kurtz et al., 2001).

It is important to note the peaks used in the definition of the oxidation index (Figure 2.7). The area of interest is the carbonyl region between 1800 and 1660 cm^{-1} , which measures the carbon-oxygen double bonds indicating the presence of ketone, ester, aldehyde, and carboxylic acid (S. M. Kurtz et al., 2001). However, it has been found that retrieved implants and ultra-high exposed to bovine serum during testing may absorb esters (1738 cm^{-1}) on the surface (Costa, Bracco, del Prever, Luda, & Trossarelli, 2001). This absorption results in overestimation of the oxidation index if the entire carbonyl peak is considered (recommended in the ASTM standard F2102 (ASTM, 2001)). Therefore, the oxidation index definition in this study employs a narrower keytone peak height from 1713 to 1717 cm^{-1} to exclude the ester peak. Although the materials in this study are not exposed to absorbed species, this protocol makes the results comparable to other studies from the Dartmouth Biomedical Engineering Center and to future studies of retrieved implants that use these particular formulations of ultra-high. In addition, ongoing work at Dartmouth indicates that the Dartmouth oxidation index scales linearly with the ASTM standard (D. W. Van Citters, 2006).

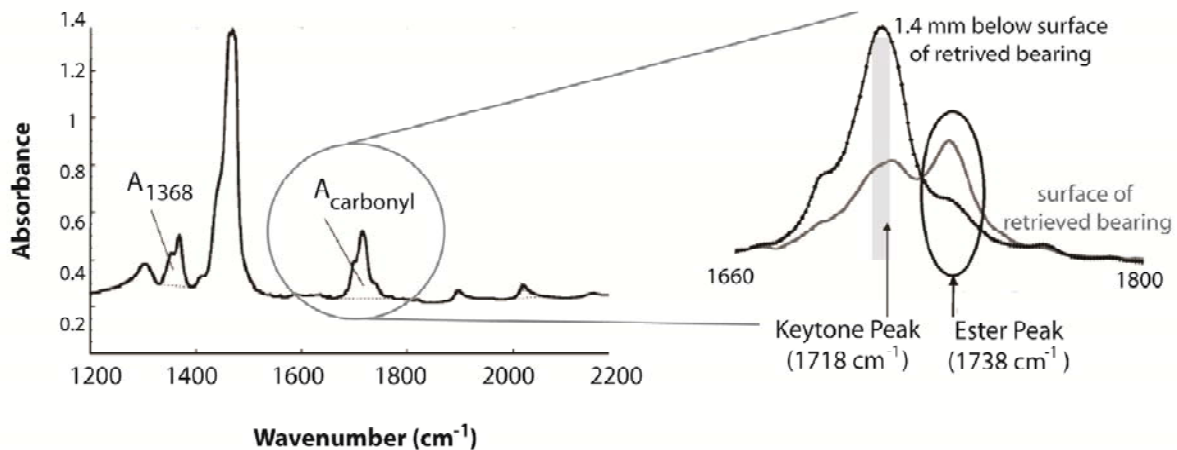


Figure 2.7. Typical Fourier transform infrared spectroscopy scan of oxidized ultra-high showing the carbonyl region and the definition of the keytone peak height used in the oxidation index (modified from (Currier, Currier, Mayor, Lyford, Van Citters et al., 2007; S. M. Kurtz et al., 2001)).

2.2.5 Microstructure

To elucidate the relationship amongst microstructure, processing treatments, and performance, the materials' lamellar structure and crystallinity was assessed qualitatively using scanning electron microscopy and quantitatively using differential scanning calorimetry and image analysis. The microstructural parameters in this study are limited to lamellar properties and do not include amorphous properties such as cross-link density.

Etching and Scanning Electron Microscopy

To obtain images of the crystalline lamellae, two samples from each material group were etched to preferentially remove the amorphous phase, and then imaged with a scanning electron microscope. Before etching, each sample (2 mm x 2 mm x 6 mm) was microtomed using a glass knife (Reichert Ultracut E, Depew, NY) to obtain a smooth surface. The sample was then subjected to a potassium permanganate etching procedure developed by Olley (Olley & Bassett, 1977) that preferentially removes the amorphous phase occupying the space between the lamellae. The samples were then sputter-coated with gold-palladium (Tousimis Sputter Coater, Rockville, MD) and imaged using a field-emission scanning electron microscope (Hitachi S-5000, Pleasanton, CA) at the Berkeley Electron Microscope Facility. Digital images of the lamellae were taken at a magnification of 20,000 times with an accelerating voltage of 30 kV, resulting in a resolution of 4 nanometers.

Differential Scanning Calorimetry

To assess the percent crystallinity, differential scanning calorimetry was performed on three samples of each material group. Samples of approximately 10 milligrams were subjected to a thermal scan from 50 to 180°C at a rate of 10°C per minute (Perkin Elmer, Waltham, MA). The thermal rate and sample size are within validated ranges (Meng & Kathryn, 1998; Pascaud, Evans, McCullagh, & FitzPatrick, 1996). The specific sample size was chosen because larger samples exhibited a lack of thermal conductivity, while smaller samples had more substantial error associated with sample weight.

The thermal scan produced an endothermic graph of heat flow as a function of temperature, normalized to the sample mass (Figure 2.8). The enthalpy of melting was determined by integrating the entire melting endotherm from 80 to 160°C and normalizing to the sample mass (TA Instruments Universal Analysis v. 3.1E, New Castle, DE). Wide bounds on the melting endotherm were chosen to reduce the effect of shifting melting temperatures amongst the material groups. Percent crystallinity was calculated by normalizing the enthalpy of melting for a particular sample to that for a pure ultra-high crystal (293 J/g) (S. M. Kurtz, 2009d).

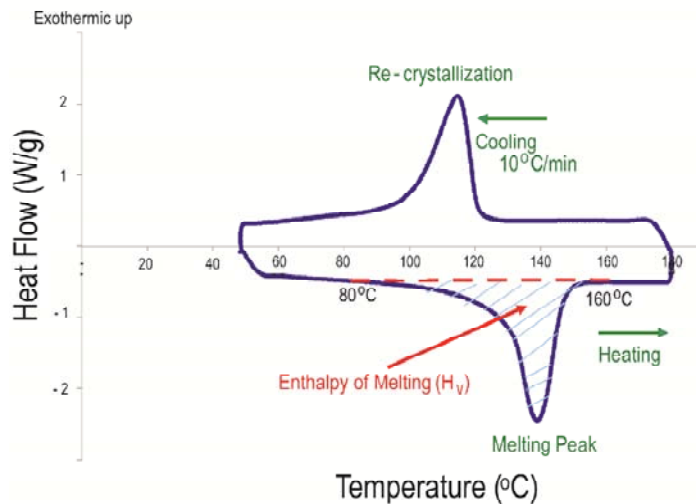


Figure 2.8. Typical differential scanning calorimetry graph showing the enthalpy of melting (the area under the melting peak), which is normalized to that of a pure ultra-high crystal to determine percent crystallinity.

Image Analysis

To quantify the lamellar dimensions observed in the scanning electron micrographs, image analysis was performed on one representative image (5 x 5 microns) for each material group (National Instruments LabVIEW v. 8.5). The image analysis consisted of a user-defined threshold of the image and a series of standard filters that separated or eliminated large tangled clumps of lamellae, small round corners of lamellae, and lamellae touching the edge of the image (Figure 2.9).

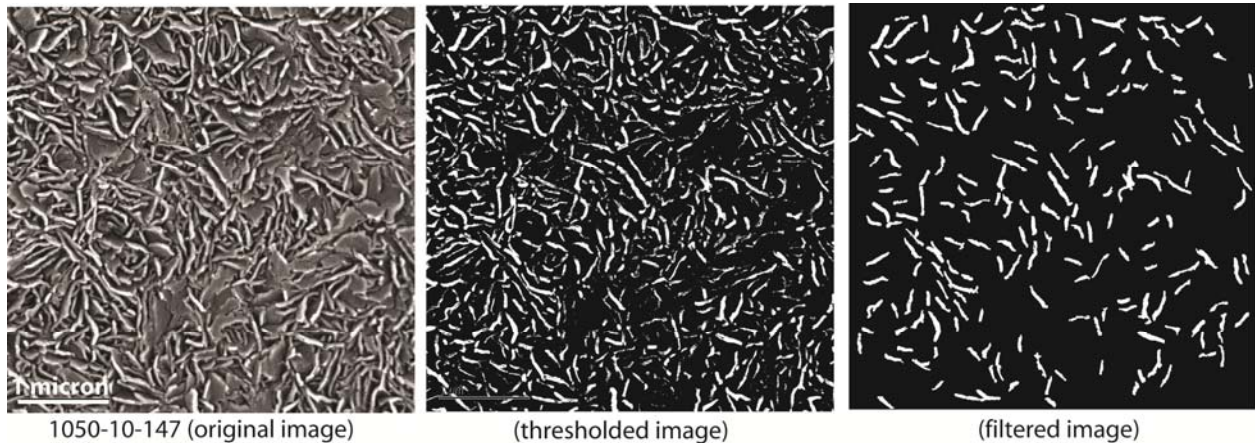


Figure 2.9. Image analysis software was used to digitally threshold and filter original scanning electron micrographs to visualize cross-sections of representative lamellae. On each processed image, pixels were counted and scaled dimensionally to obtain distributions of lamellar cross-sectional area, thickness, and length

First, the image was converted into a binary image and the user prescribed a brightness level to delineate the lamellae from their surroundings. This thresholding process is user-defined, but target brightness levels to indicate light cross-sections of lamellae were around 128 (0 is black, 255 is white). An upper threshold was also set around 250 to eliminate noise pixels. Next, a series of filters was applied to the binary image: proper open, Heywood circularity, and percent area. The proper open function smooths the boundaries of the lamellae and removes small noise particles without changing the area of the lamellae. The Heywood circularity function identifies nearly circular objects (corners of lamellae, large tangled clumps of lamellae, v-shaped lamellae) by calculating the ratio of the contour perimeter of the object to the perimeter of a circle with the same area. Objects with Heywood circularity greater than 1.3 were determined to be representative lamellae and were kept in the image. The percent area function compares the area of the object with the area of the entire image. Small noise particles were determined to be those below 1%. This effectively eliminated any pixels on the sides of lamellae remaining after the threshold. Lamellae touching the edge of the image were also removed as these were likely only portions of full lamellae and were therefore not representative.

After the thresholding and filtering, a best-fit rectangle was fit to each remaining lamellar object and the pixel dimensions of the rectangle were converted to nanometers using spatial calibration of the scale bar on the image (resolution of 4 nanometers). The individual objects were two-dimensional cross-sections of plate-like lamellae that were characterized by a thickness (short dimension of best-fit rectangle), a length (long dimension of best-fit rectangle), and an

area (number of pixels of the object). Each image contained about 200 lamellar objects upon which relative magnitudes and distributions for lamellar thickness, length, and area were based.

This image analysis technique (Medical Polymers Group, or MPG, technique) was compared to other methods for determining lamellar dimensions, including differential scanning calorimetry, a thermodynamic theory-based image analysis technique developed independently by Van Citters (D. W. Van Citters, 2006), and ultra small angle x-ray scattering.

Differential scanning calorimetry determinations of melting temperature and the enthalpy of melting can be combined with the Hoffman-Weeks relation to determine an average crystal (lamellae) thickness:

$$t = \frac{2 \sigma_c T_m^0}{\Delta H_v (T_m^0 - T)} \quad (2.6)$$

where σ_c is the surface energy (9×10^{-6} J/cm²), T_m^0 is the pure crystal melting temperature, ΔH_v is the change in enthalpy with melting, and T is the measured melting temperature (Hoffman & Miller, 1997; Hoffman & Weeks, 1962). However, this equation was developed for uncross-linked ultra-high and does not hold for cross-linked ultra-high due to the larger distribution of lamellar thicknesses. This method was still used to validate the MPG image analysis approximation of the thickness of the two untreated control materials.

Lamellar parameters were also determined using an independent image analysis technique developed by Van Citters based on the Hoffman-Weeks relation (D. W. Van Citters, 2006). The Van Citters (DVC) technique uses the object count from image analysis in combination with results from differential scanning calorimetry. The details are provided elsewhere (D. W. Van Citters, 2006). Ultimately, an equivalent lamellar thickness and an equivalent lamellar diameter are determined based on the assumption that the thickness grows linearly with the diameter. Equivalent lamellar size was calculated as the equivalent thickness times the equivalent diameter, giving a two-dimensional cross-sectional area through the largest section of the disc-shaped lamellae. These measures are related to the MPG lamellar thickness, lamellar length, and lamellar area, respectively.

Finally, the MPG image analysis technique was performed on scanning electron micrographs of ultra-high materials from another study that were also subjected to ultra-small angle x-ray scattering (Simis, Bistolfi, Bellare, & Pruitt, 2006). X-ray scattering is commonly used for reporting lamellar thickness (Bistolfi, Turell, Lee, & Bellare, 2009; Turell & Bellare, 2004). The x-ray scattering method applied to ultra-high is based on the theory of using diffraction to determine interatomic distances of crystalline materials with simple cubic long-range order, such as metals. The resolvable limit of the structure of interest is dependent on the scattering vector q (nm⁻¹) through

$$q = \frac{2\pi}{d_{hkl}} = \frac{4\pi}{\lambda} \sin\theta \quad (2.7)$$

where λ is the x-ray wavelength (nm), d_{hkl} is the distance between adjacent planes (nm), and θ is one-half the Bragg angle, defined by Bragg's law

$$n\lambda = 2 d_{hkl} \sin\theta \quad (2.8)$$

where n is an integer. Therefore, the smaller the scattering vector, the larger the resolvable structural feature. *Ultra-small* angle x-ray scattering is necessary for determining ultra-high lamellar parameters because it can detect features from about 1 nanometer up to hundreds of microns, while small angle x-ray scattering cannot measure structure in the micrometer scale characteristic of the crystalline lamellae (Baker, Pruitt, & Bellare, 2001; Bellare, Schnablegger, & Cohen, 1995; Turell & Bellare, 2004).

With a semi-crystalline polymer such as ultra-high, the plate-like crystalline lamellae are analogous to planes of ordered atoms from which diffraction occurs, but at a much larger size scale because the diffraction angles are near zero. Similarly, the distance between adjacent planes for a certain $\langle hkl \rangle$ orientation in a traditional crystal (d_{hkl}) is replaced in this application with the long period L , or distance between adjacent lamellae separated by the amorphous phase in between (Figure 2.10).

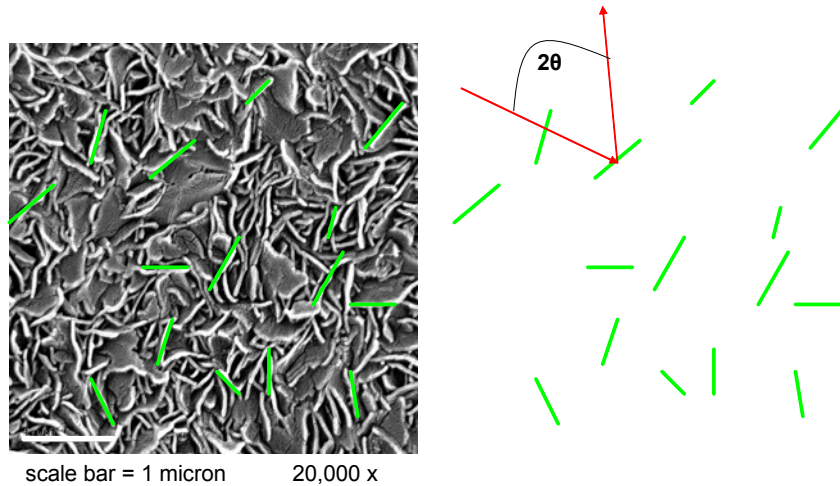


Figure 2.10. Ultra-high lamellae can be considered analogous to scattering planes of atoms to determine inter-lamellar spacing using x-ray scattering.

To calculate the lamellar thickness, the inter-lamellar spacing obtained from x-ray scattering is multiplied by the percent crystallinity obtained by differential scanning calorimetry (Figure 2.11).

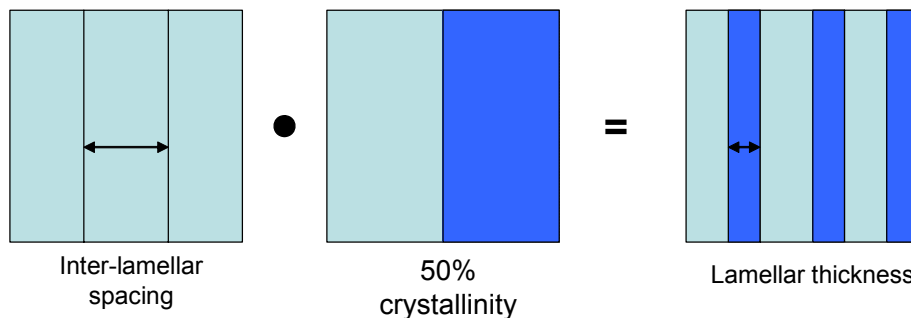


Figure 2.11. After x-ray scattering, determination of lamellar thickness depends on percent crystallinity obtained from differential scanning calorimetry.

2.2.6 Statistical Analysis of Pair-wise Correlations

Finally, to determine relationships amongst microstructural properties and mechanical performance, a statistical analysis was performed using the non-parametric Spearman rank correlation coefficient (STATA v. 9). The non-parametric analysis accounts for small sample sizes and non-normal distributions observed for some outcomes. For the estimates, 75th percentile values of mechanical and microstructural properties were used because the image analysis procedure eliminates lamellae below a given size and skews the distribution. Fatigue crack propagation resistance was quantified as the value for the range of stress intensity corresponding to a da/dN of 10^{-5} mm/cycle (this captures the left-to-right shift of the fatigue curves in the Paris regime and is related to the stress intensity required for the inception of crack propagation (Baker et al., 2003)).

Chapter 3

Results

3.1 Tensile Behavior

The mechanical properties (yield strength, elastic modulus, and ultimate true stress and strain, Figure 3.1) of the cross-linked materials depended on the type of heat treatment, the radiation dose, and the resin and consolidation method. Elastic modulus and yield strength were higher for annealed materials and lower for re-melted materials, with secondary dependence on radiation dose. Alternately, the ultimate properties generally decreased with increased radiation dose, regardless of heat treatment. Mechanical properties also depended on the resin and consolidation method. The GUR 1050 materials had lower yield strength and elastic modulus compared to GUR 1020 materials with the same heat treatment and radiation dose, but ultimate properties were about the same (Figure 3.2).

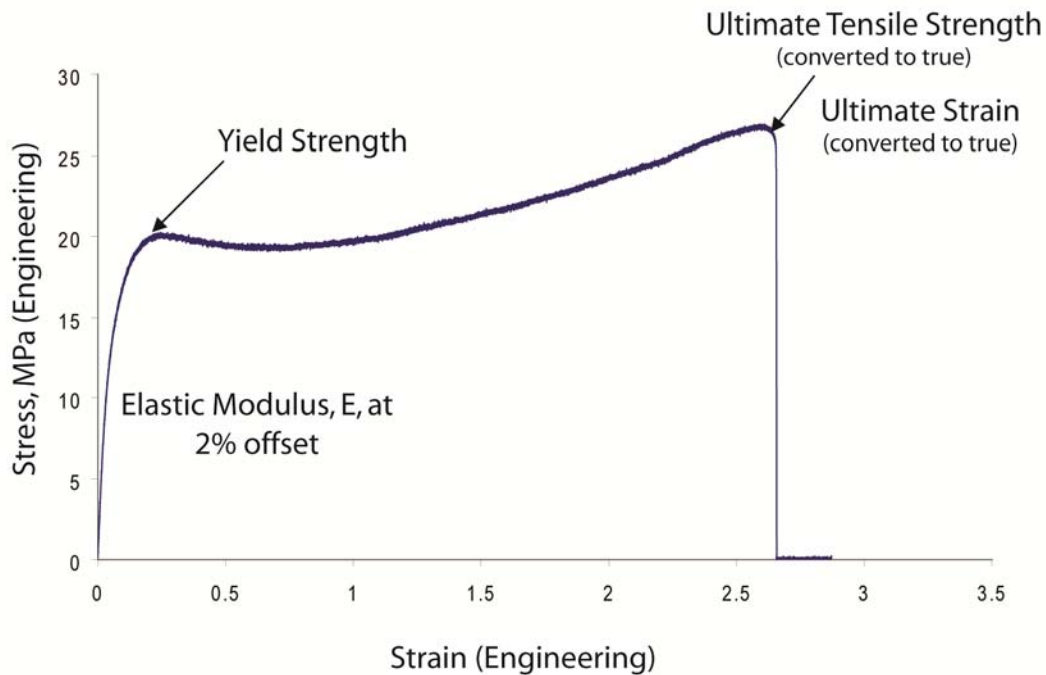


Figure 3.1. Typical stress-strain curve for the ultra-high materials showing tensile properties determined from the experimental curves.

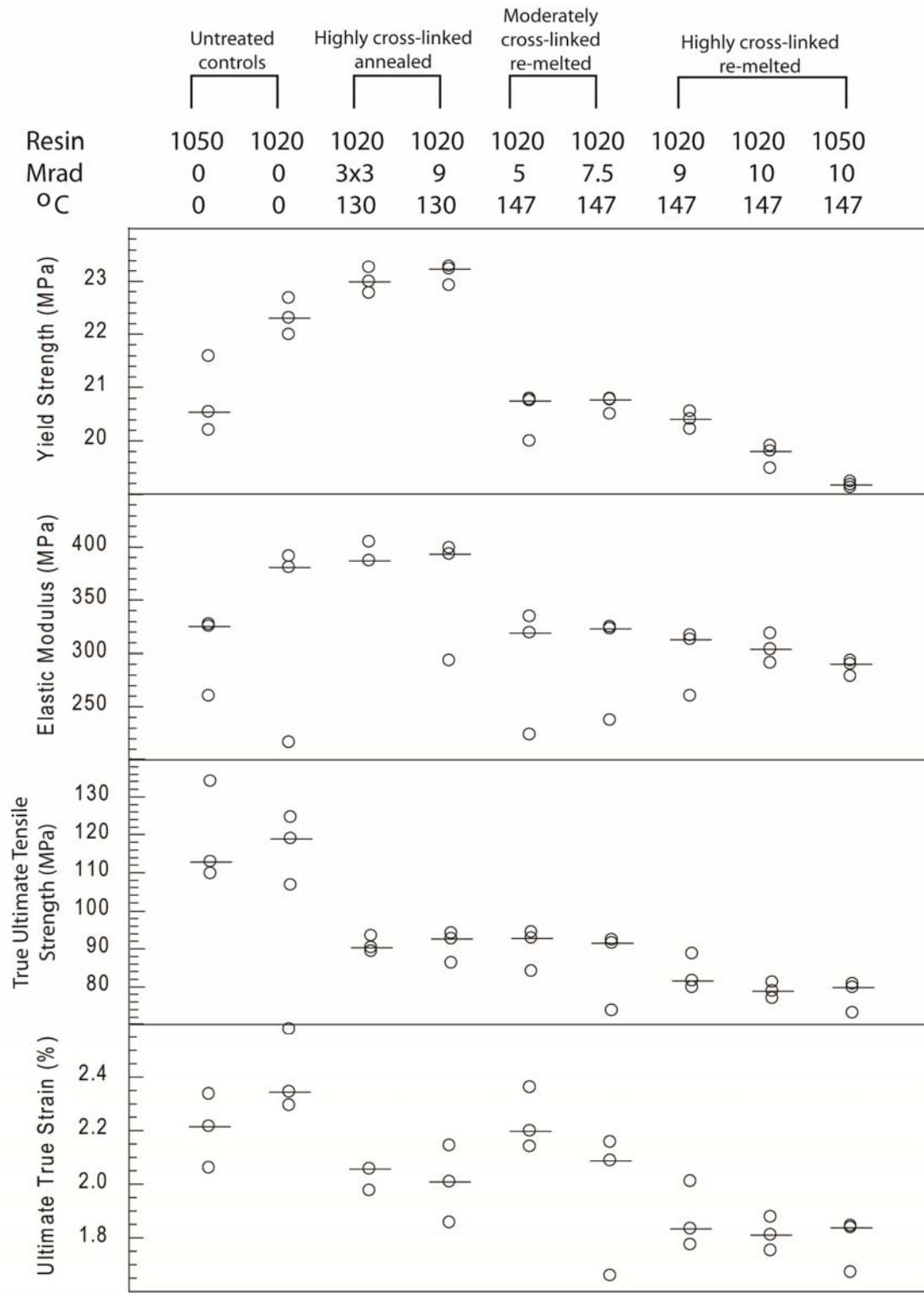


Figure 3.2. Tensile properties for all materials. Yield strength and modulus of cross-linked annealed materials are higher than untreated controls, while cross-linked re-melted materials are lower. Ultimate properties decrease with increasing radiation dose. Each sample is represented by an o. The median is represented by — (n = 3 samples).

3.2 Fatigue Crack Propagation

Fatigue crack propagation resistance of the moderately cross-linked re-melted materials and the highly cross-linked annealed materials was greater than that of highly cross-linked re-melted materials, but was worse than that of untreated controls (Figure 3.3). Statistically, the slopes of all the fatigue resistance lines were the same ($p > 0.10$, 95% confidence interval: 7.3 to 8.4), but the intercepts were not. The fitted intercepts represent the left-to-right shift in the fatigue curve and are related to the inception stress intensity. The intercepts of the 5 Mrad cross-linked re-melted and highly cross-linked annealed materials were not different from one another ($p > 0.20$, 95% CI: 1.02 to 4.07×10^{-6}), but were significantly different from highly cross-linked re-melted materials ($p < 0.001$, 95% CI: 4.10 to 17.9×10^{-6}), and from untreated controls ($p < 0.001$, 95% CI: 0.078 to 0.153×10^{-6}). This means that, in an idealized large laboratory specimen, at a stress intensity range of $1.3 \text{ MPa}\sqrt{\text{m}}$ for 100,000 cycles (roughly one month of service for a joint replacement), a crack in an untreated material would grow about 0.1 mm, a crack in a moderately cross-linked or annealed material would grow about 1 mm, and a crack in highly cross-linked re-melted material would grow about 10 mm.

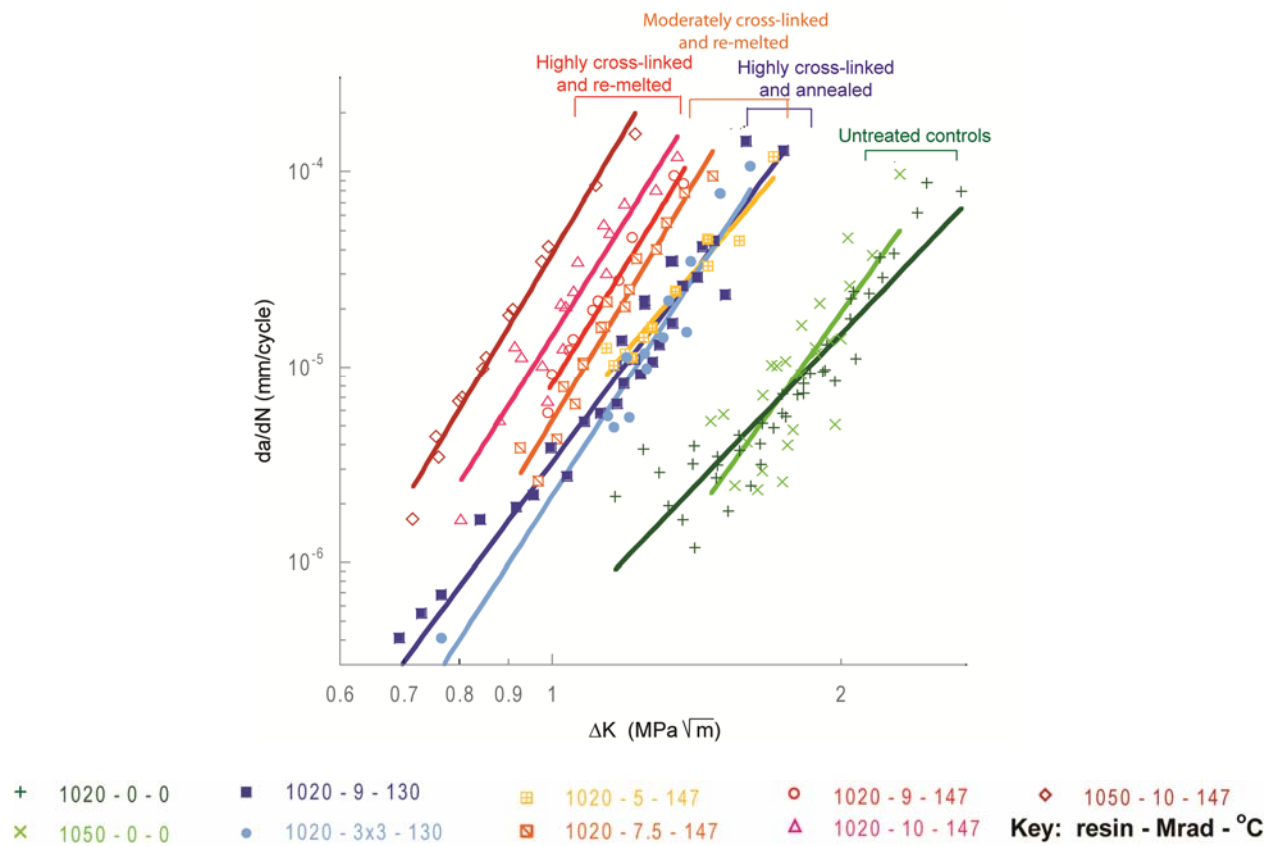


Figure 3.3. Fatigue crack propagation data showing fatigue resistance of moderately cross-linked re-melted and highly cross-linked annealed materials is increased compared to highly cross-linked re-melted materials, but decreased compared to untreated controls. Key: resin – radiation dose (Mrad) – subsequent thermal treatment (°C).

Within the cross-linked re-melted materials, the fatigue resistance decreased with increasing radiation dose (Figure 3.4) (the intercept, C, is significantly different for each cross-linked re-melted group, $p < 0.001$ from an F-test). For example, at a stress intensity range of $1.0 \text{ MPa}\sqrt{\text{m}}$ for 100,000 cycles, a crack in a GUR 1020 7.5 Mrad material would grow about 0.4 mm, while a crack in a GUR 1020 10 Mrad material would grow about 3 mm.

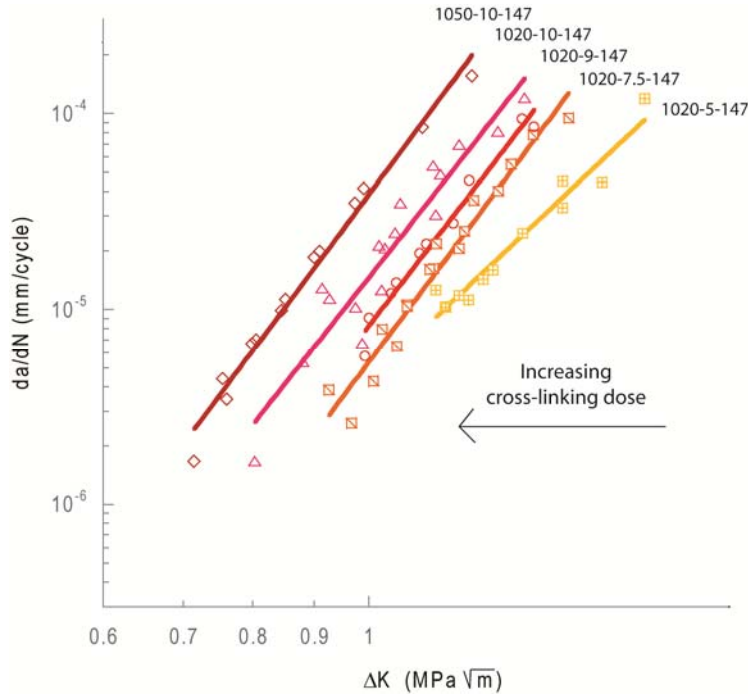


Figure 3.4. Fatigue crack propagation data showing within re-melted materials, fatigue resistance decreased with increasing radiation dose. Key: resin – radiation dose (Mrad) – subsequent thermal treatment ($^{\circ}\text{C}$).

Linear Regression Model

For the linear regression model, functional form assumption checks verified that the data is described by the bilogarithmic relationship assumed by the Paris equation. A series of full versus restricted F-tests resulted in a simplified model (Table 3.1) with the same slope for all groups ($p > 0.10$), one coefficient for the control materials (not different from one another, $p > 0.15$), one coefficient for the 5 Mrad cross-linked re-melted and highly cross-linked annealed materials (not different from one another, $p > 0.20$), and one coefficient for the highly cross-linked re-melted materials plus the 7.5 Mrad re-melted material (statistically different from one another, $p < 0.001$, but pooled for a simplified model). The p-values for the remaining estimated population coefficients were less than 0.001. The R^2 value for the model was 0.8250, indicating that about 83% of the variation in crack growth rate is explained by this simplified model (Table 3.2).

		95% CI on intercept, or C (x 10 ⁻⁶)	95% CI on slope, or m
1050-0-0	cons	0.078 to 0.153	7.258 to 8.350
1020-0-0		0.078 to 0.153	7.258 to 8.350
1020-3x3-130	secgen	1.023 to 4.072	7.258 to 8.350
1020-9-130		1.023 to 4.072	7.258 to 8.350
1020-5-147		1.023 to 4.072	7.258 to 8.350
1020-7.5-147	hxl	4.101 to 17.91	7.258 to 8.350
1020-9-147		4.101 to 17.91	7.258 to 8.350
1020-10-147		4.101 to 17.91	7.258 to 8.350
1050-10-147		4.101 to 17.91	7.258 to 8.350

Table 3.1. Estimated population coefficients on m (slope) and C (intercept) determined from linear regression in combination with full versus restricted F tests. The three groups are all statistically different from one another (p<0.001 from F test).

```
. regr logdadn logdeltak secgen hxl
```

Source	SS	df	MS	Number of obs = 177		
Model	41.1857577	3	13.7285859	F(3, 173) =	271.94	
Residual	8.7338283	173	.050484557	Prob > F =	0.0000	
				R-squared =	0.8250	
				Adj R-squared =	0.8220	
Total	49.919586	176	.283634011	Root MSE =	.22469	

logdadn	Coef.	Std. Err.	t	P> t	[95% Conf. Interval]	
logdeltak	7.80425	.275485	27.23	0.000	7.25819	8.35031
secgen	1.28808	.068796	18.72	0.000	1.15171	1.42445
hxl	2.03167	.140895	23.31	0.000	1.74454	2.31881
_cons	-6.97898	.082692	-84.40	0.000	-7.14289	-6.81508

Table 3.2. Regression analysis from STATA showing the point estimates and 95% confidence intervals for slope m (logdeltaK) and for the intercepts C (cons is for the controls (baseline), secgen and hxl values modify the cons value for the 5 MRad cross-linked and annealed groups, and the highly cross-linked groups, respectively). The values for the intercept must be converted by raising 10 to that power to obtain the values reported for C.

Following the same procedure, a second model was fit including only the re-melted materials to determine if the different levels of cross-linking result in statistically different fatigue performance. The slopes were the same (p>0.20, 95% CI: 7.32 to 8.21) but the intercepts were all statistically different (p<0.001) (Table 3.3). The p-values for the remaining estimated population coefficients were less than 0.001. The R² value for the model was 0.9411, indicating that about 94% of the variation in crack growth rate in cross-linked re-melted materials is explained by this model with different values of C (Table 3.4).

	95% CI on intercept, or C (x 10 ⁻⁶)	95% CI on slope, or m
1020-5-147	2.033 to 3.114	7.322 to 8.218
1020-7.5-147	3.753 to 8.876	7.322 to 8.218
1020-9-147	5.420 to 13.51	7.322 to 8.218
1020-10-147	9.380 to 23.05	7.322 to 8.218
1050-10-147	21.85 to 60.49	7.322 to 8.218

Table 3.3. Estimated population coefficients on m (slope) and C (intercept) determined from linear regression in combination with full versus restricted F tests. The cross-linked re-melted groups are all statistically different from one another (p<0.001 from F test).

```
. regr logdadn logdeltak 102075 10209 102010 105010 if 10205==1 | 102075==1
| 10209==1|102010==1|105010==1
```

Source	SS	df	MS	Number of obs = 68		
Model	13.0339632	5	2.60679265	F(5, 62) =	198.27	
Residual	.81516005	62	.013147743	Prob > F =	0.0000	
				R-squared =	0.9411	
				Adj R-squared =	0.9364	
Total	13.8491233	67	.206703333	Root MSE =	.11466	

logdadn	Coef.	Std. Err.	t	P> t	[95% Conf. Interval]	
logdeltak	7.720493	.2493394	30.96	0.000	7.322071	8.218916
102075	.3605077	.0472271	7.63	0.000	.2661021	.4549134
10209	.5314766	.0529186	10.04	0.000	.4256939	.6372593
102010	.7666593	.0514061	14.91	0.000	.6639001	.8694186
105010	1.1597	.0643572	18.02	0.000	1.031051	1.288348
_cons	-5.59918	.0462719	-121.01	0.000	-5.691676	-5.506684

Table 3.4. Regression analysis from STATA showing the point estimates and 95% confidence intervals for slope m (logdeltaK) and for the intercepts C for the cross-linked re-melted materials (cons is for 1020-5-147 (baseline), other listed values modify the cons value for the specified cross-linked re-melted group). The values for the intercept must be converted by raising 10 to that power to obtain the values for C.

An additional regression analysis was performed on the re-melted materials using resin, radiation dose, and interaction between resin and dose as factors in the model. This analysis evaluates the fundamental effect of resin and radiation dose on the fatigue behavior of the materials rather than determining statistical differences in performance amongst individual materials or groups. The indicator on resin was insignificant and was dropped from the model.

The results are consistent with the other regressions performed (Table 3.5). The R² value is comparable at 0.9377. The slope is the same for all materials and is similar in magnitude, and the values of C calculated for each material fall within the 95% confidence intervals from the other two regressions (Tables 3.1 – 3.4).

```
. regr logdadn logdeltak res1050 dose dosex1050 (1020 resin is baseline)
```

Source	SS	df	MS	Number of obs = 68		
Model	12.9866624	3	4.32888748	F(3, 64)	=	321.23
Residual	.862460853	64	.013475951	Prob > F	=	0.0000
				R-squared	=	0.9377
				Adj R-squared	=	0.9348
Total	13.8491233	67	.206703333	Root MSE	=	.11609

logdadn	Coef.	Std. Err.	t	P> t	[95% Conf. Interval]	
logdeltak	7.683727	.2497481	30.77	0.000	7.184798	8.182656
dose	.1494743	.0098904	15.11	0.000	.129716	.1692327
dosex1050	.0418407	.0043662	9.58	0.000	.0331181	.0505633
_cons	-6.354582	.089067	-71.35	0.000	-6.532514	-6.17665

Table 3.5. Regression analysis from STATA showing that radiation dose is an important factor in predicting the intercept. For each additional 1 Mrad of radiation, the intercept (cons) is increased by 0.149 in 1020 resin materials, and by 0.191 in 1050 resin materials. The values C must be obtained by taking the log of the intercept values.

For a 1020 resin re-melted material the model predicts log da/dn as follows:

$$\log da/dn = \log \Delta K [\text{MPa} \sqrt{\text{m}}] (7.68) + \underbrace{-6.3545 + 0.149 (\text{dose} [\text{Mrad}])}_{\text{intercept (log C)}}$$

↑ slope (m)

For a 1050 resin re-melted material the model predicts log da/dn as follows:

$$\log da/dn = \log \Delta K [\text{MPa} \sqrt{\text{m}}] (7.68) + \underbrace{-6.3545 + 0.191 (\text{dose} [\text{Mrad}])}_{\text{intercept (log C)}}$$

↑ slope (m)

This regression indicates that while all the re-melted materials have the same slope, the radiation dose is a significant factor in predicting the intercept. In addition, there is a significant interaction between radiation dose and resin. This means that in a 1020 resin re-melted material, each additional 1 Mrad of radiation will increase the intercept by 0.149 log mm/cycle, or will increase the crack growth rate by 41%. In contrast, in a 1050 resin re-melted material, each additional 1 Mrad of radiation will increase the intercept by 0.191 log mm/cycle, or will increase the crack growth rate by 55%. In both resins the crack growth rate increases with increasing dose, but in the 1050 resin the crack growth rate is more sensitive to changes in radiation dose.

3.3 Wear Rate

All the cross-linked ultra-high groups had significantly lower wear rates than untreated control materials (Table 3.6). All materials reached a steady-state wear rate after approximately 300,000 cycles (Figure 3.5). The moderately cross-linked re-melted 5 Mrad material had a significantly higher wear rate than materials with higher radiation doses. There was no significant difference in wear rate for 9 Mrad materials subjected to re-melting versus annealing. However, the sequentially-dosed ultra-high demonstrated the lowest wear rate of all the materials – significantly lower than the single dose 9 Mrad annealed material (Figure 3.5). The GUR 1050 and GUR 1020 materials were not statistically different; nor were any the highly cross-linked re-melted materials.

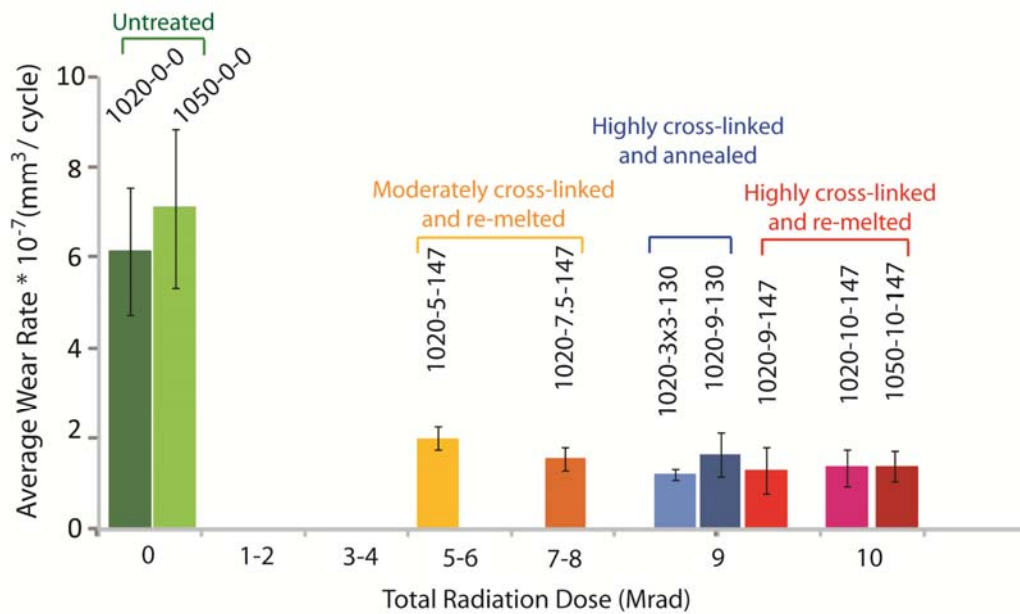
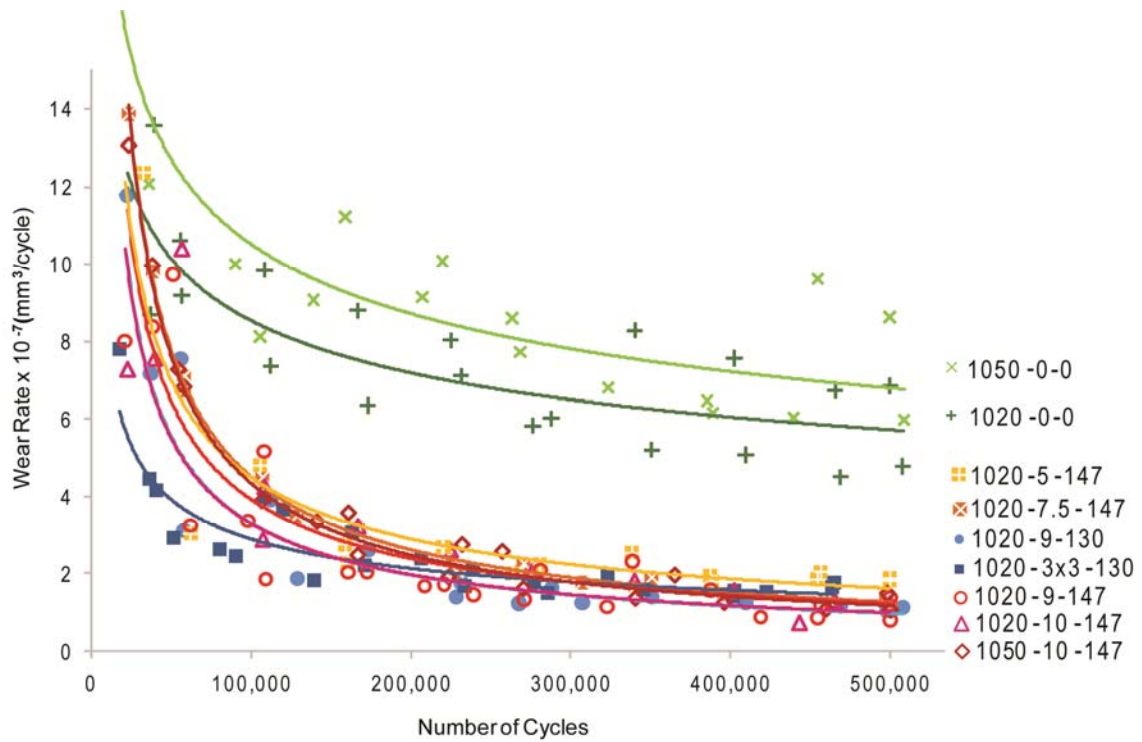


Figure 3.5. Wear data showing (top) wear rates were significantly lower for all cross-linked ultra-high compared to untreated (n=2 tests) and (bottom) steady-state wear rate depends primarily on radiation dose (beyond 300,000 cycles, n = 6-8 wear rate measurements). Key: resin – radiation dose (Mrad)– subsequent thermal treatment (°C).

Analysis of Variance and Student-Newman-Keuls Multiple Comparisons

Analysis of variance on the steady-state wear rates of the nine material groups resulted in a p-value of $p < 0.0001$ indicating statistically significant differences in wear rates amongst the material groups. The Student-Newman-Keuls multiple comparisons procedure then determined which wear rates were significantly different from one another (Table 3.6). The standard deviation of the wear rates and the number of observations were not the same across all material groups (Table 3.7). However, by explicitly calculating the Student-Newman-Keuls q-statistic for each comparison of interest (33 comparisons total), the different standard deviations and numbers of observations were taken into account (Table 3.8) (Glantz, 2005).

Significant Comparison	p-value	Not Significant comparison	p-value
1020-0-0 vs all cross-linked	<0.0001	1020-0-0 vs 1050-0-0	0.1005
1050-0-0 vs all cross-linked	<0.0001	1020-10-147 vs 1050-10-147	0.3883
1020-5-147 vs 1020-7.5-147	0.0023	1020-9-130 vs 1020-9-147	0.0737
1020-5-147 vs 1020-3x3-130	0.0006		
1020-5-147 vs 1020-9-130	0.0010	All other comparisons	
1020-5-147 vs 1020-9-147	0.0133	between cross-linked	>0.05
1020-5-147 vs 1020-10-147	0.0358	materials	
1020-5-147 vs 1050-10-147	<0.0001		
1020-3x3-130 vs 1020-9-130	0.0018		
1020-3x3-130 vs 1020-7.5-130	0.0003		

The p-value from the initial analysis of variance F-test is < 0.0001 . Post-hoc multiple comparisons were performed using the Student-Newman-Keuls test, with one-way p-values reported above.

Table 3.6. Summary of statistical comparisons between wear rates show that all cross-linked materials had significantly lower wear rates than the untreated control materials, while the 5 Mrad re-melted material had a significantly higher wear rate than materials with higher radiation doses.

Material Group	Mean	Standard Deviation	Number of Observations
1020-3x3-130	1.20E-07	1.21E-08	6
1020-9-147	1.27E-07	5.02E-08	8
1020-10-147	1.34E-07	4.05E-08	6
1050-10-147	1.36E-07	3.33E-08	6
1020-7.5-147	1.53E-07	2.52E-08	7
1020-9-130	1.63E-07	1.79E-08	7
1020-5-147	1.98E-07	2.55E-08	7
1020-0-0	6.12E-07	1.41E-07	8
1050-0-0	7.10E-07	1.43E-07	7

Table 3.7. Mean and standard deviation of steady-state wear rates. The standard deviation and number of observations differs amongst the material groups, which is taken into account using the Student-Newman-Keuls multiple comparison procedure.

Comparisons		q-statistic	Cutoff	Significant?
1050-0-0 vs	1020-3x3-130	36.054483	4.5925	S
	1020-9-147	18.802347	4.4805	S
	1020-10-147	18.280386	4.3495	S
	1050-10-147	21.144125	4.1975	S
	1020-7.5-147	24.549120	4.0080	S
	1020-9-130	28.604991	3.7640	S
	1020-5-147	22.432665	3.4205	S
	1020 -0-0	1.8858706	2.8435	NS
1020-0-0 vs	1020-3x3-130	31.191371	4.4805	S
	1020-9-147	16.305169	4.3495	S
	1020-10-147	15.691489	4.1975	S
	1050--10-147	18.190594	4.0080	S
	1020-7.5-147	21.040993	3.7640	S
	1020-9-130	24.421574	3.4205	S
	1020-5-147	18.866184	2.8435	S
	1020-5-147 vs	1020-3x3-130	11.287553	4.3495
1020-9-147		5.4225028	4.1975	S
1020-10-147		4.8099523	4.0080	S
1050-10-147		5.4083831	3.7640	S
1020-7.5-147		4.6966822	3.4205	S
1020-9-130		4.3343149	2.8435	S
1020-9-130 vs		1020-3x3-120	7.4270649	4.1975
	1020-9-147	3.2816141	4.0080	NS
	1020-10-147	2.6013714	3.7640	NS
	1050-10-147	2.8111440	3.4205	NS
	1020-7.5-147	1.2457252	2.8435	NS
	1020-7.5-147 vs	1020-3x3-130	4.8038446	4.0080
1020-9-147		1.9974899	3.7640	NS
1020-10-147		1.4364292	3.4205	NS
1050-10-147		1.4917447	2.8435	NS
1050-10-147 vs		1020-3x3-130	1.9524540	3.7640
	1020-9-147	0.5764214	3.4205	NS
	1020-10-147	0.1271920	2.8435	NS

S = significant, NS = not significant

Table 3.8. For each pairwise comparison of interest, Student-Newman-Keuls q-statistic was calculated, arranged in decreasing order, and compared to decreasing tabulated values to determine statistical significance (Glantz, 2005).

Wear Rate Measurement Accuracy and Effect of Creep

The accuracy of the wear rate measurement was $\pm 6\%$ based on the largest and smallest circles that could be fit to the image of the wear scar. The group with the lowest variation in measurement was the 1050-0-0 untreated control (2.2%), while the group with the highest variation was the highly cross-linked and re-melted material 1020-10-147 (10.4%). The rest of the material groups had variation from 3.5 to 8.0%, with no dependence on material treatment.

The effect of creep on the wear measurement was more substantial. Allowing the material to recover and simply re-measuring the wear scar assuming it is still flat resulted in about a 14% overestimation of the wear volume using the original measurement. Also taking the recovered bulge into account resulted in an additional 62% overestimation. The exact measurement of the machined pin radius resulted in less than 1% difference in the total wear volume. The trends demonstrated by the materials investigated were the same when using the flat wear scar assumption, but were slightly altered taking the bulge into account (Figure 3.6). However, the accuracy of the measurement on the bulge volume method was about $\pm 17\%$, which is larger than the differences amongst three of the four groups.

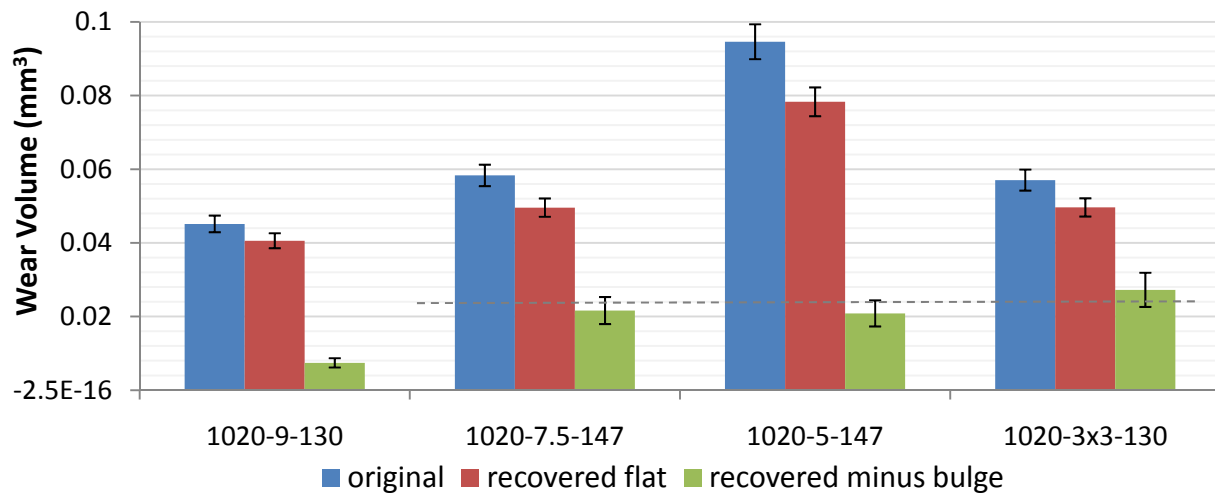


Figure 3.6. Wear volume measurements considering creep recovery show an overestimation of the wear by 14% when assuming a flat wear scar and by 62% when taking the recovered bulge into account. The error bars represent $\pm 6\%$ accuracy on the original and recovered flat, and $\pm 17\%$ accuracy on the bulge measurement. Given these accuracies, the trends are consistent ($n=3$ measurements on 1 wear scar for each of 4 material groups).

3.4 Oxidation

Oxidative stability was achieved by re-melted materials but not by annealed materials (Figure 3.7). The cross-linked re-melted materials were chemically stable after artificial aging (oxidation index less than 0.1), along with the untreated materials. The cross-linked annealed materials were susceptible to oxidation with an oxidation index greater than 0.5 after artificial aging. As expected, crystallinity increased by about 10-15% in the oxidized materials (Table 3.9).

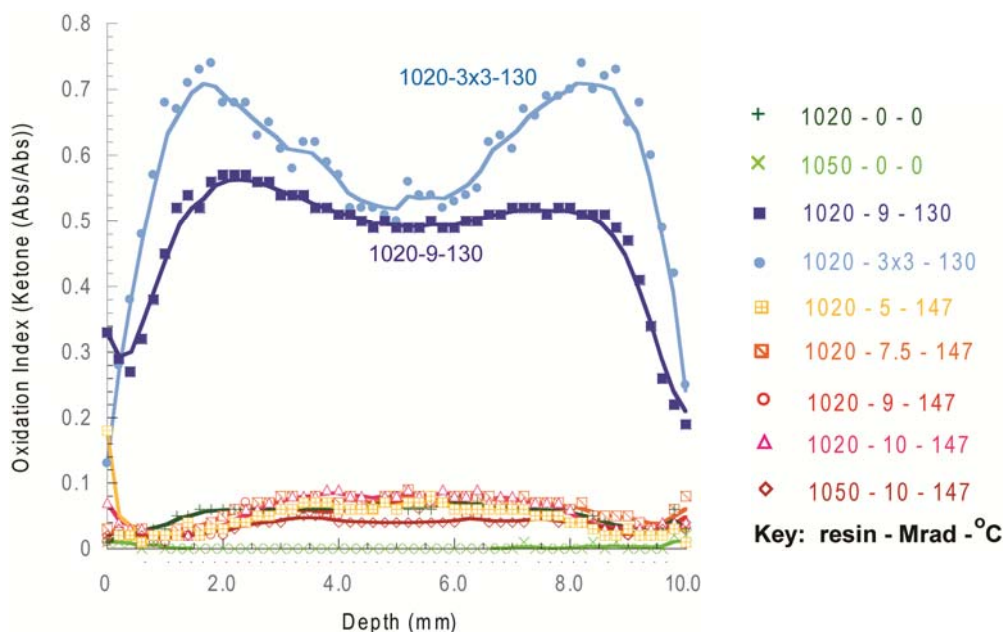


Figure 3.7. Artificial aging data showing that annealed materials have an oxidation index greater than 0.5 while re-melted and untreated materials remain chemically unchanged with an oxidation index less than 0.1. Aging was performed in 3 atm O₂ at 63°C for 28 days (Currier, Currier, Mayor, Lyford, Van Citters et al., 2007). Oxidation index is defined as the measured 1715 cm⁻¹ peak height (ketone) normalized to the 1368 cm⁻¹ peak height.

	Crystallinity	Stdev
1020-3x3-130	59.2	3.0
1020-3x3-130 Aged	67.8	5.1
1020-9-130	58.6	1.5
1020-9-130 Aged	65.3	2.3

n = 6 samples tested

Table 3.9. Crystallinity increased after aging in the oxidized materials.

3.5 Microstructure

Microstructural parameters such as lamellar size and percent crystallinity also depended on the heat treatment, the radiation dose, and the resin. Annealing produced large lamellae similar in size to those of the untreated controls with respect to the magnitude and distribution of lamellar thickness, length, and cross-sectional area. Annealed materials showed increased percent crystallinity by 10% compared to the untreated controls. Alternately, re-melted materials demonstrated lamellae smaller than those of the untreated controls (Figure 3.8) with decreased percent crystallinity by about 5%. Furthermore, in the re-melted materials, the percent crystallinity decreased with increasing radiation dose. With respect to resin, the GUR 1020 materials had slightly smaller lamellae but higher crystallinity than the GUR 1050 materials with the same heat treatment and radiation dose (Figure 3.9).

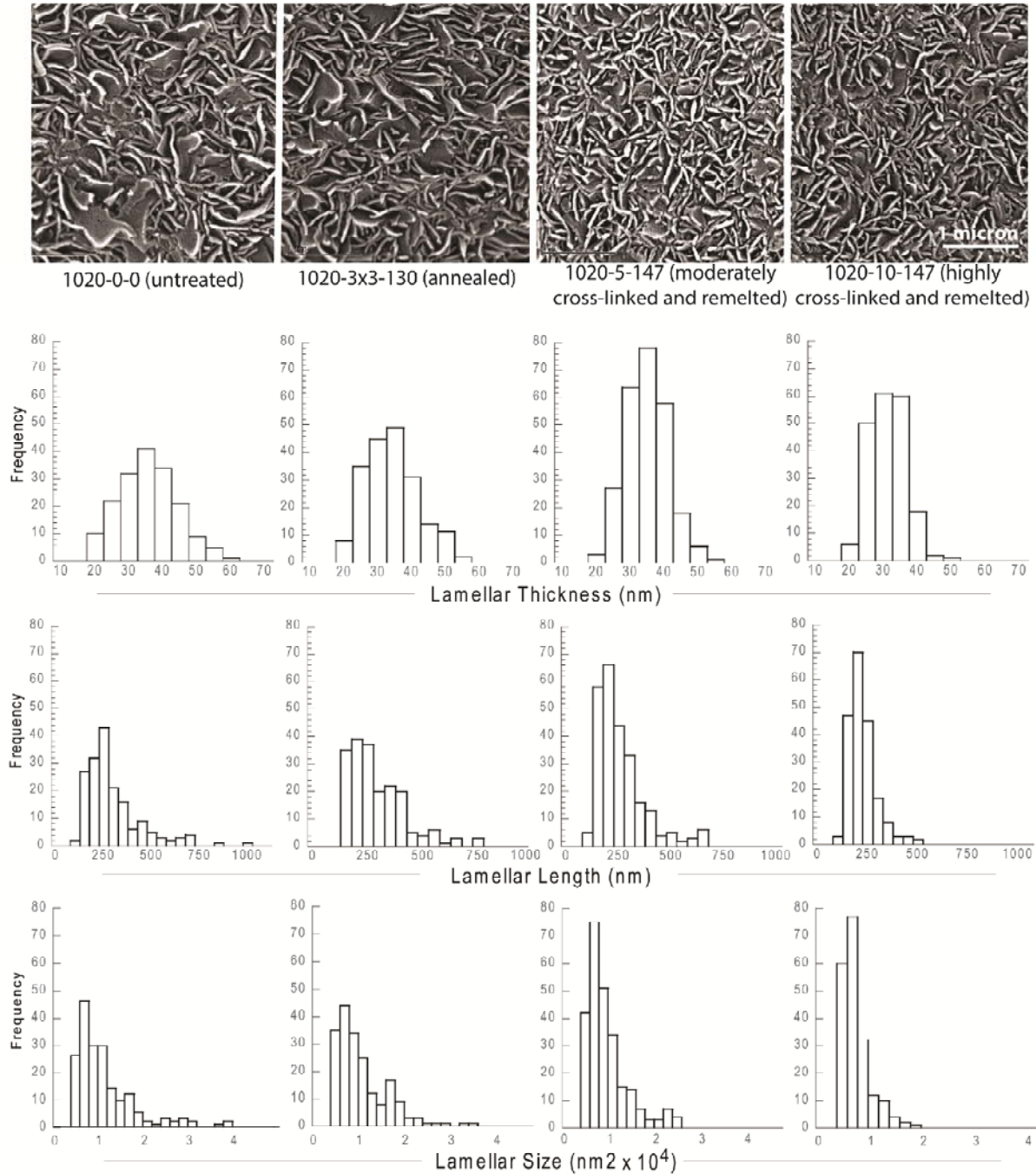


Figure 3.8. Microstructural characterization of four representative material groups: a) untreated control, b) highly cross-linked annealed material, c) moderately cross-linked re-melted material, d) highly cross-linked re-melted material. Note the lamellar structure of the annealed material is similar to that of the untreated control, while that of the re-melted materials is generally smaller. Scanning electron micrographs were obtained after amorphous regions were removed by etching. Scale bar in the lower right corner represents 1 micron for all images. Histograms of the lamellar microstructural properties are shown for each group.

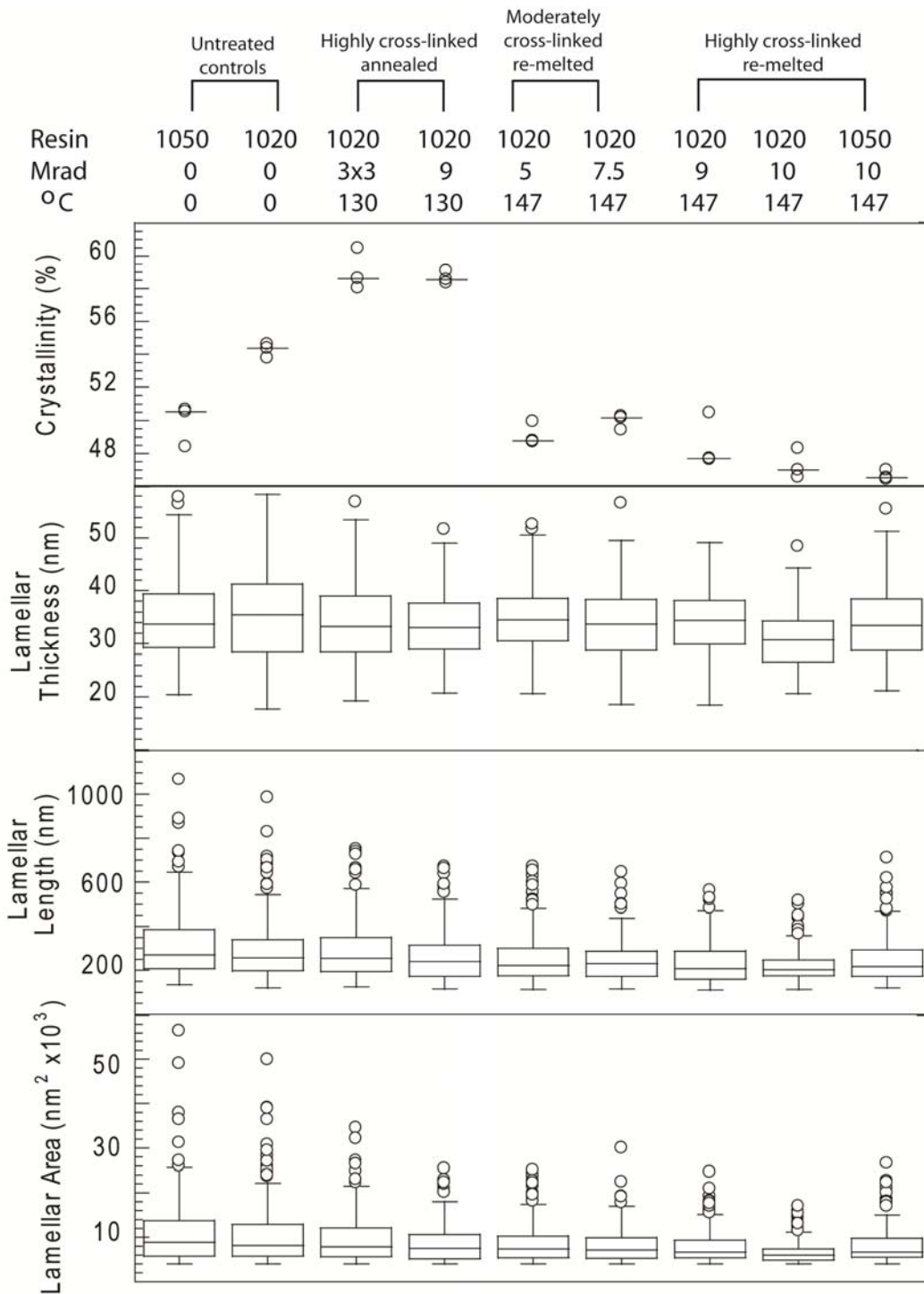


Figure 3.9. Microstructural properties for all material groups. Crystallinity is higher for annealed materials and lower for re-melted materials compared to untreated controls. Lamellar thickness, length, and size show a trend of smaller median lamellae with narrower distributions in re-melted materials. For crystallinity each sample is represented by an O with the median represented by — ($n = 3$ samples). For lamellar properties the box represents the middle two quartiles separated by a median line. The whiskers represent the upper and lower quartiles and outliers are represented by O (from image analysis performed on one representative scanning electron micrograph per material).

Comparison to Other Techniques

The lamellar thickness measured by the image analysis technique developed in this dissertation (MPG) was very similar to the lamellar thickness measured by the established differential scanning calorimetry technique (DSC) for the untreated control materials (Table 3.10). This method is only valid for uncross-linked ultra-high.

With respect to the thermodynamic-based image analysis technique developed by Van Citters (D. W. Van Citters, 2006), the MPG lamellar area measurement correlated well with the Van Citters (DVC) calculation of lamellar area ($R^2=0.82$) (Figure 3.12). Lamellar thickness and length (or equivalent diameter) did not correlate well ($R^2=0.46$ and $R^2=0.52$, respectively) (Figures 3.10 and 3.11). In general, the Van Citters thickness was larger in magnitude with a larger range than the MPG measure, while the Van Citters length was smaller in magnitude with a smaller range. The MPG thickness measure was considerably more similar to the established differential scanning calorimetry technique (DSC) for the untreated control materials (Figure 3.10).

When applied to images of materials from another study that had also undergone x-ray scattering (Simis et al., 2006), the MPG thickness measurement was moderately correlated to the thickness measured by x-ray scattering ($R^2=0.58$) with only four material groups (Figure 3.13). The thickness measurement on one material was substantially different (131 nm versus 62 nm) (Table 3.11).

	1020	1050	1020	1020	1020	1020	1020	1020	1050
	0	0	3x3	9	5	7.5	9	10	10
	0	0	130	130	147	147	147	147	147
<i>n images</i>	2	1	2	5	2	2	1	1	3
Thickness (nm)									
MPG	35.52	34.60	33.78	33.53	33.41	34.48	34.11	30.91	33.31
DVC	67.28	90.48	48.90	27.40	65.90	49.34	34.54	14.72	53.16
DSC	34.80*	40.00*	--	--	--	--	--	--	--
Length (nm)									
MPG	279.24	320.06	281.23	257.88	260.34	246.43	237.10	219.97	247.87
DVC	225.47	229.58	232.33	230.48	217.67	197.09	202.56	205.25	194.70
Area (nm²)									
MPG	9919.4	11075.0	9500.9	8647.4	8697.8	8497.1	8086.5	6799.8	8257.5
DVC	15169.0	20772.4	11361.1	6314.8	14343.6	9724.3	6996.5	3021.2	10351.2

* Differential scanning calorimetry performed on n = 3 samples.

Table 3.10. Summary of lamellar parameter estimates using three measurement techniques.

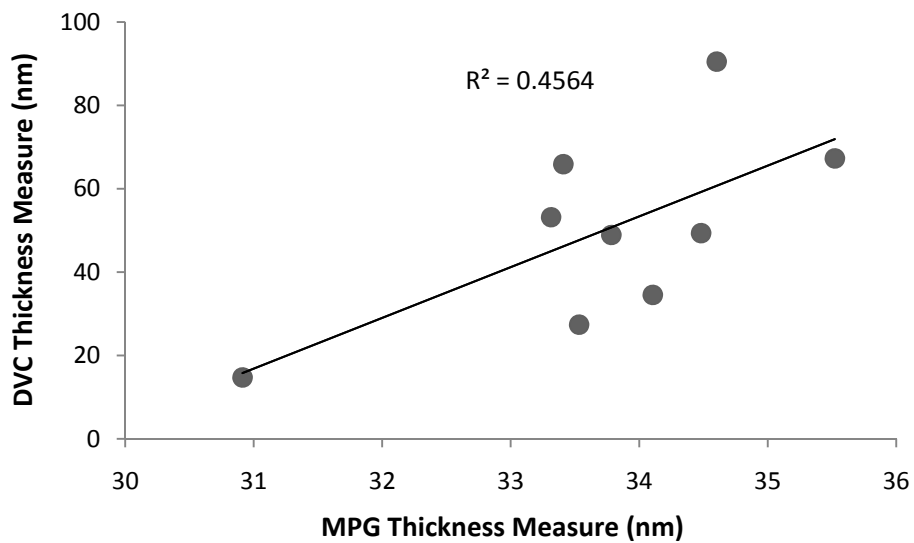
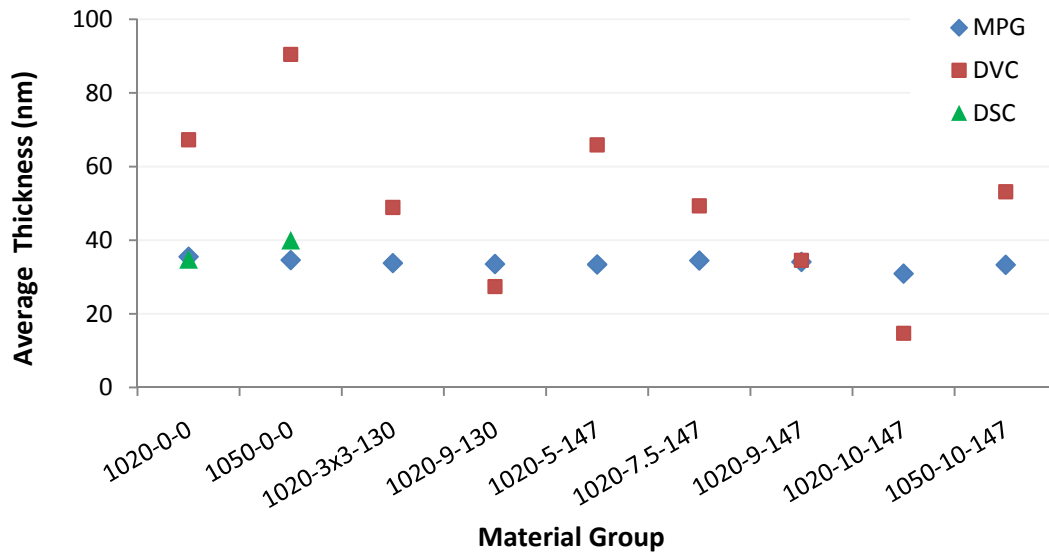


Figure 3.10. Comparison of average lamellar thickness measurements shows that the MPG measure is generally smaller with a smaller range than the Van Citters (DVC) method, but is much closer to the established differential scanning calorimetry (DSC) technique for uncross-linked materials. The MPG thickness measure was not well-correlated with the Van Citters thickness measure.

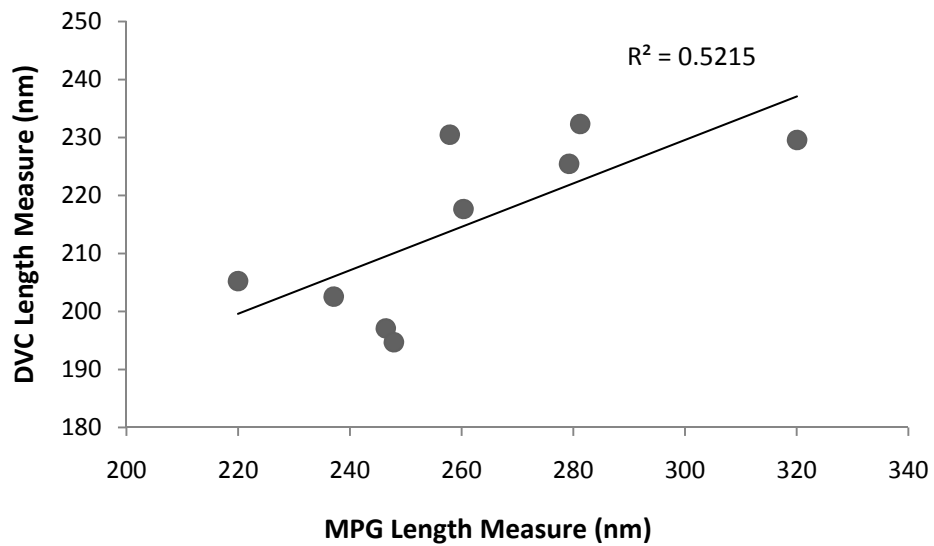
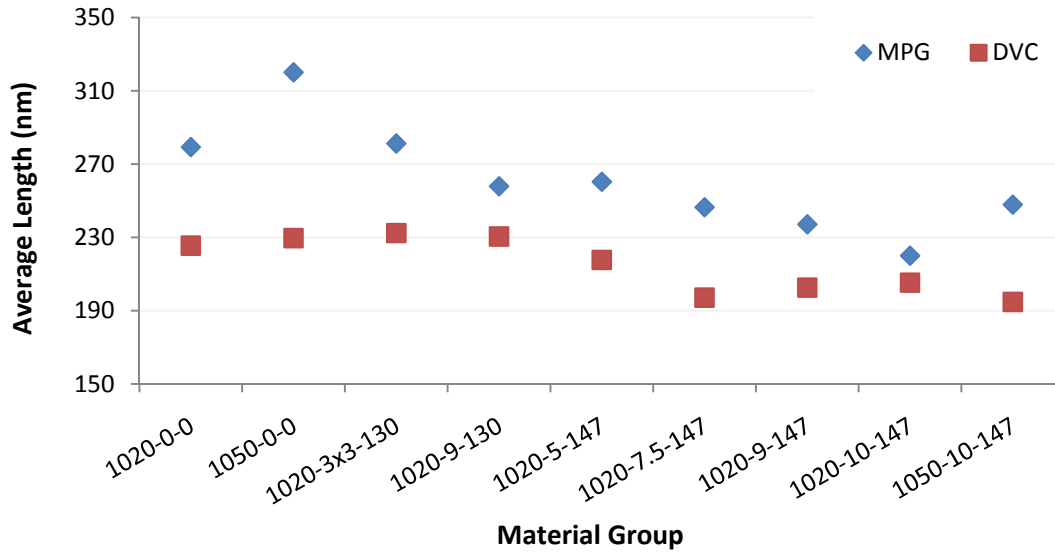


Figure 3.11. Comparison of average lamellar length (diameter) measurements shows that the MPG measure is generally larger with a larger range than the Van Citters (DVC) method. The MPG length (diameter) measure was not well-correlated with the Van Citters measure.

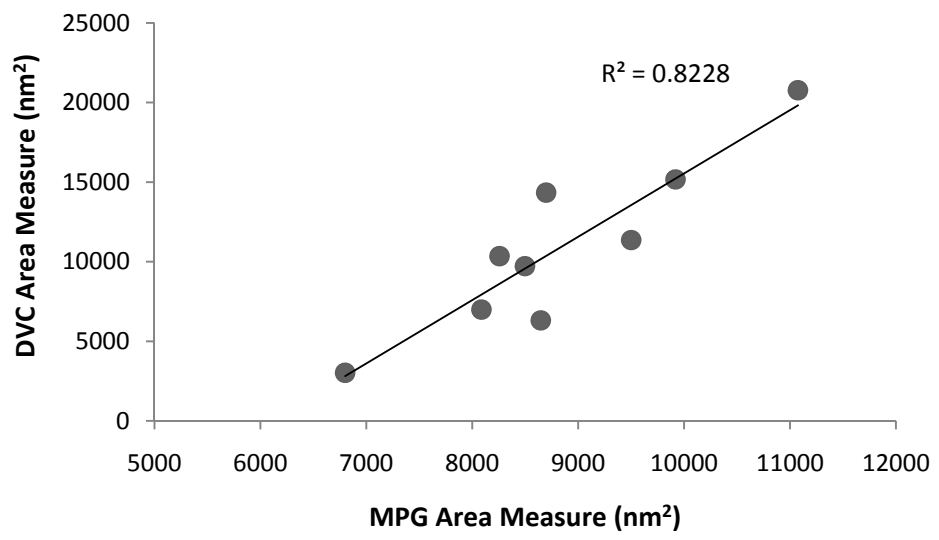
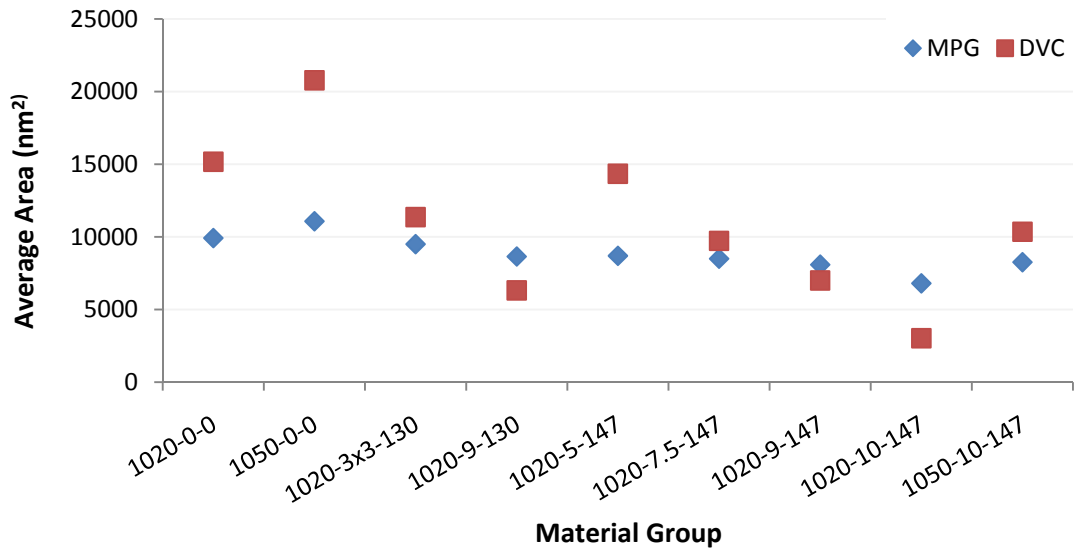


Figure 3.12. Comparison of average lamellar size (area) measurements shows that the MPG measure is generally consistent with the Van Citters (DVC) method. The MPG size (area) measure was well-correlated with the Van Citters size (area) measure.

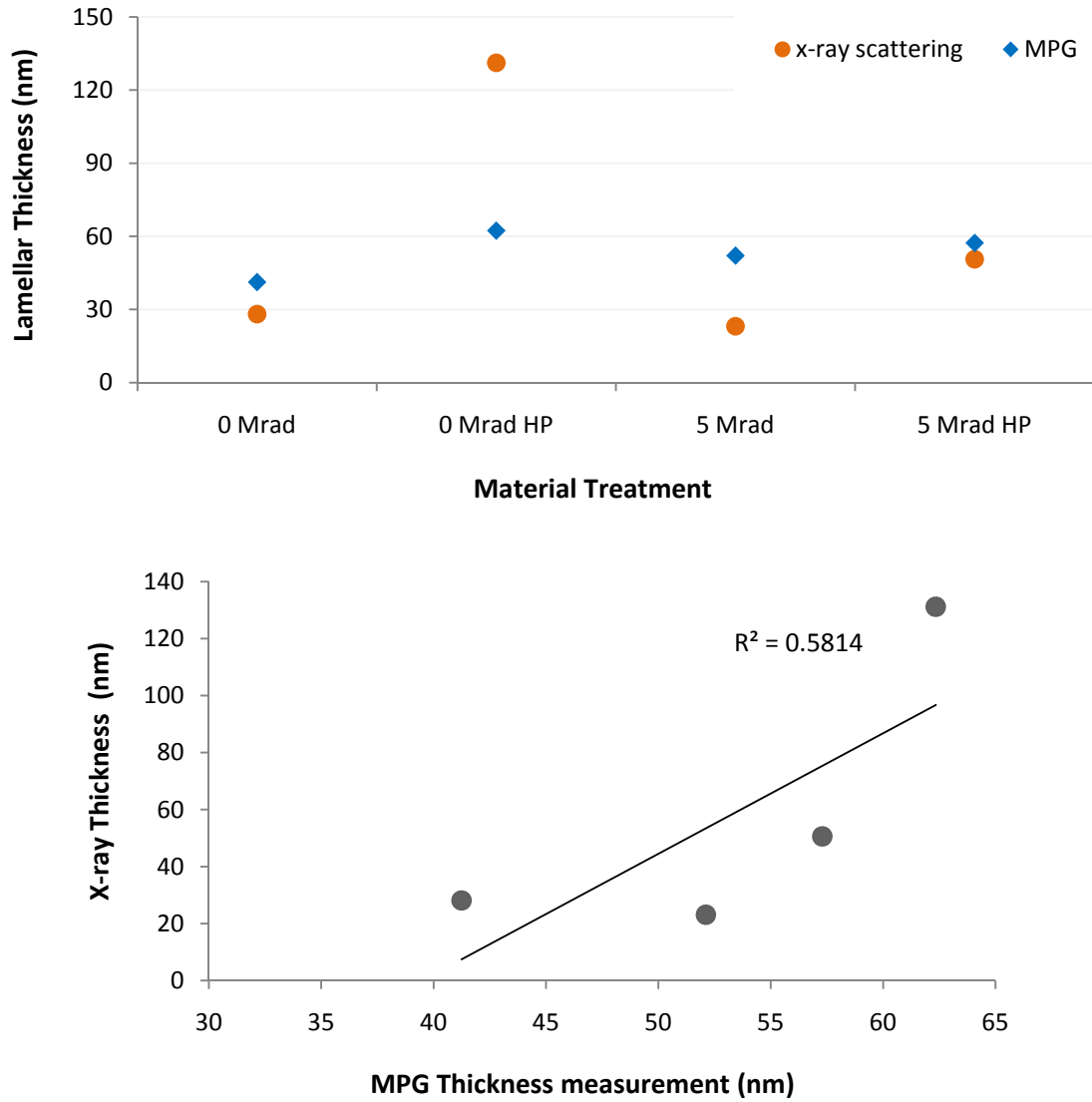


Figure 3.13. Comparison of average lamellar thickness measurements on materials from another study (Simis et al., 2006) shows that the MPG measure is generally consistent with the x-ray scattering method. The MPG thickness measure was moderately well-correlated with x-ray scattering measure, with only four material groups.

Thickness	0 Mrad	0 Mrad HP	5 Mrad	5 Mrad HP
X-ray scattering (nm)	28.1	131.2	23.1	50.6
MPG (nm)	41.2	62.3	52.1	57.3

MPG based on n = 1 image, x-ray scattering based on n = 3 diffraction scans.

Table 3.11. Summary of lamellar thickness measurements on materials from another study (Simis et al., 2006) using the MPG image analysis technique and the x-ray scattering technique.

3.6 Statistical Correlations

Non-parametric statistical analysis showed that the elastic modulus and yield strength were highly-correlated with crystallinity, while ultimate true stress and strain were highly-correlated with lamellar area (Tables 3.12 and 3.13). Resistance to fatigue crack propagation was correlated with both crystallinity and with lamellar are and length. Wear rate was not significantly correlated with any of the microstructural parameters. Lamellar thickness was not correlated with any mechanical properties, likely due to the small range and wide distributions of the lamellar thickness measurements.

Microstructural Property	Resistance to fatigue	Yield stress	Elastic modulus	Ultimate true strength	Ultimate true strain	Wear rate
	ρ	ρ	ρ	ρ	ρ	ρ
Crystallinity	0.85 ^a	0.93 ^b	0.98 ^b	0.60	0.53	0.18
Lamellar thickness	0.71	0.23	0.33	0.70	0.85	0.48
Lamellar length	0.85 ^a	0.55	0.72	0.72	0.73	0.48
Lamellar area	0.93 ^b	0.62	0.77	0.85 ^a	0.85 ^a	0.61

^a $p < 0.01$

^b $p < 0.001$

Table 3.12. Spearman rank correlation coefficients for microstructural properties and mechanical performance measures. Note the elastic properties are correlated with percent crystallinity, the ultimate properties with lamellar size, resistance to fatigue with both, and wear rate with none.

	fcp	yield	modulus	uts	ustrain	wear	cryst	thick75	length75	area75
fcp	1.0000									
yield	0.7167 0.0298	1.0000								
modulus	0.8333* 0.0053	0.9500* 0.0001	1.0000							
uts	0.8667* 0.0025	0.5667 0.1116	0.6333 0.0671	1.0000						
ustrain	0.8167* 0.0072	0.4667 0.2054	0.5167 0.1544	0.9333* 0.0002	1.0000					
wear	0.5500 0.1250	0.1667 0.6682	0.2667 0.4879	0.8333* 0.0053	0.7667 0.0159	1.0000				
cryst	0.8500* 0.0037	0.9333* 0.0002	0.9833* 0.0000	0.6000 0.0876	0.5333 0.1392	0.1833 0.6368	1.0000			
thick75	0.7167 0.0298	0.2333 0.5457	0.3333 0.3807	0.7000 0.0358	0.8500 0.0372	0.4833 0.1875	0.4167 0.2646	1.0000		
length75	0.8500* 0.0037	0.5500 0.1250	0.7167 0.0298	0.7167 0.0298	0.7333 0.0246	0.4833 0.1875	0.7500 0.0199	0.7833 0.0125	1.0000	
area75	0.9333* 0.0002	0.6167 0.0769	0.7667 0.0159	0.8500* 0.0037	0.8500* 0.0037	0.6167 0.0769	0.7833 0.0125	0.8000* 0.0096	0.9667* 0.0000	1.0000

Table 3.13. Detailed results from STATA Spearman rank correlation for microstructural properties and mechanical performance measures.

Chapter 4

Discussion and Conclusions

4.1 Trade-offs in Material Behavior

There is a trade-off amongst fatigue crack propagation resistance, wear resistance, and oxidative stability in clinically-relevant cross-linked ultra-high (Figure 4.1). High cross-linking combined with re-melting produces good wear resistance and oxidative stability but relatively poor resistance to fatigue crack propagation. High cross-linking combined with annealing produces good resistance to wear and fatigue crack propagation but can leave the material susceptible to oxidation. Moderate cross-linking combined with re-melting produces good oxidative stability but moderate resistance to fatigue crack propagation and wear.

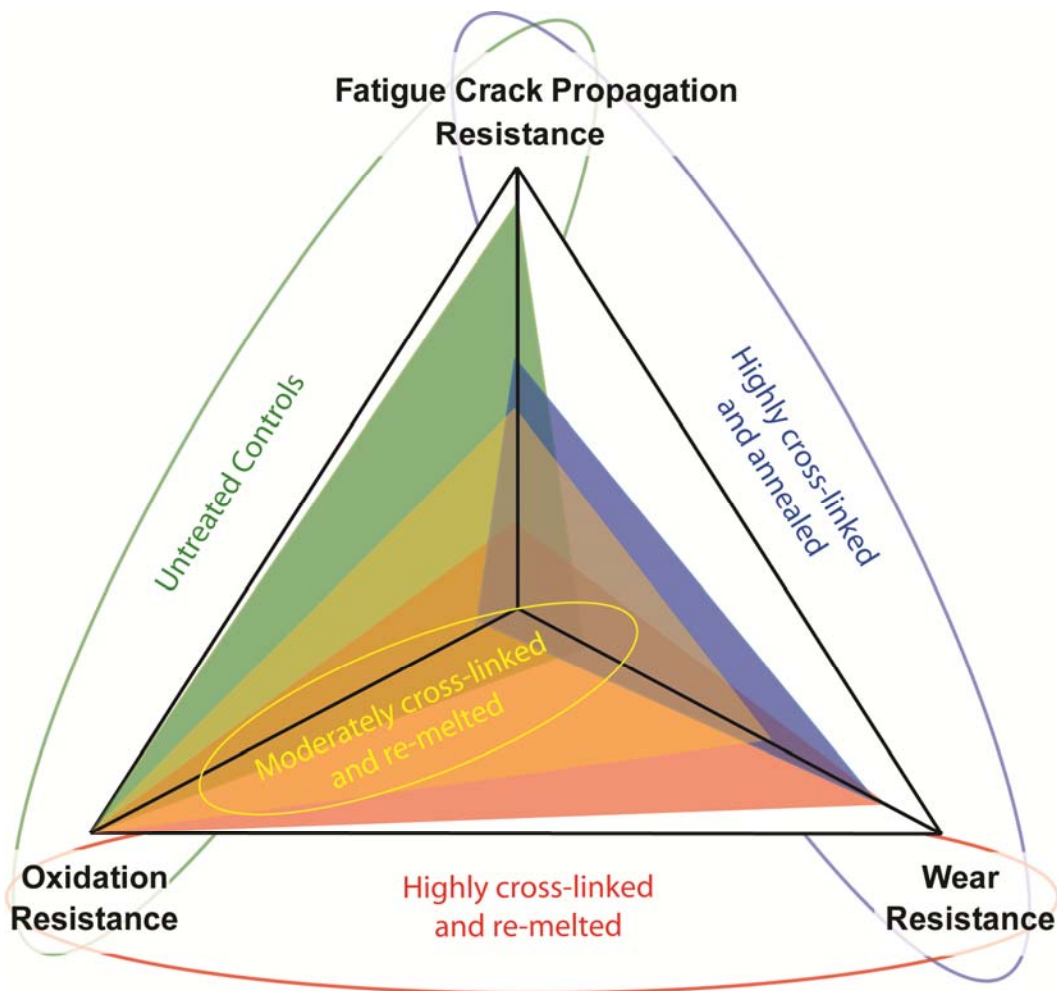


Figure 4.1. Schematic showing the trade-offs in fatigue crack propagation resistance, wear resistance, and oxidation resistance. The vertices of the colored triangles on each axis represent the relative performance in that category.

4.2 Material Behavior and Processing Treatments

Material behavior was dependent on both total radiation dose and heat treatment. Increasing radiation dose decreased fatigue resistance and ultimate properties, but increased wear resistance. Annealing, as opposed to re-melting, reduced fatigue resistance and elastic properties less than re-melting, but left materials susceptible to oxidation.

Within the highly cross-linked annealed materials, sequential doses of radiation and annealing did not significantly change resistance to fatigue or oxidation beyond that of an equivalent total single dose. However, sequential doses of radiation and annealing did appear to improve the wear resistance compared to the equivalent single dose. It is well known that increased thermal energy increases cross-link density (Muratoglu et al., 1999), and that increased cross-link density increases multidirectional sliding wear resistance (Muratoglu et al., 1999; Wang, 2001). The sequential dose annealed material is subjected to more thermal energy during processing, which would affect both cross-link density and wear behavior.

Resin and consolidation method also affected material behavior. The two GUR 1020 materials had higher crystallinity, yield strength, modulus, and fatigue crack propagation resistance than GUR 1050 materials with the same heat treatment and radiation dose. No statistical difference was found in the wear behavior of GUR 1020 versus GUR 1050 materials. The differences in elastic and fatigue behavior may be due to the lower molecular weight of the GUR 1020 (2-4 million grams/mol) compared to GUR 1050 (3-6 million grams/mol). With a lower molecular weight, the long-chain molecules are more mobile and may be more easily incorporated into lamellae. This results in higher percent crystallinity, which is correlated with higher yield strength, modulus and fatigue resistance. The differences in resin are also confounded by differences in consolidation method, which has been shown to impart directionality and to affect fatigue crack propagation resistance and tensile properties (L. Pruitt & Bailey, 1998). This directionality explains the lower fatigue crack propagation resistance of the highly cross-linked GUR 1050 material, which was tested in the weak orientation in which crack propagation direction is aligned with the ram extrusion direction.

4.3 Effect of Microstructure

The effects of the processing treatments on the material behavior can be elucidated by examining the microstructure. Cross-linking the ultra-high forms covalent bonds between the long-chain molecules; this results in a networked structure in the amorphous phase. Irradiation for cross-linking also produces residual free radicals, which can lead to in vivo oxidative degradation if the free radicals are not eliminated by heat treatment (Collier et al., 2003; Currier, Currier, Mayor, Lyford, Van Citters et al., 2007). These results show that applying thermal energy below the melting temperature after cross-linking (annealing) increased the volume fraction of lamellae, likely due to a combination of chain scission from radiation and increased mobility of amorphous chains from annealing (Viano et al., 2007). However, this annealing process failed to neutralize all free radicals. Alternatively, re-melting the materials appeared to eliminate free radicals, but, restricted by the network of cross-links, the re-formed lamellae were fewer and smaller in size. The fewer, smaller lamellae coupled with the networked amorphous phase were associated with decreased fatigue resistance and tensile properties.

The statistical relationships between fatigue resistance, tensile properties, and lamellar properties also add to an understanding of micromechanisms of damage in ultra-high. The non-parametric statistical analysis suggests that elastic parameters are strongly correlated with percent crystallinity while ultimate parameters are strongly correlated with lamellar size, in agreement with the literature (Medel, Pena, Cegonino, Gomez-Barrena, & Puertolas, 2007; Ries & Pruitt, 2005; Simis et al., 2006). Resistance to fatigue crack propagation is correlated with both percent crystallinity and lamellar size. By extension then, superior fatigue crack propagation resistance is associated with both high elastic and high ultimate properties. A high elastic modulus and high yield stress may contribute to limiting the strains at the crack tip while dissipating more energy before yielding. Higher ultimate true stresses and strains may contribute to more energy dissipation before ultimately failing on the microscale at the crack tip. Resistance to fatigue crack propagation was also highly-correlated with a large lamellar cross-sectional area and with percent crystallinity, suggesting that more lamellae, large in both dimensions, may require more energy for cracks to travel through or around.

Wear rate was not significantly correlated to any of the microstructural parameters in this study and was dominated by radiation dose. In a similar study on the relationship of microstructural parameters to rolling-sliding wear rate, Van Citters et al (Douglas W. Van Citters, Kennedy, & Collier, 2007) found a correlation between wear rate and lamellar size normalized by yield strength. The data in this dissertation did not exhibit the same trend. However, the Van Citters study is based on delamination wear which is ultimately a crack nucleation and propagation mechanism. The results are consistent in demonstrating a correlation between fatigue processes and lamellar size. The primary wear mechanism in this dissertation was multidirectional sliding wear. It has long been thought that multidirectional sliding wear is due to the alignment of lamellae in the sliding direction, resulting in a weakened material under cross-shear (Edidin et al., 1999; Wang, 2001). Cross-linking has been shown to inhibit the ability of the lamellae to align (Klapperich et al., 1999; Zhou & Komvopoulos, 2005), which is in agreement with the observation that sliding wear rate decreased with increased radiation dose. These results suggest that the number, size, and thickness of the lamellae are not as important for inhibiting sliding wear as is cross-linking the amorphous phase.

4.4 Limitations

Experimental Characterization

With respect to the experimental data, one major limitation is the fact that despite the large number of material groups, the volume of material in each group was restricted, which resulted in a small number of samples for the tensile and microstructure data. However, the data based on three samples resulted in relatively small scatter and large differences amongst groups for yield strength, ultimate properties, and crystallinity. In addition, the limited volume of material did not affect the number of samples used to obtain the fatigue, wear, or oxidation data, which was the primary focus of the study.

Another limitation due to the small volume of material is that a parallel set of fatigue, wear, and tensile tests could not be performed on aged specimens. However, the degradation of

mechanical properties due to oxidation of ultra-high has been established in the literature (Baker et al., 2000; Collier, Sperling et al., 1996; Costa et al., 2006; Costa et al., 1998a; Currier et al., 1997; Currier, Currier, Mayor, Lyford, Van Citters et al., 2007). Specifically, Baker et al. (Baker et al., 2000) found that polyethylene highly oxidized by artificial aging demonstrated decreased ultimate properties and decreased resistance to fatigue crack propagation, shifting fatigue crack propagation curves (such as those in this study) to the left. This suggests that while annealed materials had better initial fatigue resistance, they may worsen over time, shifting the fatigue crack propagation curves left towards those of highly cross-linked and re-melted materials.

Finally, the wear measurement technique had not been fully established in this laboratory prior to this study. However, the technique is well-established in the literature (Burriss & Sawyer, 2009; Saikko, 2006; Zhou & Komvopoulos, 2005). Additional investigations were performed on the accuracy of the wear measurement and the effect of creep. The accuracy of the wear rate measurement using the image analysis protocol was found to be about $\pm 6\%$, which is less than the standard deviations measured in the range of $\pm 10\%$. Statistically significant differences were established with a power of about 85% given these standard deviations, so the accuracy of the wear measurement was found to be acceptable.

The effect of creep was more substantial. Creep recovery is occurring after several weeks, manifesting itself both as a reduction in the diameter of the circular wear scar, and as the presence of a bulge unaccounted for in assuming the wear scar is flat. These changes in geometry resulted in an overestimation of the wear volume by 14% (due to the change in wear scar diameter), and by 62% (due to the additional presence of the bulge). However, the trends amongst the materials are the same considering the change in wear scar diameter, and similar accounting for the bulge recovery.

The investigation into creep recovery also had limitations. The difficulty in accurately measuring the radius of the recovered bulge, along with the fact that measurements accounting for creep could only be performed on the final data point for just four materials suggests that a more thorough investigation should be carried out before drawing conclusions. One issue with considering creep in the future is that the wear pins need at least one week to recover; this is not feasible when the pins are measured every 50,000 cycles during an ongoing test. Important information would be lost, such as the wear rate behavior throughout the test, and the basis of steady-state wear rate on more than one data point. Considering the consistent trends and the limitations of the investigation, creep recovery has not been taken into account in comparing the materials' wear behavior.

Microstructural Evaluation

While the tensile, fatigue, wear, and oxidation data provide robust experimental comparisons amongst the groups, the microstructure results of this study should be considered with the caveat that image analysis is not an exact method to determine microstructural parameters. However, alternate methods also have limitations. Differential scanning calorimetry combined with the Hoffman-Weeks relation is only applicable for uncross-linked materials. This is also a limitation in the method developed by Van Citters, although a scale factor is introduced to empirically account for thermodynamic effects in cross-linked materials. X-ray scattering

estimates lamellar size using an analysis based on Bragg's law, but assumes a stack of infinitely long and wide lamellae, and introduces error from its dependence on average crystallinity measurements (Fruhwrith, Fritz, Freiberger, & Glatter, 2004; Turell & Bellare, 2004).

In comparing the image analysis technique developed in this dissertation to other techniques discussed above, the parameter estimates were well-correlated with 1) differential scanning calorimetry estimates of thickness for uncross-linked materials, 2) the Van Citters estimate of lamellar size (cross-sectional area), and 3) x-ray scattering estimates of thickness on materials from another study (Simis et al., 2006). However, lamellar thickness and length were not well-correlated with the Van Citters estimates. This may be explained by the assumption made in the Van Citters method that the lamellae grow in both dimensions at the same rate, in combination with error introduced in the MPG technique by using the best-fit rectangle to approximate those dimensions. On the other hand, the area estimate does not make a thermodynamic assumption about relative rate of growth in the two dimensions, and is based solely on the number of pixels in each object rather than on a best-fit rectangle. With respect to the x-ray scattering comparison, there were only four material groups from another study for which images were available and x-ray scattering had been performed. Not enough information was reported to calculate the calorimetry or Van Citters estimates, and it is difficult to establish correlation with only four data points. One material group in particular was poorly measured by the MPG image analysis technique and likely reduced the correlation between the two methods. The lamellae in that particular material were extremely large (about 130 nm compared to 20-50 nm for most ultra-high materials), and well outside the range of lamellar sizes for which the MPG technique was developed.

It is important to note that with the procedure developed here, it is possible to acquire the distributions of lamellar dimensions while the other measures report simply a single value. It is also likely that the filtering process results in lamellae that are skewed small, but this bias is the same for all groups and so does not affect comparisons or statistical methods based on ranks. While absolute measurements of lamellar microstructure are challenging to obtain, this image analysis approach compares favorably to other methods and is appropriate for characterizing relative differences in microstructures amongst the materials.

With respect to amorphous phase microstructure, cross-link density and free radical concentration were not directly measured. However, it is well-known that cross-link density is directly related to the radiation dose (Muratoglu et al., 1999). It has also been established that artificial aging is an appropriate method to evaluate the oxidative stability of materials and that aging results are in agreement with free radical concentration measured by electron spin resonance (Collier et al., 2003; Collier, Sutula et al., 1996; Costa et al., 1998b; Edidin et al., 2000; Jahan, Wang, Schwartz, & Davidson, 1991). The artificial aging results are consistent with a recent study by Morrison and Jani (Morrison & Jani, 2009) which reported free radical concentration for similar annealed materials above 1.0×10^{15} spins/gram compared to concentrations below the level of detection for a re-melted material.

A final microstructural caveat is the relatively small range of microstructures found in the materials in this study, which limits the ability to quantitatively determine relationships amongst the treatments, mechanical performance, and microstructures. However, results are consistent

with other studies investigating ultra-high microstructure and mechanical properties. It has been similarly reported that crystallinity is highly correlated with elastic modulus (Medel et al., 2007; Simis et al., 2006) and that fatigue threshold scales better with lamellar size than with crystallinity (Simis et al., 2006). Dependence of fatigue resistance on crystallinity has also been reported in other studies that did not evaluate other lamellar size parameters (Baker et al., 2000). The results in this dissertation suggest that fatigue resistance is correlated with both lamellar size and with crystallinity, although experimentally these parameters are not independent because a cross-linked amorphous phase appears to limit both the number and size of re-formed lamellae. Lamellar thickness in this study was not correlated with fatigue resistance or with any other parameter, likely due to the small range of lamellar thickness present in these materials (interquartile ranges from 25 to 40 nm). These results taken together with the literature suggest that treatments such as re-melting that decrease lamellar size and crystallinity are detrimental to fatigue crack propagation resistance, and that sliding wear resistance is more dependent on amorphous phase parameters governed by cross-linking than by lamellar parameters.

4.5 Strength of Study

The principal strength of this study was the large number of distinct clinically-relevant processing treatments included and the full spectrum of mechanical characterization performed. For the same group of materials, fatigue crack propagation, wear, oxidation, tensile properties, and microstructure were evaluated. Materials included two untreated control materials, two highly cross-linked annealed materials, two moderately cross-linked re-melted materials, and three highly cross-linked re-melted materials. Comparisons were made amongst materials with the same total radiation dose (9 Mrad) but subjected to single and sequential annealing, as well as re-melting. Comparisons were also made amongst materials that had all been re-melted, but were subjected to various total radiation doses. A further strength of this study is that by evaluating microstructure along with fatigue resistance, wear resistance, oxidative stability, and tensile properties, relationships between the treatments, microstructure, and the resulting mechanical performance were elucidated.

Chapter 5

Implications and Future Work

5.1 Clinical Implications

This study has important clinical implications. Primarily, none of the clinically-relevant materials was able to excel in all three areas: fatigue crack propagation resistance, wear resistance, and oxidative stability. The moderately cross-linked re-melted material did equally well in all areas, but did not excel in any.

Another implication of this study is for tailoring ultra-high treatments, microstructures, and designs for better fatigue, wear, and oxidation performance. First, the untreated materials need improved wear resistance. This might be accomplished by exploring surface treatments such as polyethylene-glycol (Kane, Ashby, & Pruitt, 2009) or heterogeneous properties graded through the depth of the material (a cross-linked surface with a non-cross-linked bulk). Second, the annealed materials lack oxidative stability. This is being addressed using a chemical antioxidant (vitamin E), which is thought to scavenge more free radicals and inhibit long-term oxidation (Oral, Godleski Beckos, Malhi, & Muratoglu, 2008; Oral, Rowell, & Muratoglu, 2006; Oral, Wannomae, Rowell, & Muratoglu, 2007). Previous work on antioxidants shows that including the antioxidant in the initial resin may inhibit some of the cross-linking, but does not disrupt the formation of the lamellar microstructure (J. Furmanski et al., 2007). Third, the cross-linked re-melted materials are deficient in fatigue crack propagation resistance. Improvement may be achieved by increasing the lamellar volume fraction and lamellar size of re-melted materials, perhaps by combining cross-linking and re-melting with a secondary high pressure or thermal treatment (Bistolfi et al., 2009). The poor fatigue resistance of cross-linked re-melted materials may also be mitigated by designing ultra-high components with fewer design features such as notches and sharp corners that act as stress concentrators and crack initiation sites.

Understanding the shortcomings of the current marketed materials, as well as the relationship of mechanical performance to treatment and microstructure, allows for targeted improvements necessary to produce materials and designs that can withstand rigorous in vivo mechanical demands and improve the longevity of total joint arthroplasty.

5.2 Future Work: Computational Modeling of Microstructure

Although this dissertation begins to elucidate the relationship between microstructure and mechanical behavior, that understanding is limited because many of the microstructural parameters are confounded. For example, materials with larger lamellae tend to have a higher percent crystallinity. Also, a cross-linked amorphous phase tends to restrict the growth of large lamellae. The experimental materials in this study were processed to be clinically relevant rather than to provide a controlled range of microstructures. However, the mechanical effect of specific microstructural parameters can be investigated using computational modeling of the microstructure (Figures 5.1 and 5.2).

Preliminary finite element models have been developed to prove the feasibility of this computational approach. Two scanning electron microscope images of actual materials from this dissertation were converted into two-dimensional models in Abaqus (v. 6.6, Rhode Island). The resolution of the images is approximately 4.4 nanometers per pixel, which is about 5-6 pixels across the smallest dimension (thickness) of the lamellae. Each pixel is converted into an element in the model, with thresholding performed to assign a material (amorphous or lamellae) to each element. The two materials are assumed to be well-bonded to one another as in a typical composite analysis. This results in a 2D model with two materials, approximately 230,000 elements, and approximately 350,000 nodes representing a 2 micron by 2 micron section of the ultra-high containing over 100 lamellae.

The two materials chosen for this preliminary analysis had the same 1020 resin and the same total radiation dose of 9 Mrad, but different heat treatments (1020-9-147 and 1020-3x3-130). Since the amount of cross-linking is approximately equal for the two materials, the properties of the amorphous phase are assumed to be equivalent. The properties of the lamella themselves are also assumed to be the same, but due to the different heat treatments the materials have different lamellar microstructures (size, crystallinity, and geometry). These two materials were used to fit material properties to the amorphous and lamellar phases, attributing the 23% difference in modulus (found in this dissertation) to the known differences in lamellar microstructure (size, crystallinity, geometry).

To fit the unknown material properties of the amorphous and lamellar phases, an initial approximation was obtained using optimization analysis based on the rule of mixtures (Matlab v. 7, Natick, Massachusetts). Optimization provided initial approximations of $E = 980$ MPa and $\nu = 0.48$ for the lamellar phase, and $E = 68$ MPa and $\nu = 0.44$ for the amorphous phase. Finite element models run with these initial properties resulted in a 17.5% difference in bulk stiffness. (Percent difference of 2D stiffness is analogous to percent difference of experimentally-determined 3D modulus; stiffness is defined as the total reaction force at the constrained bottom surface divided by the imposed displacement at the top surface (10% strain)) To further refine the material properties, finite element analyses were run varying both the modulus and Poisson's ratio with the goal of a 23% difference in stiffness. Results fit $E = 1150$ MPa and $\nu = 0.48$ for the lamellar phase, and $E = 50$ MPa and $\nu = 0.44$ for the amorphous phase. A subsequent sensitivity analysis showed that the model stiffness was more sensitive to changes in the amorphous modulus than in the lamellar modulus (by an order of magnitude). The model stiffness was equally sensitive to changing the Poisson's ratio in the amorphous and in the lamellar phase. Overall, model stiffness was more sensitive to changes in modulus than in Poisson's ratio.

This preliminary exploration demonstrates that using the scanning electron microscope images of actual experimentally-characterized materials can be used to build computational models of the microstructure. The next steps of this study are to use the fitted material properties to predict the percent difference in stiffness (modulus) of the 1020-9-130 material, which has the same amorphous and lamellar properties but a slightly different lamellar microstructure. After this validation is complete, a verification of the model can be performed by increasing the number of elements and making sure the results are consistent.

After the models and the material properties have been fully validated and verified, an untreated material (1020-0-0) with a known lamellar geometry, known lamellar properties, and a known modulus can be used to determine the amorphous properties for an uncross-linked material. Then idealized microstructures can be developed to test the effect on stiffness (for both cross-linked and uncross-linked ultra-high) when varying one microstructural parameter (percent crystallinity, lamellar thickness, lamellar length, amorphous properties representing cross-linking) while holding all others constant. These results can be verified in part with the experimental correlations found in this dissertation.

Another application of computational modeling of the microstructure of ultra-high is to explore the effect of lamellar orientation and plastically-deformed states (discussed more in Appendix B) on the local mechanical behavior. This can be related to the oriented damage layer that is a precursor to wear, and to the theory of energy dissipation at the crack tip presented in this dissertation. From previous experimental work, the stress-strain relationship for the individual materials is known at each point of the stress-strain curve, and so could be approximated as locally linear for use in the models.

It is important to note the limitations of this proposed computational analysis. The models are two-dimensional and linear elastic and so results are somewhat restricted to the stiffness behavior at small strains, or to behavior at a specific linearly-approximated part of the stress-strain curve. A non-linear analysis would be required to probe yielding or failure behavior. However, with the experimental characterization performed in the dissertation, it would be possible to refine the model to incorporate a non-linear viscoelastic material model. Another limitation is that the two phases are considered well-bonded and so interactions and tie molecules are not taken into account. This assumption is violated at high strains near failure where tie molecules become important. For immediate future work, small strain behavior can still provide important insight on relationships between microstructural properties and mechanical behavior, as well as orientation effects, which will provide a deeper understanding of the micromechanisms of wear and crack propagation resistance.

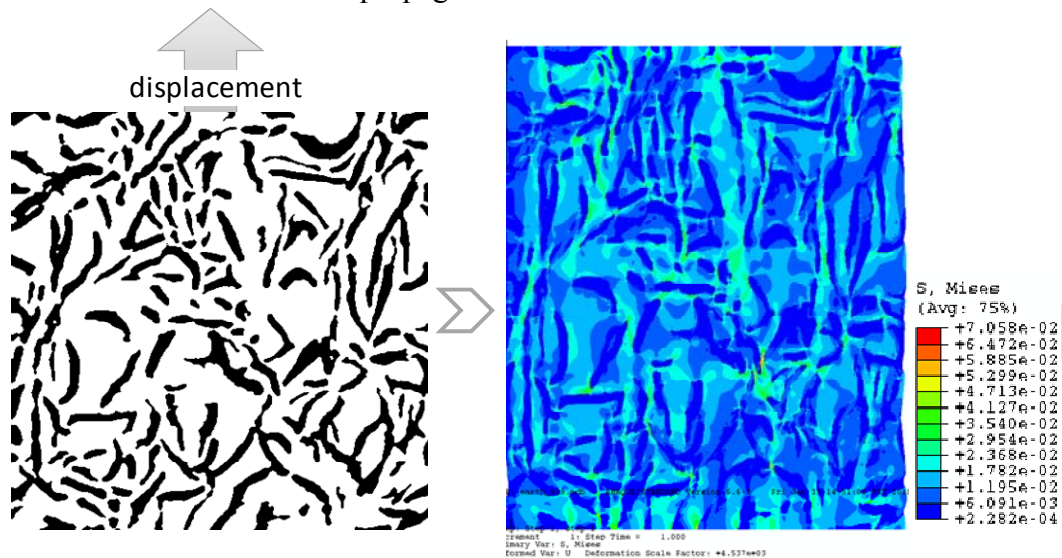


Figure 5.1. Representative finite element model with boundary conditions and displacement applied to obtain the stiffness. Dimensions of the unstrained model (*left*) are 2 x 2 microns.

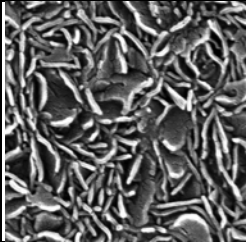
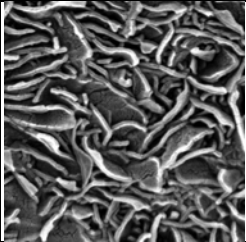
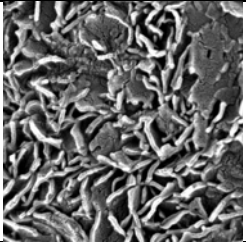
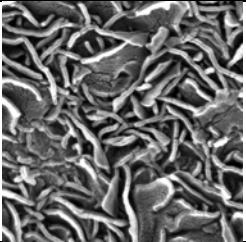


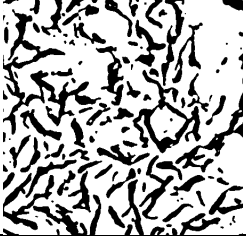

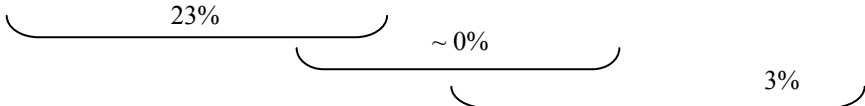
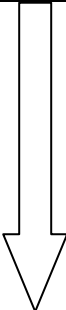
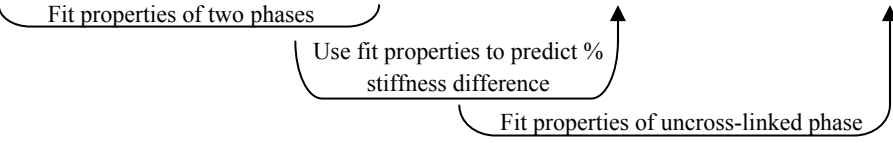
Material Resin Mrad °C	1020 9 147	1020 3x3 130	1020 9 130	1020 0 0	Custom	
Scanning Electron Microscope Image (2 x 2 microns)					none	
Model (2 x 2 microns)					Custom drawn	
Amorp Phase Props.	Highly cross-linked (networked matrix)			Uncross-linked (un-networked matrix)	Either	
Crystalline Phase	Props.	Crystalline (hard inclusions)				
	Microstructure Size	Small	Medium	Medium	Large	Varied
	Crystallinity (Vol %)	48%	59%	58%	54%	Varied
Experi- mental Modulus (MPa)	312	390	392	380	Predict	
% Diff in Modulus (3D)/ Stiffness (2D)						
Steps						
<div style="border: 2px solid black; padding: 5px; display: inline-block;"> Parameter study to determine effect on modulus of lamellar size, crystallinity, orientation </div>						

Figure 5.2. Schematic of future computational modeling: fit properties, validate, and perform parameter study.

5.3 Closing Thoughts

This dissertation is the first study to simultaneously evaluate fatigue crack propagation, wear, and oxidation in a wide variety of clinically-relevant ultra-high. The results have important clinical implications. Primarily, none of the clinically-relevant materials was able to excel in all three areas - fatigue crack propagation resistance, wear resistance, and oxidative stability. The trade-off demonstrated is critical to the material's long-term success in total joint replacements: 1) excessive wear is a historical problem that results in large numbers of failures; 2) poor resistance to fatigue crack propagation and fracture has been implicated in recent reports of cross-linked re-melted hip liners fracturing in vivo; and 3) highly oxidized ultra-high cannot adequately withstand in vivo demands. Although this dissertation begins to elucidate the relationship between processing treatments, microstructure, and mechanical behavior, our understanding is limited because many of the microstructural parameters are confounded. The mechanical impact of specific microstructural parameters can be investigated further using computational modeling. Understanding the shortcomings of the current marketed materials, as well as the relationship of mechanical performance to treatment and microstructure through experimental and computational investigation, allows for targeted improvements needed to produce materials and designs that can withstand rigorous in vivo mechanical demands and improve the longevity of total joint arthroplasty.

References

- ASTM F2102-01: Standard Guide for Evaluating the Extent of Oxidation in Ultra High Molecular Weight Polyethylene Fabricated Forms Intended for Surgical Implants, (2001).
- Baker, D. A., Bellare, A., & Pruitt, L. (2003). The effects of degree of crosslinking on the fatigue crack initiation and propagation resistance of orthopedic-grade polyethylene. *J Biomed Mater Res A*, 66(1), 146-154.
- Baker, D. A., Hastings, R. S., & Pruitt, L. (2000). Compression and tension fatigue resistance of medical grade ultra high molecular weight polyethylene: the effect of morphology, sterilization, aging and temperature. *Polymer*, 41(2), 795-808.
- Baker, D. A., Pruitt, L., & Bellare, A. (2001). Ultra-small angle X-ray scattering to detect fatigue damage in polymers. *Journal of Materials Science Letters*, 20(12), 1163-1164.
- Bartczak, Z., & Kozanecki, M. (2005). Influence of molecular parameters on high-strain deformation of polyethylene in the plane-strain compression. Part I. Stress-strain behavior. *Polymer*, 46(19), 8210-8221.
- Bartel, D. L., Bicknell, V. L., & Wright, T. M. (1986). The effect of conformity, thickness, and material on stresses in ultra-high molecular weight components for total joint replacement. *J Bone Joint Surg Am*, 68(7), 1041-1051.
- Bartel, D. L., Rawlinson, J. J., Burstein, A. H., Ranawat, C. S., & Flynn, W. F., Jr. (1995). Stresses in polyethylene components of contemporary total knee replacements. *Clin Orthop Relat Res*(317), 76-82.
- Bellare, A., Schnablegger, H., & Cohen, R. E. (1995). A Small-Angle X-Ray-Scattering Study of High-Density Polyethylene and Ultrahigh Molecular-Weight Polyethylene. *Macromolecules*, 28(23), 7585-7588.
- Bistolfi, A., Turell, M. B., Lee, Y. L., & Bellare, A. (2009). Tensile and tribological properties of high-crystallinity radiation crosslinked UHMWPE. *J Biomed Mater Res B Appl Biomater*, 90(1), 137-144.
- Bozic, K. J., Kurtz, S., Lau, E., Ong, K., Chiu, V., Vail, T. P., et al. (2009a). The epidemiology of bearing surface usage in total hip arthroplasty in the United States. *J Bone Joint Surg Am*, 91(7), 1614-1620.
- Bozic, K. J., Kurtz, S. M., Lau, E., Ong, K., Chiu, V., Vail, T. P., et al. (2009b). The Epidemiology of Revision Total Knee Arthroplasty in the United States. *Clin Orthop Relat Res*.
- Bozic, K. J., Kurtz, S. M., Lau, E., Ong, K., Vail, T. P., & Berry, D. J. (2009). The epidemiology of revision total hip arthroplasty in the United States. *J Bone Joint Surg Am*, 91(1), 128-133.

- Brown, S. A., Flemming, C. A., Kawalec, J. S., Placko, H. E., Vassaux, C., Merritt, K., et al. (1995). Fretting corrosion accelerates crevice corrosion of modular hip tapers. *J Appl Biomater*, 6(1), 19-26.
- Burris, D., & Sawyer, W. (2009). Measurement Uncertainties in Wear Rates. *Tribology Letters*, 36(1), 81-87.
- Collier, J. P., Bargmann, L. S., Currier, B. H., Mayor, M. B., Currier, J. H., & Bargmann, B. C. (1998). An analysis of hylamer and polyethylene bearings from retrieved acetabular components. *Orthopedics*, 21(8), 865-871.
- Collier, J. P., Currier, B. H., Kennedy, F. E., Currier, J. H., Timmins, G. S., Jackson, S. K., et al. (2003). Comparison of cross-linked polyethylene materials for orthopaedic applications. *Clin Orthop Relat Res*(414), 289-304.
- Collier, J. P., Sperling, D. K., Currier, J. H., Sutula, L. C., Saum, K. A., & Mayor, M. B. (1996). Impact of gamma sterilization on clinical performance of polyethylene in the knee. *J Arthroplasty*, 11(4), 377-389.
- Collier, J. P., Surprenant, V. A., Jensen, R. E., Mayor, M. B., & Surprenant, H. P. (1992). Corrosion between the components of modular femoral hip prostheses. *J Bone Joint Surg Br*, 74(4), 511-517.
- Collier, J. P., Sutula, L. C., Currier, B. H., Currier, J. H., Wooding, R. E., Williams, I. R., et al. (1996). Overview of polyethylene as a bearing material: comparison of sterilization methods. *Clin Orthop Relat Res*(333), 76-86.
- Costa, L., Bracco, P., Brach del Prever, E. M., Kurtz, S. M., & Gallinaro, P. (2006). Oxidation and oxidation potential in contemporary packaging for polyethylene total joint replacement components. *J Biomed Mater Res B Appl Biomater*, 78(1), 20-26.
- Costa, L., Bracco, P., del Prever, E. B., Luda, M. P., & Trossarelli, L. (2001). Analysis of products diffused into UHMWPE prosthetic components in vivo. *Biomaterials*, 22(4), 307-315.
- Costa, L., Luda, M. P., Trossarelli, L., Brach del Prever, E. M., Crova, M., & Gallinaro, P. (1998a). In vivo UHMWPE biodegradation of retrieved prosthesis. *Biomaterials*, 19(15), 1371-1385.
- Costa, L., Luda, M. P., Trossarelli, L., Brach del Prever, E. M., Crova, M., & Gallinaro, P. (1998b). Oxidation in orthopaedic UHMWPE sterilized by gamma-radiation and ethylene oxide. *Biomaterials*, 19(7-9), 659-668.
- Crowninshield, R. D., & Muratoglu, O. K. (2008). How have new sterilization techniques and new forms of polyethylene influenced wear in total joint replacement? *J Am Acad Orthop Surg*, 16 Suppl 1, S80-85.
- Currier, B. H., Currier, J. H., Collier, J. P., Mayor, M. B., & Scott, R. D. (1997). Shelf life and in vivo duration. Impacts on performance of tibial bearings. *Clin Orthop Relat Res*(342), 111-122.

- Currier, B. H., Currier, J. H., Mayor, M. B., Lyford, K. A., Collier, J. P., & Van Citters, D. W. (2007). Evaluation of oxidation and fatigue damage of retrieved crossfire polyethylene acetabular cups. *J Bone Joint Surg Am*, 89(9), 2023-2029.
- Currier, B. H., Currier, J. H., Mayor, M. B., Lyford, K. A., Van Citters, D. W., & Collier, J. P. (2007). In vivo oxidation of gamma-barrier-sterilized ultra-high-molecular-weight polyethylene bearings. *J Arthroplasty*, 22(5), 721-731.
- Dumbleton, J. H. (1981). *Tribology of Natural and Artificial Joints*. Amsterdam: Elsevier.
- Dumbleton, J. H., D'Antonio, J. A., Manley, M. T., Capello, W. N., & Wang, A. (2006). The basis for a second-generation highly cross-linked UHMWPE. *Clin Orthop Relat Res*, 453, 265-271.
- Edidin, A. A., Jewett, C. W., Kalinowski, A., Kwarteng, K., & Kurtz, S. M. (2000). Degradation of mechanical behavior in UHMWPE after natural and accelerated aging. *Biomaterials*, 21(14), 1451-1460.
- Edidin, A. A., Pruitt, L., Jewett, C. W., Crane, D. J., Roberts, D., & Kurtz, S. M. (1999). Plasticity-induced damage layer is a precursor to wear in radiation-cross-linked UHMWPE acetabular components for total hip replacement. Ultra-high-molecular-weight polyethylene. *J Arthroplasty*, 14(5), 616-627.
- FDA. (2009). U.S. Food and Drug Administration's Maude Database (Manufacturer and User Facility Device Experience) (Publication. Retrieved January 8, 2009: <http://www.accessdata.fda.gov/scripts/cdrh/cfdocs/cfMAUDE/search.CFM>)
- Fisher, J. (2001). Biomedical Applications. In B. Bhushan (Ed.), *Modern Tribology Handbook* (pp. 1593-1609): CRC Press.
- Fisher, J., & Dowson, D. (1991). Tribology of total artificial joints. *Proc Inst Mech Eng H*, 205(2), 73-79.
- Fisher, J., Dowson, D., Hamdzah, H., & Lee, H. L. (1994). The effect of sliding velocity on the friction and wear of UHMWPE for use in total artificial joints. *Wear*, 175(1-2), 219-225.
- Fruhvirth, T., Fritz, G., Freiburger, N., & Glatter, O. (2004). Structure and order in lamellar phases determined by small-angle scattering. *Journal of Applied Crystallography*, 37, 703-710.
- Furmanski, J., Anderson, M., Bal, S., Greenwald, A. S., Halley, D., Penenberg, B., et al. (2009). Clinical fracture of cross-linked UHMWPE acetabular liners. *Biomaterials*, 30(29), 5572-5582.
- Furmanski, J., Atwood, S. A., Feest, E., Tang, J., Hoang, M., & Pruitt, L. (2007, February 11-14, 2007). *Effect of Vitamin E on Fatigue of Irradiated UHMWPE*. Paper presented at the 53rd Annual Meeting of the Orthopaedic Research Society, San Diego, CA.
- Furmanski, J., & Pruitt, L. A. (2007). Peak stress intensity dictates fatigue crack propagation in UHMWPE. *Polymer*, 48(12), 3512-3519.

- Gencur, S. J., Rimnac, C. M., & Kurtz, S. M. (2006). Fatigue crack propagation resistance of virgin and highly crosslinked, thermally treated ultra-high molecular weight polyethylene. *Biomaterials*, 27(8), 1550-1557.
- Gilbert, J. L., Buckley, C. A., & Jacobs, J. J. (1993). In vivo corrosion of modular hip prosthesis components in mixed and similar metal combinations. The effect of crevice, stress, motion, and alloy coupling. *J Biomed Mater Res*, 27(12), 1533-1544.
- Glantz, S. A. (2005). *Primer of Biostatistics* (6 ed.). New York: McGraw-Hill
- Goldman, M., Gronsky, R., & Pruitt, L. (1998). The influence of sterilization technique and ageing on the structure and morphology of medical-grade ultrahigh molecular weight polyethylene. *J Mater Sci Mater Med*, 9(4), 207-212.
- Harris, W. H. (2001). Wear and periprosthetic osteolysis: the problem. *Clin Orthop Relat Res*(393), 66-70.
- Hoffman, J., & Miller, R. (1997). Kinetics of crystallization from the melt and chain folding in polyethylene fractions revisited: Theory and experiment. *Polymer*, 38, 3151-3212.
- Hoffman, J., & Weeks, J. (1962). Melting Process and Equilibrium Melting Temperature of Polychlorotrifluoroethylene. *Journal of Research of the National Bureau of Standards Section a-Physics and Chemistry*, 66, 13-&.
- Ingram, J. H., Stone, M., Fisher, J., & Ingham, E. (2004). The influence of molecular weight, crosslinking and counterface roughness on TNF-alpha production by macrophages in response to ultra high molecular weight polyethylene particles. *Biomaterials*, 25(17), 3511-3522.
- Jacobs, J. J., Gilbert, J. L., & Urban, R. M. (1998). Corrosion of metal orthopaedic implants. *J Bone Joint Surg Am*, 80(2), 268-282.
- Jahan, M. S., Wang, C., Schwartz, G., & Davidson, J. A. (1991). Combined chemical and mechanical effects on free radicals in UHMWPE joints during implantation. *J Biomed Mater Res*, 25(8), 1005-1017.
- Kane, S. R., Ashby, P. D., & Pruitt, L. A. Characterization and tribology of PEG-like coatings on UHMWPE for total hip replacements. *J Biomed Mater Res A*, 92(4), 1500-1509.
- Kane, S. R., Ashby, P. D., & Pruitt, L. A. (2009). Microscale wear behavior and crosslinking of PEG-like coatings for total hip replacements. *J Mater Sci Mater Med*.
- Klapperich, C., Komvopoulos, K., & Pruitt, L. (1999). Tribological Properties and Microstructure Evolution of Ultra-High Molecular Weight Polyethylene. *Journal of Tribology*, 121(2), 394-402.
- Kop, A. M., & Swarts, E. (2009). Corrosion of a hip stem with a modular neck taper junction: a retrieval study of 16 cases. *J Arthroplasty*, 24(7), 1019-1023.

- Kurtz, S., Mowat, F., Ong, K., Chan, N., Lau, E., & Halpern, M. (2005). Prevalence of primary and revision total hip and knee arthroplasty in the United States from 1990 through 2002. *J Bone Joint Surg Am*, 87(7), 1487-1497.
- Kurtz, S., Ong, K., Lau, E., Mowat, F., & Halpern, M. (2007). Projections of primary and revision hip and knee arthroplasty in the United States from 2005 to 2030. *J Bone Joint Surg Am*, 89(4), 780-785.
- Kurtz, S. M. (2009a). From Ethylene Gas to UHMWPE Component: The Process of Producing Orthopedic Implants. In *UHMWPE Biomaterials Handbook (Second Edition)* (pp. 7-19). Boston: Academic Press.
- Kurtz, S. M. (2009b). The Origins and Adaptations of UHMWPE for Knee Replacements. In *UHMWPE Biomaterials Handbook (Second Edition)* (pp. 81-95). Boston: Academic Press.
- Kurtz, S. M. (2009c). The Origins of UHMWPE in Total Hip Arthroplasty. In *UHMWPE Biomaterials Handbook (Second Edition)* (pp. 31-41). Boston: Academic Press.
- Kurtz, S. M. (2009d). A Primer on UHMWPE. In *UHMWPE Biomaterials Handbook (Second Edition)* (pp. 1-6). Boston: Academic Press.
- Kurtz, S. M., Muratoglu, O. K., Buchanan, F., Currier, B., Gsell, R., Greer, K., et al. (2001). Interlaboratory reproducibility of standard accelerated aging methods for oxidation of UHMWPE. *Biomaterials*, 22(13), 1731-1737.
- Kurtz, S. M., Muratoglu, O. K., Evans, M., & Edidin, A. A. (1999). Advances in the processing, sterilization, and crosslinking of ultra-high molecular weight polyethylene for total joint arthroplasty. *Biomaterials*, 20(18), 1659-1688.
- Kurtz, S. M., Ong, K. L., Schmier, J., Mowat, F., Saleh, K., Dybvik, E., et al. (2007). Future clinical and economic impact of revision total hip and knee arthroplasty. *J Bone Joint Surg Am*, 89 Suppl 3, 144-151.
- Lenth, R. V. (2006-2009). Java Applets for Power and Sample Size. Retrieved October 29, 2009, from <http://www.stat.uiowa.edu/~rlenth/Power>
- Li, S., & Burstein, A. H. (1994). Ultra-high molecular weight polyethylene. The material and its use in total joint implants. *J Bone Joint Surg Am*, 76(7), 1080-1090.
- Lin, L., & Argon, A. S. (1994). Structure and plastic deformation of polyethylene. *Journal of Materials Science*, 29(2), 294-323.
- Lynch, W. (1982). *Implants: Reconstructing the Human Body*: Van Nostrand Reinhold Company.
- McKellop, H., Shen, F. W., Lu, B., Campbell, P., & Salovey, R. (1999). Development of an extremely wear-resistant ultra high molecular weight polyethylene for total hip replacements. *J Orthop Res*, 17(2), 157-167.

- Medel, F. J., Kurtz, S. M., Hozack, W. J., Parvizi, J., Purtill, J. J., Sharkey, P. F., et al. (2009). Gamma inert sterilization: a solution to polyethylene oxidation? *J Bone Joint Surg Am*, *91*(4), 839-849.
- Medel, F. J., Pena, P., Cegonino, J., Gomez-Barrena, E., & Puertolas, J. A. (2007). Comparative fatigue behavior and toughness of remelted and annealed highly crosslinked polyethylenes. *J Biomed Mater Res B Appl Biomater*, *83*(2), 380-390.
- Meng, D., & Kathryn, E. U. (1998). Analysis of thermal properties of polymeric biomaterials. I. Ultrahigh-molecular-weight polyethylene. *Journal of Applied Polymer Science*, *68*(8), 1353-1361.
- Morrison, M. L., & Jani, S. (2009). Evaluation of sequentially crosslinked ultra-high molecular weight polyethylene. *J Biomed Mater Res B Appl Biomater*, *90*(1), 87-100.
- Mow, V. C., & Hayes, W. C. (1991). *Basic Orthopaedic Biomechanics*. New York: Raven Press.
- Muratoglu, O. K., Bragdon, C. R., O'Connor, D. O., Jasty, M., & Harris, W. H. (2001). A novel method of cross-linking ultra-high-molecular-weight polyethylene to improve wear, reduce oxidation, and retain mechanical properties. Recipient of the 1999 HAP Paul Award. *J Arthroplasty*, *16*(2), 149-160.
- Muratoglu, O. K., Bragdon, C. R., O'Connor, D. O., Jasty, M., Harris, W. H., Gul, R., et al. (1999). Unified wear model for highly crosslinked ultra-high molecular weight polyethylenes (UHMWPE). *Biomaterials*, *20*(16), 1463-1470.
- Olley, R., & Bassett, D. (1977). Molecular-conformations in polyethylene after recrystallization or annealing at high-pressures. *Journal of Polymer Science B*, *15*(6), 1011-1027.
- Ong, K. L., Mowat, F. S., Chan, N., Lau, E., Halpern, M. T., & Kurtz, S. M. (2006). Economic burden of revision hip and knee arthroplasty in Medicare enrollees. *Clin Orthop Relat Res*, *446*, 22-28.
- Oral, E., Godleski Beckos, C., Malhi, A. S., & Muratoglu, O. K. (2008). The effects of high dose irradiation on the cross-linking of vitamin E-blended ultrahigh molecular weight polyethylene. *Biomaterials*, *29*(26), 3557-3560.
- Oral, E., Rowell, S. L., & Muratoglu, O. K. (2006). The effect of alpha-tocopherol on the oxidation and free radical decay in irradiated UHMWPE. *Biomaterials*, *27*(32), 5580-5587.
- Oral, E., Wannomae, K. K., Rowell, S. L., & Muratoglu, O. K. (2007). Diffusion of vitamin E in ultra-high molecular weight polyethylene. *Biomaterials*, *28*(35), 5225-5237.
- Pascaud, R. S., Evans, W. T., McCullagh, P. J., & FitzPatrick, D. (1996). Effects of batch to batch variations and test methodology on degree of crystallinity and melting temperature of UHMW-PE as measured by differential scanning calorimetry. *J Biomed Mater Res*, *32*(4), 619-626.

- Patten, E. W. (2008). *Multi-axial tribo-system: rolling, sliding and rotation of UHMWPE in total joint replacements*. University of California at Berkeley, Berkeley, CA.
- Pruitt, L., & Bailey, L. (1998). Factors affecting near-threshold fatigue crack propagation behavior of orthopedic grade ultra high molecular weight polyethylene. *Polymer*, 39(8-9), 1545-1553.
- Pruitt, L. A. (2005). Deformation, yielding, fracture and fatigue behavior of conventional and highly cross-linked ultra high molecular weight polyethylene. *Biomaterials*, 26(8), 905-915.
- Ries, M. D., & Pruitt, L. (2005). Effect of cross-linking on the microstructure and mechanical properties of ultra-high molecular weight polyethylene. *Clin Orthop Relat Res*, 440, 149-156.
- Rockwood, C. A., & Wirth, M. A. (2002). Observation on retrieved Hylamer glenoids in shoulder arthroplasty: Problems associated with sterilization by gamma irradiation in air. *Journal of Shoulder and Elbow Surgery*, 11(2), 191-197.
- Saikko, V. (2006). Effect of contact pressure on wear and friction of ultra-high molecular weight polyethylene in multidirectional sliding. *Proceedings of the Institution of Mechanical Engineers, Part H: Journal of Engineering in Medicine*, 220(7), 723-731.
- Schaaff, P. (2004). The role of fretting damage in total hip arthroplasty with modular design hip joints – evaluation of retrieval studies and experimental simulation methods. *Journal of Applied Biomaterials and Biomechanics*, 2, 121-135.
- Shih, C. F., Lorenzi, H. G., & Andrews, W. R. (1977). Elastic compliances and stress-intensity factors for side-grooved compact specimens. *International Journal of Fracture*, 13(4), 544-548.
- Simis, K. S., Bistolfi, A., Bellare, A., & Pruitt, L. A. (2006). The combined effects of crosslinking and high crystallinity on the microstructural and mechanical properties of ultra high molecular weight polyethylene. *Biomaterials*, 27(9), 1688-1694.
- Sutula, L. C., Collier, J. P., Saum, K. A., Currier, B. H., Currier, J. H., Sanford, W. M., et al. (1995). The Otto Aufranc Award. Impact of gamma sterilization on clinical performance of polyethylene in the hip. *Clin Orthop Relat Res*(319), 28-40.
- Tower, S. S., Currier, J. H., Currier, B. H., Lyford, K. A., Van Citters, D. W., & Mayor, M. B. (2007). Rim cracking of the cross-linked longevity polyethylene acetabular liner after total hip arthroplasty. *J Bone Joint Surg Am*, 89(10), 2212-2217.
- Turell, M. B., & Bellare, A. (2004). A study of the nanostructure and tensile properties of ultra-high molecular weight polyethylene. *Biomaterials*, 25(17), 3389-3398.
- Van Citters, D. W. (2003). *Fatigue Failure of UHMWPE: The Development and Application of Novel Methods and Devices*. Unpublished Master of Science, Dartmouth College, Hanover, NH.

- Van Citters, D. W. (2006). *An Investigation of the Microstructural, Mechanical Properties, and Tribological Performance of Ultra High Molecular Weight Polyethylene for Applications in Total Joint Arthroplasty*. Dartmouth College, Hanover, NH.
- Van Citters, D. W., Kennedy, F. E., & Collier, J. P. (2007). Rolling sliding wear of UHMWPE for knee bearing applications. *Wear*, 263(7-12), 1087-1094.
- Viano, A. M., Spence, K. E., Shanks, M. A., Scott, M. A., Redfearn, R. D., Carlson, C. W., et al. (2007). Structural and chemical changes in ultra-high-molecular-weight polyethylene due to gamma radiation-induced crosslinking and annealing in air. *Biomed Mater Eng*, 17(5), 257-268.
- Viceconti, M., Baleani, M., Squarzoni, S., & Toni, A. (1997). Fretting wear in a modular neck hip prosthesis. *J Biomed Mater Res*, 35(2), 207-216.
- Wang, A. (2001). A unified theory of wear for ultra-high molecular weight polyethylene in multi-directional sliding. *Wear*, 248(1-2), 38-47.
- Wang, A., Stark, C., & Dumbleton, J. H. (1996). Mechanistic and morphological origins of ultra-high molecular weight polyethylene wear debris in total joint replacement prostheses. *Proc Inst Mech Eng H*, 210(3), 141-155.
- Wang, A., Sun, D. C., Yau, S. S., Edwards, B., Sokol, M., Essner, A., et al. (1997). Orientation softening in the deformation and wear of ultra-high molecular weight polyethylene. *Wear*, 203-204, 230-241.
- Wang, A., Yau, S. S., Essner, A., Herrera, L., Manley, M., & Dumbleton, J. (2008). A highly crosslinked UHMWPE for CR and PS total knee arthroplasties. *J Arthroplasty*, 23(4), 559-566.
- Williams, J. A. (1994). *Engineering Tribology*. Oxford: Oxford University Press.
- Wright Medical Technology, I. Profemur® Z Hip Stems: Information for Physicians. Retrieved July 1, 2009, from <http://www.wmt.com/Physicians/Products/Hips/ProfemurZHipStems.asp>
- Zhou, J., & Komvopoulos, K. (2005). Wear Mechanisms of Untreated and Gamma Irradiated Ultra-High Molecular Weight Polyethylene for Total Joint Replacements. *Journal of Tribology*, 127(2), 273-279.

Appendix A

Clinical Case of Fracture in an Orthopaedic Implant

A.1 Introduction

This dissertation has discussed the potential for failure of orthopaedic implants by fatigue crack propagation (and ultimately fracture) of the ultra-high component. Orthopaedic implants can also fail by fracture of the metal components. This clinical case illustrates the factors contributing to fracture of the metal stem of a hip implant, including modular design, fretting and corrosion.

Modularity is an important aspect of total hip replacement design. A modular Morse taper is commonly used to attach the femoral head to the titanium alloy stem. Newer double-modular designs incorporate a second interface at the neck-stem junction. Increased modularity allows the surgeon to restore patient anatomy such as leg length, lateral offset, and femoral anteversion, and to better balance the soft tissue for optimal biomechanics. However, modularity also increases the number of mechanical junctions which may lead to fretting (micromotion) (Viceconti, Baleani, Squarzoni, & Toni, 1997), corrosion (Collier, Surprenant, Jensen, Mayor, & Surprenant, 1992; Jacobs, Gilbert, & Urban, 1998), and ultimately fracture of the device.

A catastrophically-failed double-modular Profemur® Z (Wright Medical, Arlington, TN) stem with a fractured neck component at the neck-stem junction was evaluated. This retrieval is an opportunity to analyze the mechanical failure mechanisms associated with a double-modular design. It was hypothesized that modularity at this junction resulted in fretting and crevice-corrosion, which led to crack initiation and, upon the application an overload event, to fracture (Figure A.1).

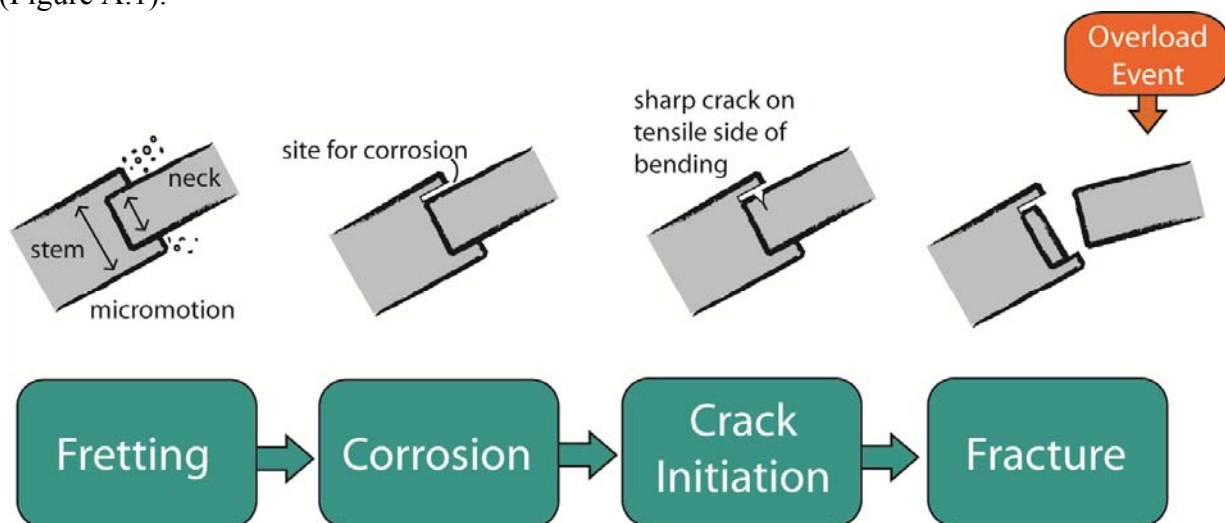


Figure A.1. Schematic illustration of the fracture process (not to scale): **fretting** due to micromotion between the neck and stem results in breaking down the passive oxide layer on the titanium; crevice **corrosion** is caused by the constant loss and repassivation of the oxide layer; **crack initiation** results from the exacerbated local environment; and finally **fracture** upon the application of an isolated overload.

A.2 Case Report

In June, 2006, a 30 year old man with Rheumatoid Arthritis who was 6'6", 242 lbs (BMI: 29) underwent an uncomplicated right total hip arthroplasty with a cementless ProFemur® Z hip stem with a long neutral neck and ceramic-on-ceramic articulation. His hip functioned well until April, 2008, when he suffered a fall on his right hip, and was taken to the emergency room, where radiographs revealed a fractured femoral stem. Subsequent revision surgery revealed a fracture of the modular neck component approximately 2 mm below the edge of the stem. The portion of the fractured neck press-fit down inside the stem could not be removed from the stem (Figure A.2).



Figure A.2. (Left) Anterior-posterior radiograph showing fracture of the modular neck. (Right) The Profemur Z® retrieval with fracture of the modular neck component about 2 mm below the edge of the stem. The fractured region of interest (boxed) is shown in cross-section in Figure A.3 and in detailed side-view in Figure A.4.

The Profemur® Z design is based on double-modular devices used extensively in Europe, and was first introduced to the U.S. in 2002 after approval by the FDA. The stem and neck are both manufactured from an orthopaedic titanium alloy, and are offered in 9 stem sizes and 12 neck sizes to accommodate a range of leg length and femoral anteversion adjustments (Wright Medical Technology).

The fracture surfaces of the retrieval were inspected using optical and scanning electron microscopy. Optical images were taken using a high-resolution digital camera (Sony XCD-SX910, Tokyo, Japan), and scanning electron micrographs were obtained using a Hitachi TM-1000 at magnifications up to 500X (Schaumburg, Illinois).

A.3 Results

Visual inspection and microscopy of the fracture surface revealed large pits at the fracture initiation site. The initiation site was identified at the center of large-scale concentric crescent-shaped features near the lateral anterior corner of the neck (Figure A.3). These crescent-shaped features were determined not to be beach marks after inspection with scanning electron microscopy, indicating that the fracture was not induced by fatigue. Further evaluation of the initiation site with scanning electron microscopy showed pitting at the edge of the fracture surface, including a large pit nearly 200 microns in diameter (Figure A.3).

The fracture surface also indicates several modes of fracture which suggest a chronology for the fracture process: 1) the dark, rough area near the initiation site is indicative of an initial sharp crack due to crevice corrosion, 2) the lighter, smooth area is likely the region of catastrophic fracture, and 3) the region of tearing in the opposite diagonal corner is where the component was finally torn (fractured) into two pieces (Figure A.3).

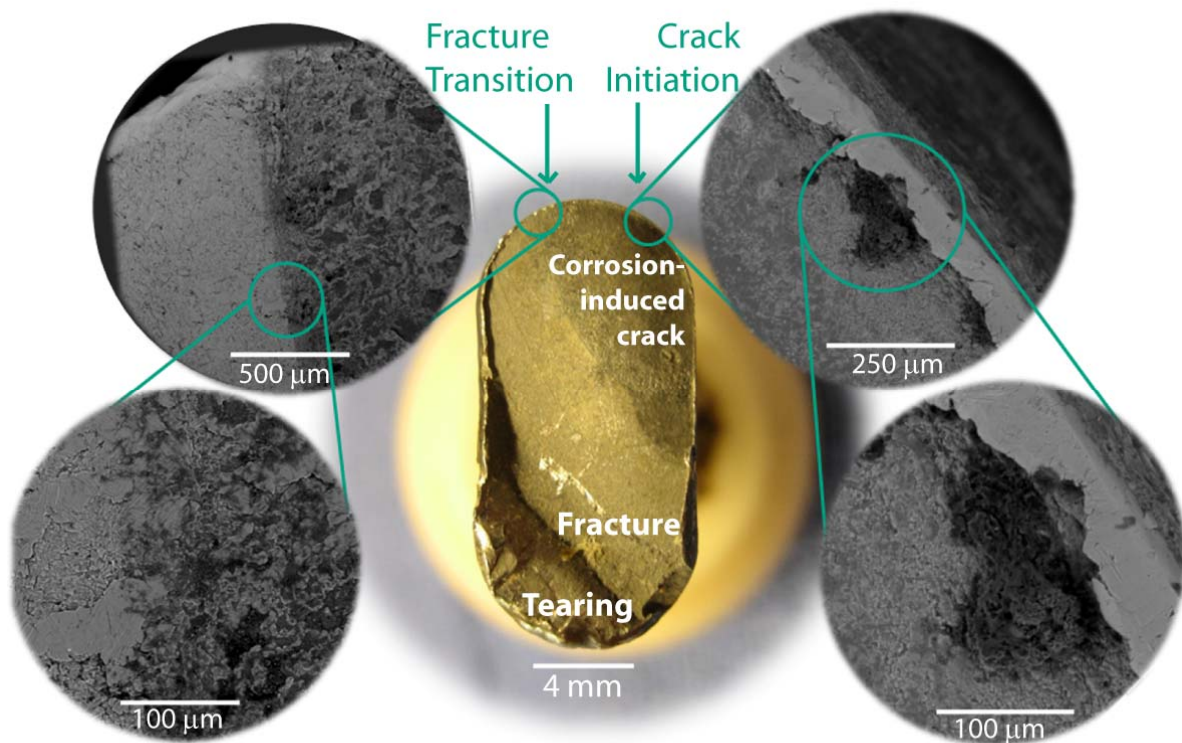


Figure A.3. Fracture surface showing the initiation site near a large pit (*right*) and the transition to catastrophic fracture (*left*). A region of tearing is seen in the corner opposite initiation, where the component finally fractured into two pieces. Note that the initiation site at the lateral anterior corner occurred on the tensile side of bending.

The outer surface of the neck at the neck-stem junction shows areas of burnishing, indicating micromotion and fretting wear (Figure A.4). Also, the edge of the fracture surface was folded over, probably due to contact with the mating surface during patient movement before retrieval.

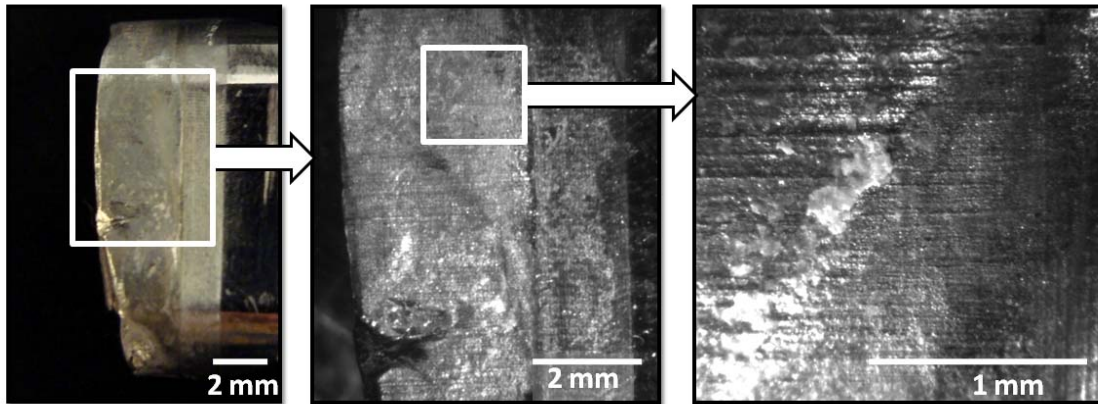


Figure A.4. Optical microscopy depicting areas of burnishing and fretting, which indicate micromotion between the neck and stem. This region is zoomed-in on the box in Figure A.2.

A.4 Discussion

This retrieval illustrates that stem-neck modularity contributes to susceptibility to corrosion-induced fracture *in vivo*. The retrieval exhibits fretting at the neck-stem junction, large pits at the crack initiation site, and several modes of fracture. This evidence suggests that micromotion at the modular interface between the neck and the stem resulted in fretting which led to crevice corrosion and pitting. This process generated a sharp crack that, upon the event of the patient's fall, resulted in catastrophic fracture of the neck (Figure A.1).

Orthopaedic metal implants are susceptible to corrosion due to the body's aggressive environment. Orthopaedic alloys, including titanium as illustrated in this case, rely on a passive oxide layer on the surface for protection against corrosion. However, fretting can continually wear away the oxide film (TiO_2), requiring constant repassivation. This is one reason that titanium is not typically used as a bearing surface in orthopaedics. This repassivation process, when occurring in a crevice such as the modular neck-stem interface, depletes the limited oxygen supply and decreases the local pH (Jacobs et al., 1998). This progression exacerbates the acidic environment and promotes further corrosion, resulting in pitting and the formation of sharp cracks.

Corrosion-induced cracks may result in catastrophic fracture upon the application of high stresses at the neck-stem junction. This process is called stress corrosion cracking and is often associated with tensile stresses such as the bending stress at the initiation site of this retrieval (Gilbert, Buckley, & Jacobs, 1993). In the absence of high stresses, a corrosion-induced crack may not result in fracture. Similarly, in the absence of a corrosion-induced crack, the same high stresses may not result in fracture. However, this retrieval shows that a critical combination of

corrosion-induced crack length and high stresses can occur in vivo and lead to catastrophic failure.

Tensile bending stresses in the neck are highest at the neck-stem junction and increase with increasing neck length (Figure A.5). The modular neck can be considered a cantilevered beam held in place by the stem, with a force applied at the femoral head. With no change in cross-sectional geometry, the bending stresses increase linearly with distance from the applied force according to the following equation:

$$\sigma = \frac{(F L \sin \theta)}{\pi d^3 / 32} \quad (\text{A.1})$$

where σ is the bending stress in the neck, $F \sin \theta$ is the perpendicular component of the applied force, L is the distance to the applied force (approximately the neck length), and d is the diameter of the neck's roughly circular cross-section. In other words, a long neck will bend more and exhibit higher stresses than a short neck. According to the manufacturer's information on this particular device, the long neck length option is about 25% longer than the standard neck length, producing roughly 25% higher bending stresses (Wright Medical Technology). This equation does not take into effect the changing cross-sectional geometry of the neck. However, this analysis suggests that higher stresses will contribute to a greater risk of fracture in long necks. In this case a long neck was used in a relatively tall, heavy patient, which contributed to stresses high enough at the neck-stem junction to propagate the corrosion-induced crack.

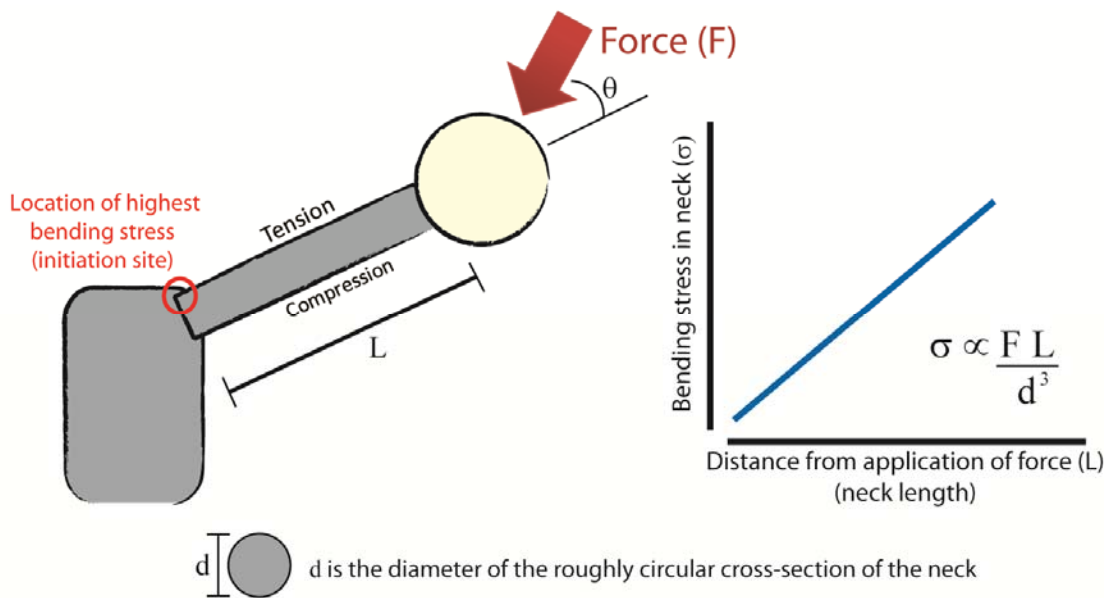


Figure A.5. Schematic illustration (not to scale) showing that bending stresses at the neck-stem junction increase linearly with neck length. Long neck lengths result in increased stresses that may contribute to corrosion-induced fracture at the neck-stem junction.

Fretting and crevice corrosion without catastrophic fracture have been previously reported in other double-modular hip devices (Kop & Swarts, 2009; Viceconti et al., 1997) and are well-documented in single Morse tapers at the head-neck junction (Brown et al., 1995; Collier et al., 1992; Schaaff, 2004). Corrosion of the Morse taper can involve a galvanic cell produced by two dissimilar metal alloys such as cobalt chromium and titanium. However, a large retrieval study of Morse tapers by Brown et al. found that fretting and crevice corrosion occurred equally in cases of identical metals (Kop & Swarts, 2009). This retrieval supports the conclusion that the corrosion process in orthopaedic devices does not require two dissimilar metals, and that the corrosion conditions leading to fracture can be present in double modular designs.

This case of neck fracture in this particular double-modular design is not an isolated incident. A review of the FDA's adverse event report database reveals at least eight other reported instances of fractured necks in this device design since July 2006 (FDA, 2009). The time in vivo of these reported failures ranges from 15 months to 42 months, with no specific indication of traumatic events such as falls. When activity was reported at the time of the event, one patient was reportedly running on the treadmill, one getting up from the sofa, and one walking. Two instances relate the location of the fracture as the "base of the neck" and "flush with the stem" similar to this case. The other instances do not specify the location on the neck. No images were included and the explants were reportedly returned to the manufacturer.

The events described above suggest that this fracture is not a single occurrence, but is instead a representative case of the trade-off in modular design used in orthopaedic implants. While modularity enables the surgeon to better-optimize the patient's biomechanics and anatomy, additional mechanical junctions can lead to corrosion processes resulting in fracture. Based on these findings, it appears that there is a risk of implant fracture at the stem-neck junction when using double modular devices with long neck lengths in heavy patients. Given the occurrence of fretting due to modularity, the high stresses at the neck-stem junction, and the cyclic nature of loading on hip prostheses, the modular neck component is likely at risk for fracture without the occurrence of a traumatic event.

Appendix B

Evolution of Lamellar Alignment in Plastically-Strained Ultra-High

B.1 Introduction

As discussed in this dissertation, cross-linked ultra-high was introduced in joint replacements due to its observed decrease in wear. Concomitantly, cross-linking introduces free radicals that cause oxidative degradation of the material, and so must be followed by re-melting to neutralize free radicals. However, cross-linking and re-melting decreases the fatigue crack propagation resistance and lowers ultimate properties relative to conventional ultra-high. This trade-off may be better-understood by evaluating the plasticity-induced lamellar alignment occurring at the microstructural level during wear and crack propagation.

It has been proposed that plasticity-induced alignment of the crystalline lamellae parallel to the sliding direction is a precursor to wear (Edidin et al., 1999; Wang, Stark, & Dumbleton, 1996). Therefore, the decrease in wear observed in cross-linked ultra-high is thought to result from the cross-linked network restricting lamellar alignment (McKellop et al., 1999; Muratoglu et al., 1999). Furthermore, lamellar orientation and size have been shown to affect crack propagation resistance in this dissertation and elsewhere (L. Pruitt & Bailey, 1998). However, limited work has been done to understand the micromechanisms responsible for lamellar alignment.

This study seeks to elucidate plasticity-induced lamellar alignment in conventional ultra-high. A better understanding of this process will serve to establish the relationship between lamellar alignment and mechanical behavior in total joint replacements.

B.2 Methods and Materials

Uniaxial tensile tests were performed on an Instron 8871 servohydraulic load frame using machined dog-bone specimens (ASTM Type IV) of medical-grade conventional untreated GUR 1020. The specimens were strained at 0%, 25%, 100%, 240%, and 400% engineering strain at a rate of 5 mm/min while subject to room temperature compressed air jet cooling. Samples were then taken from the middle of the gage section and subjected to several characterization techniques (Figure B.1). A potassium permanganate etching procedure which preferentially removes the amorphous phase was followed by field emission scanning electron microscopy (SEM) to qualitatively evaluate the initial and altered crystalline lamellae in terms of orientation and size. Crystallinity and melting temperature were assessed using differential scanning calorimetry (DSC) on samples of approximately 10 mg. The chemical composition of the samples was analyzed using attenuated total reflectance Fourier transform infrared spectroscopy (ATR-FTIR). Details on the methods and equipment are found in Chapter 2.

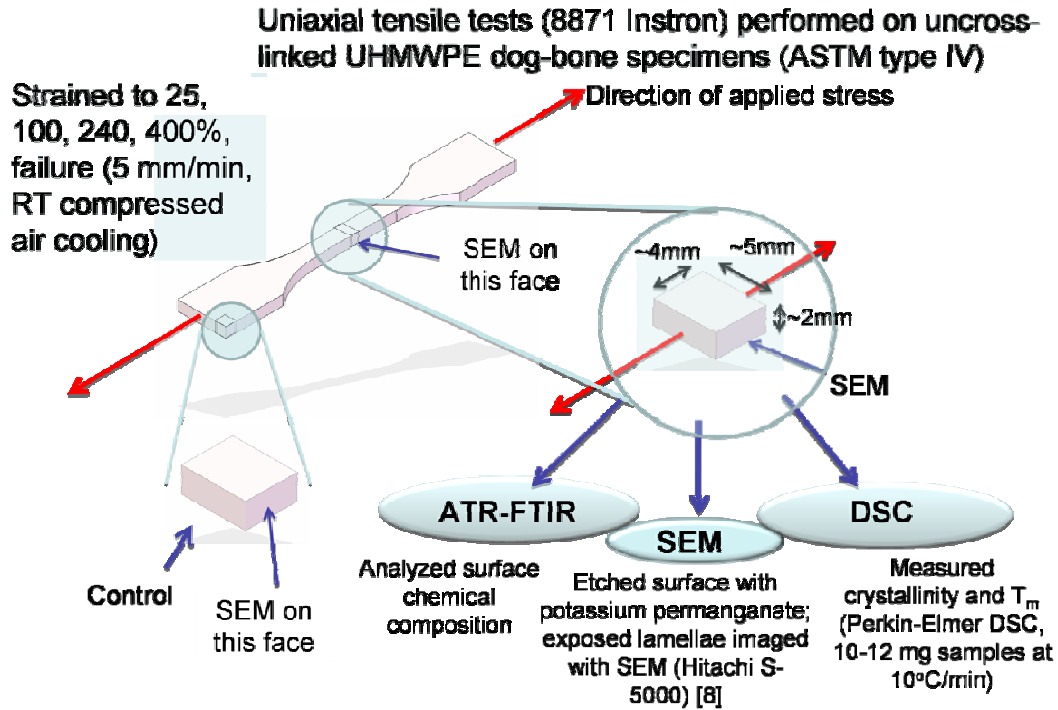


Figure B.1. Schematic of testing and characterization procedure. Modified from original image by Alastair Kilgour.

B.3 Results

Scanning electron microscope images show that lamellar alignment in the direction of applied stress became apparent at 240% engineering strain and higher. Alignment was accompanied by lamellar stack rotation, lamellar bending, localized lamellae break-up, and a shallower penetration of the etchant (Figure B.2). No statistically significant changes in crystallinity, melting temperature, or chemical composition were observed, although there was a trend for the crystallinity and melting temperature to decrease as the strain increased to failure (Table B.1).

DSC Thermal Analysis Results						
Engineering strain (%)	0%	25%	100%	240%	400%	Fail
Crystallinity (%)	47.0	46.9	45.9	45.2	42.3	40.7
Mean \pm S.D. (n=3)	± 1.2	± 0.7	± 1.2	± 1.3	± 0.3	± 1.7
Melting Temp (°C)	139.3	139.2	139.5	137.4	137.5	137.7
Mean \pm S.D. (n=3)	± 0.9	± 1.4	± 1.0	± 1.8	± 0.3	± 1.5

Table B.1. Results from thermal analysis of the strained ultra-high showing decreasing crystallinity and melting temperature with increasing strain.

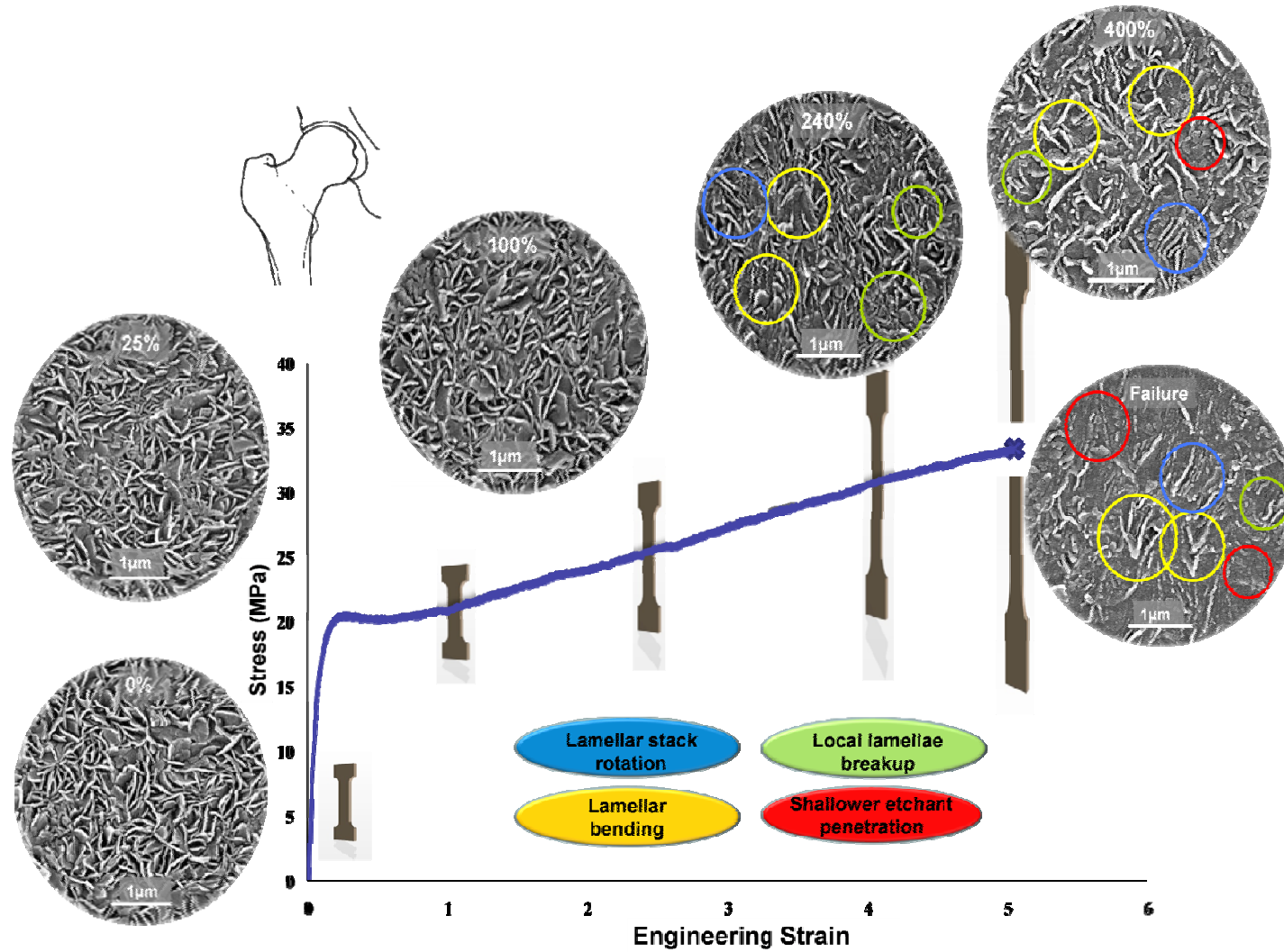


Figure B.2. Scanning electron microscope images of the lamellae demonstrating features of plastic deformation at high levels of engineering strain including: lamellar stack rotation, lamellar bending, local lamellae breakup (fragmentation), and shallower etchant penetration.

B.4 Discussion

In this uncross-linked conventional ultra-high, the onset of large-scale lamellar orientation is evident at 240% engineering strain (approximately half of failure strain). The observed localized breakup of lamellae and the appearance of bent (v-shaped) lamellae at 240% strain is evidence of physical breakdown (fragmentation) of individual lamellae upon aligning in a more closely-packed environment.

The shallower penetration of etchant above 240% strain suggests a loss of free volume as the stretched amorphous chains draw together and form a weak pseudo-crystalline phase between the lamellae (Bartczak & Kozanecki, 2005). Evidence of lamellar stack rotation accompanied by smaller lamellae at these strains indicate interlamellar shear and possible chain pull-out (Lin & Argon, 1994). The homogeneous nature at ultimate strain indicates the evolution of a quasi-single crystalline nature, supported by a decreasing trend in melting temperature and crystallinity due to lamellae fragmentation.

The ability of lamellae to orient in response to applied plastic strains may be an important mechanism for wear and fatigue resistance. For example, it has been widely suggested that wear-resistant cross-linked ultra-high inhibits lamellar alignment by forming a network in the amorphous phase (McKellop et al., 1999; Muratoglu et al., 1999; Zhou & Komvopoulos, 2005). It has also been suggested in this dissertation that resistance to fatigue crack propagation depends on energy dissipation at the crack tip. Such energy in front of the crack tip may be taken up by re-orientating lamellae, bending lamellae, and physically fragmenting lamellae by chain pull-out. Extending this investigation to cross-linked ultra-high would be a next step in understanding microstructural evolution and its influence on plastic deformation, wear, and fatigue resistance in clinically relevant orthopaedic materials.